

2011

## Quantitative Mapping of Cyanobacterial Blooms Using Oceansat-1 OCM Satellite Data

Padmanava Dash

*Louisiana State University and Agricultural and Mechanical College*

Follow this and additional works at: [https://digitalcommons.lsu.edu/gradschool\\_dissertations](https://digitalcommons.lsu.edu/gradschool_dissertations)



Part of the [Oceanography and Atmospheric Sciences and Meteorology Commons](#)

---

### Recommended Citation

Dash, Padmanava, "Quantitative Mapping of Cyanobacterial Blooms Using Oceansat-1 OCM Satellite Data" (2011). *LSU Doctoral Dissertations*. 1487.

[https://digitalcommons.lsu.edu/gradschool\\_dissertations/1487](https://digitalcommons.lsu.edu/gradschool_dissertations/1487)

This Dissertation is brought to you for free and open access by the Graduate School at LSU Digital Commons. It has been accepted for inclusion in LSU Doctoral Dissertations by an authorized graduate school editor of LSU Digital Commons. For more information, please contact [gradetd@lsu.edu](mailto:gradetd@lsu.edu).

**QUANTITATIVE MAPPING OF CYANOBACTERIAL BLOOMS  
USING OCEANSAT-1 OCM SATELLITE DATA**

A Dissertation

Submitted to the Graduate Faculty of the  
Louisiana State University and  
Agricultural and Mechanical College  
in partial fulfillment of the  
requirements for the degree of  
Doctor of Philosophy

in

The Department of Oceanography and Coastal Sciences

by

Padmanava Dash

Bachelor of Science, Utkal University, 1999

Master of Science, Utkal University, 2001

Master of Science, I.I.T. Bombay, 2003

Master of Science, Bowling Green State University, 2005

December 2011

## ACKNOWLEDGMENTS

I would like to express my deepest gratitude to my advisor, Dr. Nan Walker, for giving me the opportunity to pursue my Ph.D. and patiently guiding me through this rigorous academic process. I am thankful to her for providing me financial assistance through a graduate assistantship during this period. Without her continuous support and guidance, this dissertation would not have been possible. I would like to express my sincere appreciation for my committee members, Dr. Eurico D'Sa, Dr. Nancy Rabalais, Dr. Sibel Bargu, Dr. Brian Marx, and Dr. Huiming Bao. Further, I would like to thank Dr. D'Sa for his expert advice on my dissertation research and letting me use his sophisticated laboratory. I would also like to thank Dr. Rabalais, Dr. Bargu, Dr. Walker and Dr. D'Sa again for their insightful comments on my manuscripts.

I would like to thank NASA and the Southern University Center for Coastal Zone Assessment and Remote Sensing Program as well as the Shell Oil Company for funding my research and the Department of Oceanography and Coastal Sciences for the teaching assistantship support. I am thankful to Dr. Chuanmin Hu, University of South Florida, for his help in atmospheric correction; Sherwin Ladner, NRL, NASA Stennis Space Center, for performing the de-striping procedure on the OCM data; Bryan Franz, NASA Goddard Space Flight Center, for incorporating OCM data processing capabilities in SeaDAS; and the OBPG team at NASA Goddard Space Flight Center for providing support and answering questions on SeaDAS. I am thankful to my MS thesis advisor Dr. Robert Vincent, Bowling Green State University, Bowling Green, OH for introducing me to research in remote sensing of cyanobacteria. I extend special thanks to Floyd Demers for field support; Meredith Hunt and Puneeta Naik for helping in laboratory analysis of water samples; Alaric Haag and Chet Pilley for their help with the Terascan<sup>TM</sup> software; and Mary Lee Eggart for aiding with the figures.

Successful completion of this research was only possible due to the companionship, encouragement and support of many colleagues and friends. Firstly, I would like to thank Dr. Deepak Mishra at MSU. This dissertation would have remained a dream for me had it not been for Dr. Mishra's constant encouragement and advice. I cannot find words to express my gratitude to Dr. Hemant Chowdhary who has been a solid pillar of support in all these years. I would like to thank my dear friends Bibhudutta, Shatrughan, Neha, Renee and again, Puneeta for their support and care, which helped me overcome setbacks and stay focused on my graduate study. I greatly value their friendship. I deeply appreciate Shreekanth Balasubramanian's technical assistance and friendship.

The blessings of my family members kept me going and I thank them all for the same. Words cannot express my heartfelt thanks to my sister and brother-in-law for their general interest in my progress throughout the course of my studies at Louisiana State University. I realize that the achievements I have made are based on the opportunities presented to me earlier that my sister and brother-in-law were responsible for. Last but not the least, it was the understanding and support of my wife, Jagnyaseni, and the ever smiling face of my son, Shriyansh, that kept me energetic and enthusiastic.

## TABLE OF CONTENTS

ACKNOWLEDGMENTS.....	ii
LIST OF TABLES.....	vi
LIST OF FIGURES.....	vii
ABSTRACT.....	x
CHAPTER 1. INTRODUCTION.....	1
1.1 Background.....	1
1.2 The Problem.....	2
1.3 Study Area.....	3
1.4 Satellite Data.....	3
1.5 Objectives and Research Questions.....	6
1.6 Dissertation Structure.....	9
CHAPTER 2. LITERATURE REVIEW, FIELD DATA COLLECTION AND LABORATORY ANALYSES.....	11
2.1 Literature Review.....	11
2.1.1 Satellite Data.....	11
2.1.2 Atmospheric Correction of Satellite Data.....	13
2.1.3 Satellite Remote Sensing of Phytoplankton.....	17
2.2 Field Data Collection and Laboratory Analyses.....	18
2.2.1 Analyses of Water Samples.....	19
2.2.1.1 HPLC Analysis of Photopigments.....	19
2.2.1.2 Phycocyanin Analysis.....	21
2.2.1.3 Measurement of CDOM Absorption Coefficients.....	22
2.2.1.4 Analysis of Suspended Sediments.....	23
2.2.1.5 Microscopic and Toxin Analyses.....	23
2.2.1.6 Particulate Absorption Measurements.....	24
2.2.2 <i>In Situ</i> Water Quality Data Using YSI Instruments.....	26
2.2.3 <i>In Situ Rrs</i> Measurements.....	28
CHAPTER 3. ATMOSPHERIC CORRECTION AND VICARIOUS CALIBRATION OF OCEANSAT-1 OCM DATA.....	29
3.1 Introduction.....	29
3.2 Materials and Methods.....	32
3.2.1 Satellite Data Processing Overview.....	32
3.2.2 Atmospheric Correction Procedure.....	35
3.2.2.1 Computation of Rayleigh Path Radiance.....	36
3.2.2.1.1 Computation of Rayleigh Optical Thickness.....	37
3.2.2.1.2 Computation of Rayleigh Scattering Phase Function.....	37
3.2.2.2 Computation of Aerosol Path Radiance.....	39
3.2.2.3 Computation of Diffuse Transmittance.....	41
3.2.2.4 Computation of Water-Leaving Radiance.....	41

3.2.2.5 Computation of Normalized Water-Leaving Radiance.....	41
3.2.2.6 Computation of Remote Sensing Reflectance.....	42
3.2.3 Vicarious Calibration.....	42
3.2.4 Destriping.....	44
3.3 Results and Discussion.....	45
3.4 Conclusions.....	57
CHAPTER 4. ESTIMATION OF CYANOBACTERIAL PIGMENTS IN A FRESHWATER LAKE USING OCM SATELLITE DATA.....	
4.1 Introduction.....	58
4.2 Materials and Methods.....	60
4.2.1 Study Site.....	60
4.2.2 Field Data.....	60
4.2.3 Satellite Data.....	63
4.2.4 Destriping.....	64
4.2.5 Vicarious Calibration.....	64
4.2.6 Atmospheric Correction.....	65
4.2.7 Algorithm Development.....	67
4.2.8 Algorithm Validation.....	70
4.3 Results.....	70
4.3.1 Phytoplankton Pigments.....	70
4.3.2 Satellite Data.....	73
4.3.3 Optimization of Algorithms for PC.....	74
4.3.4 Optimization of Algorithms for Chl <i>a</i> .....	78
4.3.5 Optimization of Algorithms for Accessory Pigments.....	81
4.3.6 Application of Algorithms to OCM Image Data.....	82
4.4 Discussion.....	84
4.4.1 Usefulness of Algorithms Developed From Satellite Data.....	84
4.4.2 Advantages of Using OCM Data.....	85
4.4.3 Assessment of the Developed Algorithms.....	86
4.5 Conclusions.....	90
CHAPTER 5. SUMMARY AND FUTURE DIRECTIONS.....	
5.1 Summary.....	92
5.2 Future Directions.....	96
REFERENCES.....	98
APPENDIX	
A. TIME SERIES OF WATER QUALITY PARAMETERS MEASURED BY THE DEPLOYED YSI INSTRUMENTS.....	106
B. GLOSSARY.....	109
C. PERMISSION.....	110
VITA.....	116

## LIST OF TABLES

Table 2.1 Specifications of satellite sensors, OCM and SeaWiFS.....	13
Table 2.2 Summary of field data collection in 2006-2007. Clear-sky OCM data were obtained on the dates shown with ‘*’.....	20
Table 2.3 Summary of field data collection in 2009. Clear-sky OCM data were obtained on the dates shown with ‘*’.....	20
Table 3.1 Comparison of OCM and SeaWiFS attributes and geometries at the six atmospheric correction sites on the six dates.....	33
Table 3.2 Vicarious calibration coefficients of OCM bands 1-6.....	44
Table 4.1 Regression results of PC algorithms. P-values were less than 0.0001 for all the PC algorithms. Relative RMSE and relative MAE are given in %.....	79
Table 4.2 Regression results of Chl <i>a</i> algorithms. P-values were less than 0.0001 for all the Chl <i>a</i> algorithms developed and validated. Relative RMSE and relative MAE are given in %.....	79
Table 4.3 Measured and image-derived concentrations of PC and Chl <i>a</i> on April 20, 2007 (with higher concentration of PC and Chl <i>a</i> ) and June 21, 2007 (with lower concentration of PC and Chl <i>a</i> ). The image-derived PC and Chl <i>a</i> were obtained by application of PC algorithm 2 and Chl <i>a</i> algorithm 2. Note that high concentrations of PC and Chl <i>a</i> were obtained at regions of the lake that were not covered by field sampling.....	84

## LIST OF FIGURES

Fig. 1.1. OCM true-color image of April 12, 2007 showing (A) location of Lac des Allemands in southeastern Louisiana, (B) Lac des Allemands with respect to various lakes, bayous and canals, and (C) twelve sampling sites (S1-S12).....	4
Fig. 1.2. OCM true-color images of (A) November 17, 2006, (B) April 12, 2007, (C) April 26, 2007, and (D) May 18, 2007 showing Lac des Allemands, Lake Salvador and Lake Catouatche.....	5
Fig. 1.3. PC absorbance taken from MacColl and Guard-Friar (1987) and PC absorption coefficient measured in this study showing the characteristic PC absorption maximum with a prominent shoulder towards lower wavelengths. Locations of OCM bands 5 and 4 centered at 556.4 and 510.6 are indicated by the vertical lines.....	7
Fig. 2.1 YSI measured time series of Chl <i>a</i> concentrations and water temperature at the YSI instrument deployment site in Lac des Allemands from October 24, 2006 through December 11, 2007. HPLC Chl <i>a</i> at the water surface from November 17, 2006 through November 8, 2007 and at the sensor depth from December 17, 2006 through November 8, 2007 are shown with the YSI Chl <i>a</i> with sampling days indicated ( <i>see</i> Table 2.2 for the list of sampling days).....	27
Fig. 3.1. SeaDAS processed SeaWiFS Chl <i>a</i> images of northern Gulf of Mexico. The sites represented by squared dots are the clear water locations, where atmospheric correction was performed. The sites represented by triangles are the location from which aerosol characteristics were transferred to the atmospheric correction sites.....	35
Fig. 3.2. Comparison of Rayleigh path radiance for OCM bands 1-6 calculated by the new code and SeaDAS along a scan line of OCM data of June 21, 2007.....	47
Fig. 3.3. Comparison of Rayleigh path radiance for SeaWiFS bands 1-6 calculated by the new code and SeaDAS along a scan line of SeaWiFS data of June 21, 2007.....	48
Fig. 3.4. Comparison of Rayleigh path radiance ( $L_r$ ), aerosol path radiance ( $L_a$ ) and Diffuse transmittance ( $t$ ) calculated by the new code and SeaDAS at the atmospheric correction sites in each of the OCM data.....	48
Fig. 3.5. Comparison of OCM TOA radiances before and after vicarious calibration, and the corresponding $nL_w$ values computed by the new code and SeaDAS. Solid dots with solid lines represent vicariously calibrated $nL_w$ and TOA radiances, and hollow dots with dotted lines represent $nL_w$ and TOA radiances before vicarious calibration.....	51
Fig. 3.6. Comparison of new code and SeaDAS computed OCM and SeaWiFS $nL_w$ .....	52



Fig. 3.7. Comparison of TOA radiance before vicarious calibration ( $L_t$ ) and after vicarious calibration (Calibrated $L_t$ ) at four selected sites (S1, S7, S9 and S12) from the 12 sites in Lac des Allemands for the OCM data of April 20, 2007. Comparison of Rayleigh path radiance ( $L_r$ ) calculated by the new code and SeaDAS at these 4 sites is also shown.....	53
Fig. 3.8. Comparison of aerosol radiance ( $L_a$ ) calculated by the new code and SeaDAS at the 12 sites in Lac des Allemands for the OCM data of April 20, 2007.....	54
Fig. 3.9. Comparison of <i>in situ</i> $R_{rs}$ and $R_{rs}$ estimated by the new code before and after destriping. <i>In situ</i> $R_{rs}$ was obtained with a hand-held hyperspectral radiometer and then weighted with the relative spectral response function of each OCM band.....	55
Fig. 3.10. Comparison of normalized water-leaving radiance ( $_nL_w$ ) calculated by SeaDAS and by the new code before and after destriping of the OCM data of April 20, 2007 at selected 5 sites (S1, S3, S7, S9 and S12) out of the 12 sites in Lac des Allemands.....	56
Fig. 4.1. (A) Chl $a$ , (B) PC, (C) echinenone and (D) zeaxanthin concentrations at the twelve sampling sites (S1-S12) from November 17, 2006 through November 8, 2007 with sampling days indicated ( <i>see</i> Table 2.2 for the list of sampling days).....	72
Fig. 4.2. (A) Chl $a$ , (B) PC, (C) echinenone and (D) zeaxanthin concentrations at the twelve sampling sites (S1-S12) from May 1, 2009 through June 30, 2009 with sampling days indicated ( <i>see</i> Table 2.3 for the list of sampling days).....	72
Fig. 4.3. ChemTax-derived concentrations of algal groups during 2006-2007 (top panel) and 2009 (bottom panel).....	73
Fig. 4.4. (A) Comparison of OCM $R_{rs}$ spectra when low, moderate and high PC concentrations were measured. (B) Relationship between field measured PC and Chl $a$ .....	75
Fig. 4.5. (A) PC algorithm developed using OCM $R_{rs}$ with subtraction of $R_{rs}$ accounting for absorption by water+Chl $a$ +NAP+CDOM and backscattering by water using 2006-2007 database (B) PC estimated from OCM data using this algorithm versus measured PC of 2009.....	78
Fig. 4.6. (A) Chl $a$ algorithm developed using OCM $R_{rs}$ with subtraction of $R_{rs}$ accounting for absorption by water+PC+ NAP+CDOM and backscattering by water using 2006-2007 database (B) Chl $a$ estimated from OCM data using this algorithm versus measured Chl $a$ of 2009.....	81
Fig. 4.7. PC, Chl $a$ and true color images derived from OCM data of April 20, 2007 and June 21, 2007. The PC and Chl $a$ images were obtained by application of PC algorithm 2 and Chl $a$ algorithm 2. The 12 sampling sites are indicated in the true color images.....	83
Fig. A.1 Time series of salinity at the YSI instrument deployment site in Lac des Allemands from October 24, 2006 through December 11, 2007.....	106

Fig. A.2 Time series of dissolved oxygen at the YSI instrument deployment site in Lac des Allemands from October 24, 2006 through December 11, 2007.....	106
Fig. A.3 Time series of optical backscatter, a measure of turbidity, at the YSI instrument deployment site in Lac des Allemands from October 24, 2006 through December 11, 2007....	107
Fig. A.4 Time series of PC concentrations at the YSI instrument deployment site in Lac des Allemands from October 24, 2006 through December 11, 2007.....	107
Fig. A.5 Water level at the YSI instrument deployment sites in Lac des Allemands and Lake Salvador, and the water level anomalies in comparison with mean daily discharge at the Davis Pond Diversion.....	108

## ABSTRACT

Cyanobacteria represent a major harmful algal group in fresh to brackish water environments. Lac des Allemands, a freshwater lake of 49 km<sup>2</sup> southwest of New Orleans, Louisiana, provides a natural laboratory for remote characterization of cyanobacteria blooms because of their seasonal occurrence. This dissertation makes a contribution to research methodology pertaining to atmospheric correction of satellite data and development of remote sensing algorithms to quantify cyanobacterial pigments.

The Ocean Color Monitor (OCM) sensor provides radiance measurements similar to Sea-viewing Wide Field-of-View Sensor (SeaWiFS) but with higher spatial resolution. However, OCM does not have a standard atmospheric correction procedure and the comprehensive suite of atmospheric correction procedures for ocean (or lake) is not available in the literature in one place. Atmospheric correction of satellite data over inland lakes, estuaries and coastal waters is also challenging due to difficulties in the estimation of aerosol scattering accurately over these optically complex water bodies. Thus an atmospheric correction procedure was developed to obtain more accurate spectral remote sensing reflectance ( $R_{rs}$ ) over Lac des Allemands from OCM data based on NASA's extensive work for SeaWiFS. Since OCM was not well calibrated, a new vicarious calibration procedure was also developed to adjust OCM radiance values to SeaWiFS radiance as SeaWiFS is well calibrated over its entire life.

Empirical inversion algorithms were developed to convert the OCM  $R_{rs}$  at bands centered at 510.6 and 556.4 nm to concentrations of phycocyanin (PC), the primary cyanobacterial pigment. For the algorithms to be uniformly valid over all areas (or all bio-optical regimes) of the lake, a holistic approach was developed to minimize the influence of other optically active constituents on the PC algorithms. Similarly, empirical algorithms to estimate chlorophyll *a* (Chl *a*) concentrations were developed using OCM bands centered at 556.4 and

669 nm. The best PC algorithm ( $R^2=0.7450$ ,  $p<0.0001$ ,  $n=72$ ) yielded a root mean square error (RMSE) of 36.92  $\mu\text{g/L}$  with a relative RMSE of 10.27%, and a mean absolute error (MAE) of 21.79  $\mu\text{g/L}$  with a relative MAE of 6.06% (PC from 2.75 to 363.50  $\mu\text{g/L}$ ,  $n=48$ ). The best algorithm for Chl *a* ( $R^2=0.7510$ ,  $p<0.0001$ ) produced an RMSE of 31.19  $\mu\text{g/L}$ , with relative RMSE = 15.70% and a MAE of 16.56  $\mu\text{g/L}$ , with relative MAE = 8.33% (Chl *a* from 9.46 to 212.76  $\mu\text{g/L}$ ,  $n=48$ ). The results demonstrate the preliminary success of using the  $360 \times 236$  m resolution OCM data to map cyanobacterial blooms in a small lake. While more field data are required to further validate the long-term performance of the algorithms, at present the algorithms may be implemented to process OCM data in an automated setup to provide timely information on the lake's bloom conditions. Similarly, retrospective processing may provide a long-term time series of bloom characteristics to document potential trends. The applicability of the algorithms can be extended to other lakes after necessary testing.

# **CHAPTER 1**

## **INTRODUCTION**

### **1.1 Background**

Cyanobacteria, also known as blue-green algae, are important primary producers in many areas of the ocean, but most dominant in inland waters (Dyer, 2003). They produced most of the oxygen in the earth's atmosphere 2.8 billion years ago, which dramatically changed the life forms on earth and provoked an explosion in biodiversity (Olson, 2006). Cyanobacteria blooms are undesirable since they discolor the water, cause turbidity in recreational and amenity facilities and synthesize a large number of low molecular weight compounds which cause taste and odor problems (Metcalf and Codd, 2004). Of particular concern are a diverse range of toxins termed as cyanotoxins produced by cyanobacteria which are hazardous to human, animal and aquatic ecosystem health (Codd, 1999; Carmichael, 1997; Falconer, 2005). Due to the human health threats and their negative impact on aquaculture, recreation, and tourism, cyanobacterial blooms have significant economic and socio-cultural impacts (Anderson, 2007).

Cyanobacterial blooms have become more prevalent in recent decades and increasing globally and in the U.S. (Anderson, 2007). As a result there is an emerging consensus for the development of methods for operational monitoring of the blooms in coastal and inland waters world-wide (Kutser, 2009). Conventional monitoring strategies based on sampling at fixed stations, cannot provide the information needed. Therefore, alternative methods such as satellite remote sensing may be preferred because they are economical and provide synoptic views with fairly rapid repeat coverage that is unmatched by data collection at fixed stations. However, it is not a simple task because inland waters where cyanobacteria blooms occur are often optically complex and this complexity varies over space and time. To extract meaningful information from remotely sensed data, specialized techniques must be developed.

## 1.2 The Problem

Accurate characterization of the spatial distribution and concentration of cyanobacteria using remote sensing can be challenging due to several reasons.

- (i) Range of concentration: Validity of an algorithm for estimating cyanobacteria over a broad range of concentration requires the algorithm to be developed using a wide range of concentration from field measurements.
- (ii) Temporal, spatial, spectral, and radiometric resolution of satellite data: The most critical parameters for choosing satellite sensors for operational monitoring of phytoplankton blooms in coastal and inland waters are the sensors' revisit time and the spatial resolution. Other important considerations are radiometric sensitivity, placement of bands, and spectral resolution. Hence, choice of an optimal sensor based on these criteria is crucial.
- (iii) Atmospheric correction of satellite data: In aquatic remote sensing, the water-leaving radiance forms a small fraction of the total radiance received by the sensor, with the main contribution being due to the atmosphere. Hence, an accurate atmospheric correction procedure is crucial for utilizing the full potential of satellite data. The inland water bodies are often shallow and turbid. Therefore, the atmospheric correction procedure should have the capability to process turbid water pixels accurately.
- (iv) Bio-optical algorithms: Differential absorption and scattering of light by several optically active substances coastal in inland waters pose a challenge for an algorithm to be uniformly valid over all areas (or all bio-optical regimes) of the lake. Therefore, the optical complexity needs to be resolved and the influence of additional optically active substances should be algebraically decomposed from the total absorption and scattering spectrum.

The issues related to range of concentration and resolution of satellite data can be resolved by choosing an appropriate study area and adapting to a satellite sensor with sufficient temporal, spatial, spectral, and radiometric resolution suitable for operational monitoring of cyanobacterial blooms. Subsequently, the satellite data should be perfected using an atmospheric correction procedure suited to the study area and the satellite data. Finally, using field data from the study area and atmospherically corrected satellite data, bio-optical algorithms can be developed. The developed algorithms should be validated on a new dataset to test the performance of the algorithms.

### **1.3 Study Area**

A study area was sought that could meet the criteria of a wide range of cyanobacterial concentrations. The study area selected was Lac des Allemands because this lake provides an ideal natural laboratory for this study as high concentrations of cyanobacteria usually occur in spring and summer (Fig. 1.1) (Ren et al., 2009; Garcia et al., 2010; Swenson et al., unpublished data; Rabalais, unpublished data). Lac des Allemands (French for "Lake of the Germans") is a 49 km<sup>2</sup> (12,000 acre) lake located in the uppermost part of the Barataria estuary in southeastern Louisiana mostly in St. John the Baptist Parish and partly in Lafourche and St. Charles Parishes centered at 29°55'25.74'' N and 90°34'39.31'' W. It is 42 km (26 mi) southwest of New Orleans. The average depth of Lac des Allemands is 2 meters, reaching a maximum depth of 3.3 meters (10 feet).

### **1.4 Satellite Data**

The Oceansat-1 satellite launched on May 26, 1999 carries the OCM sensor with spectral bands nearly identical to the Sea-viewing Wide Field-of-View Sensor (SeaWiFS) sensor. SeaWiFS and MODIS (Moderate Resolution Imaging Spectroradiometer) 1 km ocean bands



Fig. 1.1. OCM true-color image of April 12, 2007 showing (A) location of Lac des Allemands in southeastern Louisiana, (B) Lac des Allemands with respect to various lakes, bayous and canals, and (C) twelve sampling sites (S1-S12).

have high radiometric sensitivity (O'Reilly et al., 1998); however, they lack the spatial resolution needed for studying smaller water bodies. Most of the other ocean color sensors (such



as MERIS, MISR, OCI, OSMI, GLI and POLDER-2) have the required spatial resolution for studying smaller water bodies, but they lack frequent revisit cycles. The Oceansat-1 OCM sensor provides a compromise between the two types of sensors discussed above with a spatial resolution of  $360 \times 236$  m and an orbit that repeats exactly every alternate day. OCM true-color images of November 17, 2006, April 12, 2007, April 26, 2007, and May 18, 2007 covering the study area are shown in Fig. 1.2. In this sequence of true color images the “greenness” of Lac des Allemands water was observed to intensify with increasing concentration of phytoplankton. The maximum greenness in Lac des Allemands was on April 26, 2007. The very different water color within Lake Catouatche and Lake Salvador is due to high concentrations of river sediments.

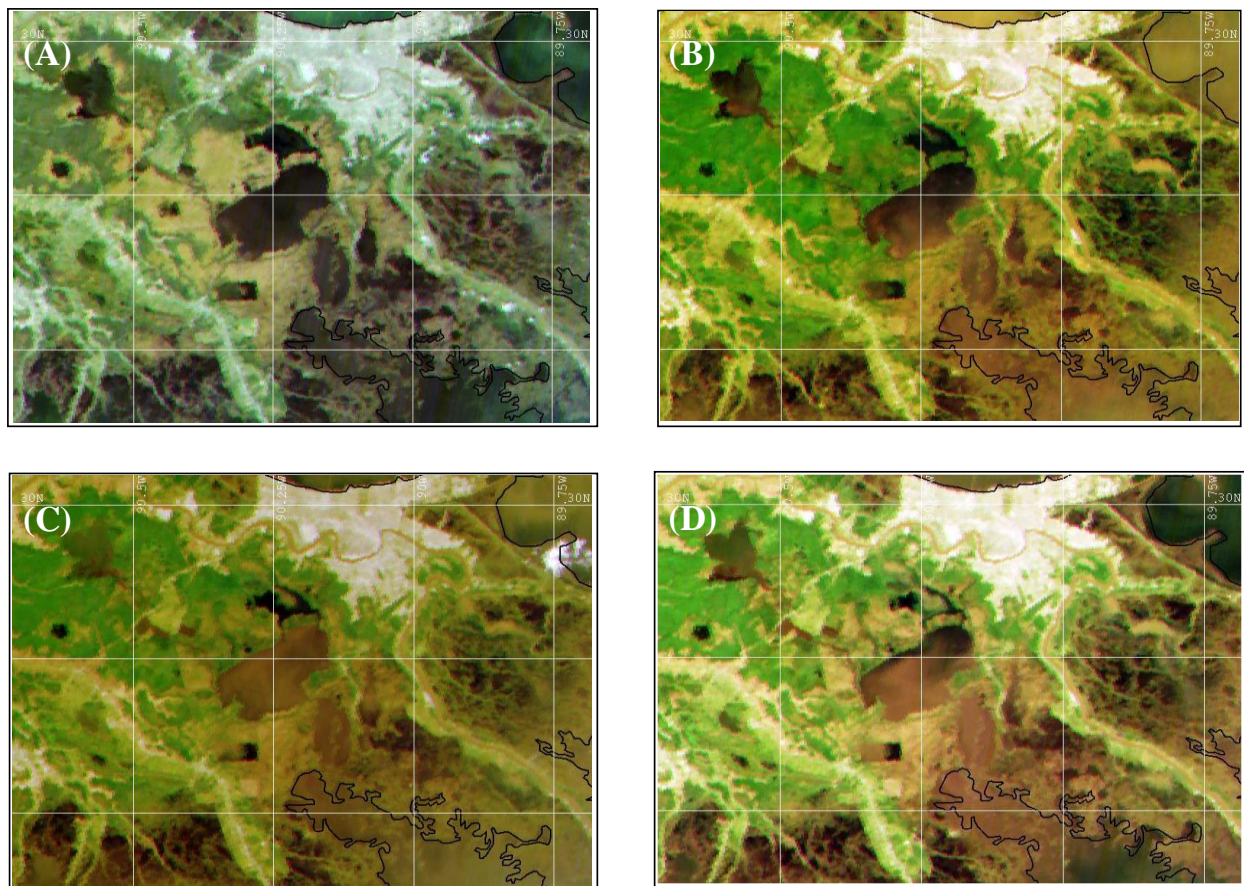


Fig. 1.2. OCM true-color images of (A) November 17, 2006, (B) April 12, 2007, (C) April 26, 2007, and (D) May 18, 2007 showing Lac des Allemands, Lake Salvador and Lake Catouatche.

OCM acquired data for a period of eleven years since 1999, but these data have not been used extensively by the scientific community for studying coastal and inland waters despite its higher spatial resolution. This is possibly due to one or more of the following: a lack of reliable atmospheric correction procedure and bio-optical algorithms for the sensor over coastal and inland waters, the timing of its launch immediately following the launch of the long-awaited SeaWiFS instrument, and difficulty in data access by the scientific community (Crowley, 2003). Nevertheless, the high resolution OCM data has a strong potential for ocean color research especially in coastal and inland waters. In addition, its successor, the OCM-2 sensor, was launched on September 23, 2009 and OCM-3 is planned for launch in 2013 (ISRO, 2010). Due to small size and optical complexities of Lac des Allemands, OCM sensor with its higher spatial resolution and SeaWiFS equivalent spectral bands is an appropriate sensor for this study.

## **1.5 Objectives and Research Questions**

OCM does not have a standard processing software for atmospheric correction. Hence, there was a need for the development of an atmospheric correction procedure with the capability to process optically complex waters, such as Lac des Allemands, to utilize the full potential of OCM data in a quantitative manner. As chlorophyll *a* (Chl *a*) is common to all taxonomic groups its use in mapping phytoplankton distributions does not permit taxonomic differentiation (Hunter et al., 2008). In addition to Chl *a*, phytoplankton contain a range of accessory pigments as part of their photosynthetic systems as light harvesting and photoprotective substances (Schalles and Yacobi, 2000). Phycocyanin (PC), the blue phycobilliprotein, is uniquely associated with cyanobacteria and it has been used to estimate fresh-water cyanobacterial abundance from remotely sensed data. A number of studies (Dekker et al., 1993; Schalles and Yacobi, 2000; Simis et al., 2005; Hunter et al., 2008; Mishra et al., 2009) have utilized the PC absorption

feature near 620 nm to develop algorithms for quantifying cyanobacteria. More recently Hu et al. (2010) and Wynne et al. (2010) focused on the red and near infrared wavelengths to characterize the distribution and intensity of cyanobacteria blooms using remotely sensed data. However, relatively little attention has been devoted to the reflectance and absorption features in the 500-600 nm region. A spectral curve representing PC absorbance shows that PC has an absorption maximum at 620 nm with a prominent shoulder extending to lower wavelengths (MacColl and Guard-Friar, 1987; Fig. 1.3). The same peak and a prominent shoulder toward blue wavelengths were observed from the measurements of PC absorption coefficients of PC standards in this study (Fig. 1.3).

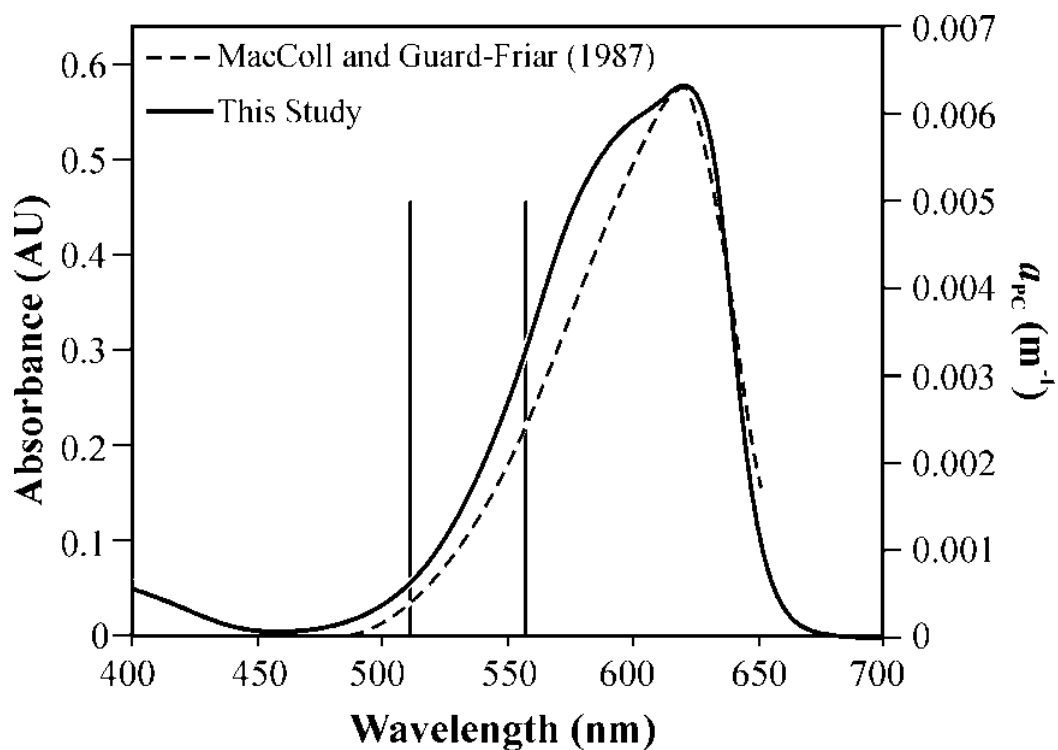


Fig. 1.3. PC absorbance taken from MacColl and Guard-Friar (1987) and PC absorption coefficient measured in this study showing the characteristic PC absorption maximum with a prominent shoulder towards lower wavelengths. Locations of OCM bands 5 and 4 centered at 556.4 and 510.6 are indicated by the vertical lines.

A few studies concerning the mapping of cyanobacteria using satellite measurements have used sensors such as LANDSAT, MERIS, and MODIS (Vincent et al., 2004; Simis et al.,

2005; Wynne et al., 2010; Hu et al., 2010). Additionally, while both SeaWiFS and OCM have been used for detecting the cyanobacteria *Trichodesmium* spp. (Subramaniam et al., 2001; Sarangi et al., 2005), and SeaWiFS has been used together with CZCS and MODIS for quantifying the cyanobacteria *Nodularia spumigena* (Kahru et al., 2007), neither OCM nor SeaWiFS has been used for mapping PC concentrations, mainly because these sensors do not have the spectral band covering the PC absorption maximum. This study aimed at developing OCM-based algorithms for quantifying PC using remote sensing reflectance ( $R_{rs}$ ) at bands <600 nm by modeling and removing the contributions of other optically active constituents in this wavelength region. This study is significant because it presents a technique for atmospheric correction of OCM data and it represents the first attempt of utilizing OCM data to quantify PC. It is also significant because it represents the first effort of using satellite data for both development and validation of algorithms for quantitatively mapping cyanobacteria with  $R_{rs}$  <600 nm.

The primary research objectives were:

- 1) Development of an atmospheric correction procedure for OCM data to obtain accurate spectral  $R_{rs}$  over Lac des Allemands.
- 2) Development of algorithms for quantifying the pigments PC and Chl *a*, using OCM data by modeling and subtracting the influence of additional optically active constituents.
- 3) Validation of algorithms using additional field data.
- 4) Application of the algorithms to OCM image data to map cyanobacterial concentrations over the entire lake.

The four primary research questions addressed in this dissertation are:

- 1) Can spectral  $R_{rs}$  be retrieved accurately by applying a customized atmospheric correction and vicarious calibration procedure to OCM data?
- 2) Can concentrations and spatial distributions of cyanobacteria be quantified using derived reflectance measurements?
- 3) Are wavelengths less than 620 nm applicable for quantifying PC?
- 4) Does subtraction of the effects of other optically active constituents improve the performance of the algorithms for mapping cyanobacterial pigments?

## **1.6 Dissertation Structure**

This dissertation consists of five chapters. Chapter 1 provides an introduction to the nature of the problem and states the research objectives. Chapter 2 presents a review of the literature and an overview of the field data collection and the laboratory analyses performed. Chapter 3 focuses on the development of an atmospheric correction procedure for OCM and solution to problems encountered with the OCM data, including striping and calibration. Chapter 4 constitutes the development and validation of algorithms for quantification of cyanobacteria and phytoplankton assemblages based on the pigments PC and Chl *a*. Chapter 5 summarizes the research contributions and presents an insight into future directions for research.

Parts of the research work presented in this dissertation have been submitted for publication. A manuscript dealing with the atmospheric correction and vicarious calibration of OCM data, presented in chapter 3, is in review with the journal IEEE Transactions on Geoscience and Remote Sensing. A manuscript detailing the algorithm development presented in chapter 4 is published in the journal, Remote Sensing of Environment. Field data collected for this dissertation contributed to a publication in the journal Harmful Algae (Garcia et al., 2010).

Conference abstracts were prepared from the chapters presented above and the results were presented at the ASLO Aquatic Sciences Meeting in February 2011 in San Juan, Puerto Rico; the annual Northern Gulf Institute Conference, May 16-17, 2008 in Biloxi, MS; the Graduate Student Symposium, February 22-24, 2008 at LUMCON in Cocodrie, LA, and the Fourth Symposium on Harmful Algae in the U.S., October 29- November 1, 2007 in Woods Hole, Massachusetts.

## **CHAPTER 2**

### **LITERATURE REVIEW, FIELD DATA COLLECTION AND LABORATORY ANALYSES**

#### **2.1. Literature Review**

##### **2.1.1 Satellite Data**

Satellite ocean color research began in the late 1970s with the Coastal Zone Color Scanner (CZCS) onboard the Nimbus 7 satellite which acquired data from October 1978 to June 1986 (Evans and Gordon, 1994; Acker, 1994; O'Reilly et al., 1998). This instrument provided global and regional data sets which yielded a wealth of information about the distribution and seasonal variability of primary productivity in the ocean. During the period 1986 to 1996, there was a lack of an operational ocean color satellite, until India launched the German sensor MOS (Modular Optoelectronic Scanner) in March 1996. Subsequently, Japan launched the Japanese sensor OCTS (Ocean Color and Temperature Scanner) and the French sensor POLDER (Polarization and Directionality of the Earth's Reflectance) in August 1996. Although these sensors do not provide global coverage, they were important as the first source of new ocean color data after a gap of ten years. The Sea-viewing Wide Field-of-View Sensor (SeaWiFS) onboard the OrbView-2 satellite launched in August 1997 and the two Moderate Resolution Imaging Spectroradiometers (MODIS), including Terra-1 MODIS (since 1999) and Aqua-1 MODIS (since 2002) onboard the Terra and Aqua satellites respectively, provide unprecedented multispectral imagery of the Earth's ocean surfaces every day. The Oceansat-1 (IRS P-4) satellite launched on May 26, 1999 by the Indian Space Research Organization (ISRO) carried the OCM sensor with spectral bands nearly identical to the SeaWiFS and MODIS ocean color bands. Over and above these sensors, a number of other sensors have been launched (MERIS, MISR, OCI, OSMI, GLI, POLDER-2, OCM-2) and some others are planned for launch in the near future.

Recent experience has emphasized that a certain controlled redundancy is essential if we are to enjoy an unbroken stream of ocean color data (ESA, 2006).

Ocean color remote sensing refers to the study of spectral variations of water leaving radiance that can be related to the concentration of phytoplankton pigments, colored dissolved organic matter, and suspended particulate matter. Operational monitoring of smaller water bodies using satellite data requires sufficient spatial resolution and higher frequency of satellite data acquisition because of the inherent spatial and temporal variability of the in-water constituents in these regions (Kutser, 2009). The new generation ocean color sensors such as SeaWiFS and MODIS were primarily designed to measure ocean color with a high temporal but with a relatively coarse spatial resolution (Chauhan et al., 2001). Although these two sensors have much higher radiometric sensitivity and additional spectral bands than CZCS to aid in atmospheric correction and bio-optical applications (Hooker et al., 1993; O'Reilly et al., 1998), they lack the resolution needed for studying smaller water bodies. Most of the other ocean color sensors that have the required spatial resolution for studying smaller water bodies do not have frequent revisit cycles. Oceansat-1 OCM sensor provides a compromise between the spatial resolution of SeaWiFS and MODIS, and revisit cycles of other ocean color sensors. It produces radiance measurements similar to SeaWiFS and the ocean color bands of MODIS. The spatial resolution of OCM is  $360 \times 236$  m, which is superior compared to SeaWiFS ( $1100 \times 1100$  m) and MODIS ( $1000 \times 1000$  m) for studying small lakes and it has the revisit cycle of every alternate day. Table 2.1 summarizes the specifications of OCM sensor in comparison with SeaWiFS.



Table 2.1. Specifications of satellite sensors, OCM and SeaWiFS

Parameters	OCM		SeaWiFS	
		<i>Corresponding Annual Mean <math>F_0</math></i>		<i>Corresponding Annual Mean <math>F_0</math></i>
Band 1	404-424 (414.2)	171.38	402-412 (412)	171.18
Band 2	432-452 (441.4)	184.80	433-453 (443)	188.76
Band 3	479-499 (485.7)	196.31	480-500 (490)	193.38
Band 4	502-522 (510.6)	188.39	500-520 (510)	192.56
Band 5	547-567 (556.4)	185.57	545-565 (555)	183.76
Band 6	660-680 (669.0)	153.44	660-680 (670)	151.22
Band 7	748-788 (768.6)	121.67	745-785 (765)	123.91
Band 8	847-887 (865.1)	97.890	845-885 (865)	95.965
Spatial Resolution	0.360 km across & 0.236 km along track		1.1 km	
Temporal Resolution	2 days		1 day	
Radiometric Resolution	12 bit		10 bit	
Sensor type	Push broom linear array CCD		Whiskbroom scan mirrors	
Orbit type	Sun synchronous		Sun synchronous	
Altitude	720 km		705 km	
Inclination	98.62°		98.2°	
Period	98 min		98.88 min	
Equator crossing	Noon $\pm$ 10 min, Descending		Noon +20 min, Descending	
Tilt	Along track, +20,0,-20		Along track, +20,0,-20	
Swath	1420 Km		2801 km (full swath)	
Calibration	Internal Lamp		Sun, Moon	
Data access	<a href="http://www.antrix.gov.in">http://www.antrix.gov.in</a>		<a href="http://oceancolor.gsfc.nasa.gov">http://oceancolor.gsfc.nasa.gov</a>	

Source: Suresh et al., 2006; Pandya et al., 2002; SeaDAS

Bands 1-8 are in units of nm and center wavelengths are in parenthesis.

$F_0$  is in units of  $\text{mW cm}^{-2} \mu\text{m}^{-1}$

### 2.1.2 Atmospheric Correction of Satellite Data

In the case of ocean color remote sensing, the water-leaving radiance forms a small fraction of the total radiance received by the sensor, as the remaining signal is the solar radiation scattered by the atmosphere. Removal of these atmospheric effects is termed “atmospheric correction”. For processing ocean color data, the SeaWiFS Data Analysis System (SeaDAS) is one of the most comprehensive atmospheric correction procedures developed so far by the Ocean Biology Processing Group (OBPG) at NASA Goddard Space Flight Center. Currently, SeaDAS supports operational data processing from the sensors SeaWiFS, MODIS, OCTS, CZCS, and MERIS.

As defined by Morel and Prieur (1977), Case 1 waters are those waters in which phytoplankton and their degraded products control the optical properties of the water whereas Case 2 waters are influenced by other substances that vary independently of phytoplankton, including suspended sediments and dissolved material in addition to phytoplankton and their degraded products. The SeaDAS processed SeaWiFS or MODIS data from Case 1 waters is fairly accurate and widely used by the ocean color community, however, they generally fail to deliver the Case 1 type accuracy in shallow coastal Case 2 waters (Hu et al., 2000; Wang and Franz, 2000; Kutser, 2009). The SeaDAS atmospheric correction procedure assumes the water-leaving radiance to be negligible in the near infrared (NIR) part of the spectrum. Initially, one of the major reasons for the failure of the SeaDAS atmospheric algorithm in Case 2 waters was very high reflectance in the NIR part of the spectrum due to dense algal bloom areas with high chlorophyll *a* (Chl *a*) concentrations which resulted in processing errors. Iterative methods by Arnone et al. (1998), Stumpf et al. (2003) and Siegel et al. (2000) were developed to correct for non-negligible water reflectance in the NIR arising from moderate to high phytoplankton abundances (Chl *a* concentrations greater than  $\sim 2 \text{ mg m}^{-3}$ ). However, when modest quantities of other constituents (e.g., suspended sediments and colored dissolved organic matter, or CDOM etc.) are present, SeaDAS processing produces negative water-leaving radiances or masks the pixels. This limitation together with the coarse 1 km spatial resolution prevents the use of SeaDAS processed SeaWiFS or MODIS data for applications in coastal areas and inland water bodies where it is needed the most.

As Lac des Allemands is a relatively small lake, the spatial resolution of SeaWiFS is not adequate since the spatial variability within the lake is much higher. The spatial resolution of OCM and its full suite of SeaWiFS-equivalent spectral bands warrant a thorough analysis in this

region. Together with higher spatial resolution, a suitable atmospheric correction procedure is essential to carry out accurate measurements. In the SeaWiFS data processed through SeaDAS, this lake is often flagged and masked out due to failure of SeaDAS to produce valid retrievals. Unlike SeaDAS for SeaWiFS, OCM doesn't have a standard processing software package for atmospheric correction. The principle of atmospheric correction for the ocean has been reviewed by Gordon (1997), however in practice it is hard to find the solutions in one place (Hu et al., 2004). Hence, there was a need for the development of an atmospheric correction procedure to utilize the full potential of OCM for studying smaller water bodies. These small inland water bodies are often shallow and turbid. Therefore, the atmospheric correction procedure needed the capability to process turbid Case 2 waters accurately.

Hu et al. (2000) developed a method of atmospheric correction for turbid coastal waters by using the aerosol characteristics of a non-turbid adjacent region, then transferring it to the turbid region and making all the corrections for it with an assumption that type of aerosol doesn't vary much over relatively short spatial scales. In this way, the authors were able to retrieve information from more turbid pixels and could get more realistic estimates of different constituents, for the pixels which had suffered either "chlorophyll algorithm failure", "negative water-leaving radiance", or "turbid water" flags. D'Sa et al. (2002) applied this turbid water correction of Hu et al. (2000) to SeaWiFS data of the Florida Shelf and Florida Bay and compared the results to the atmospheric correction schemes used in the standard SeaWiFS data processing in SeaDAS. They indicated improved performance upon using the Hu et al. (2000) turbid water atmospheric correction algorithm.

SeaDAS enforces a rigorous atmospheric correction but, on the other hand, it is comprised of a complex series of programs which are difficult to modify as a user to obtain valid

retrievals over Case 2 waters. Quantitative use of satellite data relies completely on the accuracy of atmospheric correction. From a user's standpoint, use of a software package for atmospheric correction often appears as a black-box since the user doesn't have the ability to alter the software. In addition, the comprehensive suite of atmospheric correction procedures is not available in the literature as a simple and easy-to-understand procedure for researchers who are not experts in atmospheric correction. Hence, there was a need for an atmospheric correction procedure, simple but detailed enough, which can be easily modified to incorporate the Hu et al. (2000) turbid-water atmospheric correction algorithm or other modifications.

In addition to an accurate atmospheric correction procedure, a consistent vicarious calibration is also required to achieve the level of accuracy desired for quantitative oceanographic applications (Franz et al., 2007). Vicarious calibration adjusts the variations resulting from integrated instrument and atmospheric correction procedure to retrieve normalized water-leaving radiances that are in agreement with ground truth measurements. Amongst all the ocean color sensors, SeaWiFS had one of the most comprehensive and effective vicarious calibration programs in place (McClain et al., 2000) and it was continuously monitored for variations in all bands using several direct methods and well calibrated instruments at the MOBY (Marine Optical Buoy) site close to Hawaii (Barnes et al., 2001; Eplee et al., 2001; Suresh et al., 2006). In the absence of regular ground truth data, it is imperative that SeaWiFS normalized water-leaving radiances from Case 1 clear-water locations could proxy for ground truth data when the overpass time of the sensor under investigation is close to SeaWiFS overpass time and its bands are similar to SeaWiFS. OCM was not well calibrated necessitating the use of SeaWiFS to adjust OCM's radiance values to a standard that is well calibrated over its entire life. Therefore, OCM data was vicariously calibrated using SeaWiFS data as reference.

### 2.1.3 Satellite Remote Sensing of Phytoplankton

Satellite remote sensing measurements provide a practical means for monitoring the spatial and temporal variation of near surface phytoplankton (McClain et al., 1998; Liew et al., 2000). For example, it is well understood that Chl *a*, the primary photosynthetic pigment in phytoplankton, absorbs relatively more blue and red light than green, as the spectrum of backscattered sunlight or color of ocean water progressively shifts from deep blue to green as the concentration of phytoplankton increases (O'Reilly et al., 1998). Some phytoplankton groups contain accessory pigments specific to a smaller group of phytoplankton. For example, dinoflagellates contain peridinin, cryptophytes contain alloxanthin, diatoms contain fucoxanthin and diadinoxanthin, and cyanobacteria contain zeaxanthin, echinenone and phycobiliproteins (Jeffrey and Vesk, 1997; Kutser, 2009). It has been shown that the concentration of the pigment phycocyanin (PC), the blue phycobilliprotein, can be used to estimate the concentration and distribution of fresh-water cyanobacteria from remotely sensed data (Dekker et al., 1993; Schalles and Yacobi, 2000; Vincent et al., 2004; Simis et al., 2005; Kutser et al., 2006; Hunter et al., 2008, Mishra et al., 2009; Hu et al., 2010; Wynne et al., 2010).

Schalles and Yacobi (2000) assumed that variation at 625 nm is PC dependent and 650 nm is PC independent and developed a PC algorithm with the 650 and 625 nm ratio. The baseline algorithm by Dekker et al. (1993) draws a baseline between 648 and 600 nm and derives PC concentration from the distance of the midpoint of the baseline to the reflectance at 624 nm. More recently, a nested band-ratio algorithm was developed by Simis et al. (2005). An algorithm is most useful if it can quantify the algal concentrations from satellite data. The Schalles and Yacobi (2000) approach uses 625 nm and 650 nm, and the Dekker et al. (1993) approach uses 600, 624 and 648 nm. These wavelengths are not centered at band settings of any satellite sensor

with global coverage. Therefore, the algorithms by Dekker (1993) and Schalles and Yacobi (2000) cannot yet be applied to operational satellite sensors with global coverage as the required wavebands are lacking (Ruiz-Verdu et al., 2008). The nested band-ratio algorithm by Simis et al. (2005) was developed keeping in mind the MERIS band settings. However, it did not produce the desired results when applied to MERIS data (Simis et al., 2006; Ruiz-Verdu et al., 2008). It was shown to be limited by sensitivity of the atmospheric correction procedure to high NIR reflectances over turbid water pixels and near land (Simis et al., 2006; Ruiz-Verdu et al., 2008).

In this study, an atmospheric correction procedure for the OCM sensor has been developed following that of SeaWiFS with the capability to accurately process Case 2 waters. New algorithms were developed for estimating cyanobacteria by quantifying PC and Chl *a* using Oceansat-1 OCM data. The algorithms for PC were developed utilizing OCM bands less than 600 nm. The effects of optically active constituents influencing PC and Chl *a* retrievals were modeled and subtracted. OCM data is used for both development and validation of the algorithms.

## **2.2. Field Data Collection and Laboratory Analyses**

Field data were collected from November 2006 through November 2007 and in the summer of 2009. From November 2006 to February 2007, monthly field trips were undertaken, from March to August 2007, weekly trips were undertaken, and from September to November 2007 sampling frequency was reduced to bi-weekly. These trips were planned targeting clear-sky conditions over the study area when possible. During each trip, twelve sites in Lac des Allemands were sampled (Fig. 1.1). The field data included the collection of water samples in clean Nalgene bottles, *in situ* water quality data using a YSI (Yellow Springs Instrument) 6600 probe and *in situ*  $R_{rs}$  measurements using a GER (Geophysical and Environmental Research)

1500 spectro-radiometer. The water samples were collected for High Performance Liquid Chromatography (HPLC) photopigments, the cyanobacteria unique pigment PC, Colored Dissolved Organic Matter (CDOM), Suspended Particulate Matter (SPM), toxin, and microscopic analyses. In the summer of 2009, six field trips were undertaken to obtain a dataset for the purpose of algorithm validation. The same suite of field measurements was obtained on the field trips in 2009. In addition, the absorption coefficients of total particulate, phytoplankton and non-algal particulate matter (NAP) were measured in the laboratory from the water samples collected on these field trips using the quantitative filter pad technique (QFT). An overview of the field data collected and laboratory analyses performed during 2006-2007 and 2009 is summarized in Table 2.2 and Table 2.3, respectively.

#### 2.2.1. Analyses of Water Samples

##### 2.2.1.1. HPLC Analysis of Photopigments

On every field trip, surface water samples (2 Liters) with two replicates were collected at the twelve sites, which were transferred on ice to the laboratory. For the determination of Chl *a* concentrations, replicate 100 ml aliquots of surface water were filtered (<50 kPa) onto 4.7 cm diameter glass fiber filters (Whatman GF/F), immediately frozen, and stored at -80 °C. The filter papers were shipped overnight on dry ice to Dr. James L. Pinckney at the Department of Biological Sciences, University of South Carolina, Columbia, for high performance liquid chromatography (HPLC) analysis (Pinckney et al., 1996). HPLC analysis of filtered water samples provided concentrations of 40 algal pigments including Chl *a* and the cyanobacteria specific pigments echinenone, myxo-xanthophyll and zeaxanthin. ChemTax was used to calculate the absolute abundances of major algal groups in Lac des Allemands from the HPLC pigment data (Mackey et al. 1996). For ChemTax, an iterative scheme (Latasa, 2007) was

Table 2.2 Summary of field data collection in 2006-2007. Clear-sky OCM data were obtained on the dates shown with ‘\*’.

Serial No.	Date	Laboratory Analyses						Radiometer	YSI	Water Depth
		HPLC	PC	CDOM	SPM	Microscopic	Toxin			
1	Sep 11, 2006	Only at S11								
2*	Nov 17, 2006	x			x				x	x
3*	Dec 19, 2006	x		x	x	x			x	x
4*	Jan 10, 2007	x		x	x	x		x	x	x
5	Feb 19, 2007	x		x	x	x			x	x
6	Mar 23, 2007	x		x	x	x		x	x	x
7	Mar 29, 2007	x	x	x	x	x			x	x
8*	Apr 12, 2007	x	x	x	x	x	x		x	x
9*	Apr 20, 2007	x	x	x	x	x	x		x	x
10*	Apr 26, 2007	x	x	x	x	x	x		x	x
11	May 14, 2007	x		x	x	x	x		x	x
12*	May 18, 2007	x	x	x	x	x	x		x	x
13	May 24, 2007	x		x	x	x	x		x	x
14	June 01, 2007	x		x	x	x	x	x	x	x
15	June 15, 2007	x		x	x	x	x		x	x
16*	June 21, 2007	x	x	x	x	x	x	x	x	x
17	June 29, 2007	x		x	x	x	x	x	x	x
18	July 09, 2007	x		x	x	x	x	x	x	x
19	July 18, 2007	x		x	x	x	x		x	x
20	July 26, 2007	x		x	x	x	x		x	x
21	Aug 03, 2007	x		x	x	x		x	x	x
22	Aug 15, 2007	x		x	x	x		x	x	x
23	Aug 23, 2007	x		x	x	x		x	x	x
24	Aug 31, 2007	x		x	x	x		x	x	x
25	Sept 06, 2007	x		x	x	x			x	x
26	Sept 20, 2007	x		x	x	x			x	x
27	Sept 27, 2007	x		x	x	x			x	x
28*	Oct 11, 2007	x	x	x	x	x		x	x	x
29	Oct 25, 2007	x		x	x	x			x	x
30	Nov 08, 2007	x		x	x	x			x	x

Table 2.3 Summary of field data collection in 2009. Clear-sky OCM data were obtained on the dates shown with ‘\*’.

Serial No.	Date	Laboratory Analyses						Radiometer	YSI	Water Depth
		HPLC	PC	CDOM	SPM	Microscopic	Absorption			
1	May 1, 2009	x	x	x	x	x	x		x	x
2	May 13, 2009	x	x	x	x	x	x	x	x	x
3*	May 19, 2009	x	x	x	x	x	x		x	x
4*	May 29, 2009	x	x	x	x	x			x	x
5*	June 18, 2009	x	x	x	x	x			x	x
6*	June 30, 2009	x	x	x	x	x		x	x	x



followed using the initial pigment ratios from published ratios (Pinckney et al., 2009; Schlüter et al. 2006). Iterations were successively performed until the ratios in the output matrix remained constant (8 iterations). The ChemTax analysis was limited to cyanobacteria, euglenophyte, chlorophyte, dinoflagellate, cryptophyte, diatom, and chrysophyte groups.

#### 2.2.1.2. Phycocyanin Analysis

Subsamples (50 ml aliquots of surface water) were filtered (<50 kPa) onto polycarbonate filters with 4.7 cm diameter and 0.2  $\mu\text{m}$  pore size, and kept frozen (-20 °C) until analysis for determination of PC concentrations. PC was extracted from the filtered water samples of selected dates according to Downes and Hall (1998) with 0.05M Tris buffer (pH 7). Tris buffer solution was prepared by first dissolving 6.057 gram of Tris base ( $\text{C}_4\text{H}_{11}\text{NO}_3$ ) in 500 ml of deionized water. Using a pH meter, the solution of Tris was titrated with 1M hydrochloric acid (HCl) until pH 7 was reached. Deionized water was added to the Tris-HCl mixture for preparing a total of 1 liter of 0.05M Tris buffer (pH 7) solution. The filter paper was placed in a 15 ml centrifuge tube with 5 ml of the Tris buffer solution and sonicated using a Misonix Sonicator 3000 with a micro-tip sonication probe for 2 min at 30-40 W maintaining the sample tubes on ice bath at all times. After sonication the sample tubes were incubated in the dark for 1 h at 4 °C and then centrifuged for 10 min at 3000 RPM with a relative centrifugal force of 1,240g in an IEC Centra CL2 centrifuge (Thermo Electron Corp.). Fluorescence was measured using a Horiba Jovin Yvon FluoroMax®-4 Spectrofluorometer with  $\lambda_{\text{EX}} = 615 \text{ nm}$  and  $\lambda_{\text{EM}} = 647 \text{ nm}$ . A PC standard curve was constructed using a five point PC standard (C-Phycocyanin, Prozyme, Inc) calibration set (10, 30, 55, 75, and 100  $\mu\text{g/L}$ ). Using this standard curve equation ( $y = mx + c$ ), the sample fluorescence values were interpolated. Finally, PC concentration was computed by adjusting for the volume of filtered water sample and Tris buffer solution as

$$PC (\mu g/L) = \frac{[PC] \times 0.005}{0.05} \quad (2.1)$$

To determine the specific absorption coefficients of PC, first a dilution series of concentrations 1 to 100  $\mu g/L$  with 10  $\mu g/L$  interval was prepared from the PC standards (Prozyme Inc.) and the absorption coefficients were measured using a Perkin Elmer Lambda 850 spectrophotometer. Subsequently, these absorption coefficients were divided by PC concentrations to determine the specific absorption coefficient of PC for each dilution. The average specific absorption coefficient of PC, which is presented in Fig. 1.3, was determined by taking the average specific absorption coefficients over PC of all the concentrations.

#### 2.2.1.3. Measurement of CDOM Absorption Coefficients

For the measurement of spectral absorption coefficients of CDOM, 50 ml of water sample was filtered under a low vacuum through Nuclepore membrane filters with 47 mm diameter and 0.2  $\mu m$  pore size. Filtrate samples were stored in clean amber colored glass bottles and refrigerated at 4 °C. For absorbance measurements, the filtrate samples were allowed to reach ambient room temperature. Absorbance measurements were performed using a multiple path-length aqueous capillary waveguide (WPI, Inc.), which is a single-beam spectrophotometer (D'Sa et al., 1999; D'Sa and Steward, 2001). The absorbance spectra ( $A$ ) between 187 nm and 722 nm at 1 nm interval were determined by 4 scans: one of a cell filled with blank solution (Milli-Q water) and three of the sample replicates. For processing the absorbance data, as a first step the average absorbance at 701-722 nm was considered as a baseline and corrected by subtracting from the absorbance at each wavelength for 400-700 nm. The absorption coefficient at each wavelength for 400-700 nm,  $a(\lambda)$  ( $m^{-1}$ ), was obtained from the relationship (D'Sa et al., 1999)

$$a(\lambda) = 2.303 A(\lambda)/l \quad (2.2)$$

where  $A(\lambda)$  is the absorbance and  $l$  is the cell path length in meters. Finally, the CDOM spectral absorption coefficients were determined by averaging the absorption coefficients of the three replicates.

CDOM spectral absorption coefficients ( $a_{CDOM}(\lambda)$ ) generally decreased approximately exponentially from 400 to 700 nm for all the samples.  $a_{CDOM}(\lambda)$  as a function of wavelength, is commonly modeled with an exponentially decreasing function (Bricaud et al., 1981) as:

$$a_{CDOM}(\lambda) = a_{CDOM}(\lambda_0) e^{-S(\lambda-\lambda_0)} \quad (2.3)$$

where  $\lambda_0$  is a reference wavelength at 440 nm, and  $S$  is the spectral slope parameter. The spectral slopes,  $S$  ( $\text{nm}^{-1}$ ), were calculated from plots of the natural logarithm of the absorption coefficient versus wavelength using the linear least-squares regression over the interval 400-560 nm. For Lac des Allemands,  $S$  varied between 0.012 and 0.022.  $a_{CDOM}$  values for all the wavelengths were extrapolated from  $a_{CDOM}(440)$  using the above computed  $S$  values.

#### 2.2.1.4. Analysis of Suspended Sediments

SPM concentrations were determined by following the glass fiber filter method (USGS, 1987). Recorded volumes of water samples were filtered through pre-weighed GF/F filters and the increase in weight of the filter after drying at 105 °C was measured as SPM. Ashing the residue at 500 °C provided the inorganic sediment fraction or suspended particulate inorganic matter (SPIM). Subsequently, the organic fraction or the suspended particulate organic matter (SPOM) was determined by subtracting SPIM from SPM.

#### 2.2.1.5. Microscopic and Toxin Analyses

Subsamples (100 ml) of water samples were fixed with 1% glutaraldehyde to determine species composition and abundance of cyanobacteria and refrigerated in the dark at 4 °C until

analysis. Enumeration of all the species of cyanobacteria present in the water samples was performed by microscopic cell counts under a compound microscope and using an imaging microscope (Fluid Imaging Technologies) by Garcia et al. (2010). Subsamples (100 ml aliquots) of surface water were collected between April and July 2007, filtered (<40 kPa) onto 2.5 cm diameter glass fiber filters (Whatman GF/F), and kept frozen (20 °C) until analysis for determination of particulate microcystin concentrations. Microcystin analysis was performed using an enzyme-linked immunosorbent assay (ELISA) kit for both the filtered surface water samples and blue crab tissues in this earlier study (Garcia et al., 2010).

#### 2.2.1.6. Particulate Absorption Measurements

Subsamples (100 ml) of water samples collected in the summer of 2009 were filtered to determine total particulate, phytoplankton and NAP absorption coefficients in the laboratory. Discrete water samples were filtered under low vacuum onto Whatman GF/F glass fiber filters with 25 mm diameter and 0.7 µm pore size, and stored in liquid nitrogen until analysis. On the day of the analysis, the samples of selected three field trips were first thawed to room temperature after removing from liquid nitrogen by keeping them in the dark at room temperature for thirty minutes. Filter paper blanks were prepared by filtering 15 ml of Milli-Q water. Absorbance was measured by scanning the sample and blank filter papers using a Perkin Elmer Lambda 850 spectrophotometer from 190 to 750 nm at 2 nm intervals.

To correct for residual scattering offsets in the absorption measurements the mean value from 700 to 750 nm was subtracted from the corresponding entire spectra for both sample and blank absorbance. Contributions due to non-particulate absorption were removed by subtracting blank absorbance at each wavelength from sample absorbance at corresponding wavelengths. Glass-fiber filters, which act as optical diffusers are commonly used for absorption

measurements in the laboratory, but correction for the increase in effective pathlength caused by multiple scattering within the filters (pathlength amplification factor,  $\beta$ ) is required (Cleveland and Weidemann, 1993). Pathlength amplification was corrected by using the relationship (Cleveland and Weidemann, 1993)

$$A_P(\lambda) = 0.378 A_{Filt}(\lambda) + 0.523 A_{Filt}(\lambda)^2 \quad (2.4)$$

where  $A_P(\lambda)$  and  $A_{Filt}(\lambda)$  represent absorbance of total particulate matter and filter, respectively. Absorbance of particulate matter was converted to absorption coefficient by using the equation (Cleveland and Weidemann, 1993)

$$a_p(\lambda) = \frac{2.3[A_P(\lambda)]}{V/A} \quad (2.5)$$

where  $a_p(\lambda)$  ( $\text{m}^{-1}$ ),  $V$  ( $\text{m}^3$ ) and  $A$  ( $\text{m}^2$ ) represent the total particulate absorption coefficient, volume filtered and the area of the filter paper, respectively.

To decompose the total particulate absorption coefficients into NAP absorption coefficients and phytoplankton absorption coefficients, after measuring the total particulate absorption coefficients, the sample filter papers were extracted with methanol following the method described in Mitchell et al. (2002) and Naik et al. (2010). The sample filter paper was set up in the filtration apparatus and 15 ml of methanol was filtered after immersing the filter paper for 30 minutes. Methanol extraction dissolves the phytoplankton component. Subsequently, absorbance was measured using the Perkin Elmer Lambda 850 spectrophotometer and the absorbance spectra was examined for any residual phytoplankton signature, such as the 676 nm Chl *a* absorption peak. In the case when a 676 nm peak was observed, the sample filter paper was extracted with methanol again and then the absorbance was measured. Subsequent scanning

of the sample filter paper provided NAP absorbance,  $A_{NAP}(\lambda)$  which was converted to  $a_{NAP}(\lambda)$  using Eq. 2.2.

The phytoplankton absorption coefficients were computed by subtracting the absorption coefficients of NAP from the absorption coefficients of total particulate matter. The specific absorption coefficients of phytoplankton were computed by dividing these phytoplankton absorption coefficients by Chl *a* concentrations obtained from the HPLC analysis and then computing the average. For the specific absorption coefficients of NAP, first NAP concentrations were determined by subtracting Chl *a* concentrations from gravimetrically determined SPM after conversion of Chl *a* concentrations from  $\mu\text{g/L}$  to  $\text{mg/L}$ . Subsequently, the specific absorption coefficients of NAP were computed by dividing NAP absorption coefficients by NAP concentrations and averaging all the NAP specific absorption coefficients.

#### 2.2.2. *In Situ* Water Quality Data Using YSI Instruments

Using a YSI 6600 instrument, profiles of water temperature, specific conductivity, salinity, dissolved oxygen (DO), water depth, pH, optical backscatter, and Chl *a* concentrations were measured at each of the water sampling sites on every field trip. Additionally, two YSI sondes were deployed at 0.5 m approximately from the water surface; one in Lac des Allemands (at site S11) and another where Bayou des Allemands meets Lake Salvador. The YSI 6600 sensor in Lac Des Allemands site provided continuous (at 30-min intervals) water temperature, specific conductivity, salinity, pressure, water depth, optical backscatter, Chl *a* concentrations, PC concentrations, and dissolved oxygen (DO), whereas the YSI 600 instrument at the Lake Salvador site provided temperature, salinity, and water depth. They were self-cleaning, thus increasing the collection of high quality data and reducing field costs. Nevertheless, to maintain the integrity of the data, the YSI instrument deployed in Lac des Allemands was checked for

fouling, batteries replaced and data downloaded on each field trip. The YSI instrument deployed in Lake Slavador was serviced monthly. The time series of Chl *a* concentrations and temperature measured by the YSI 6600 instrument deployed in Lac des Allemands are shown with Chl *a* concentrations at the water surface and at the sensor depth obtained from HPLC analysis in Fig. 2.1. The Chl *a* concentrations suggest the start of an algal bloom as temperature warmed in late February, 2007 reaching to the largest bloom in the month of April and May 2007. With a further increase in temperature ( $> \sim 25^{\circ}\text{C}$ ), the phytoplankton bloom senesced.

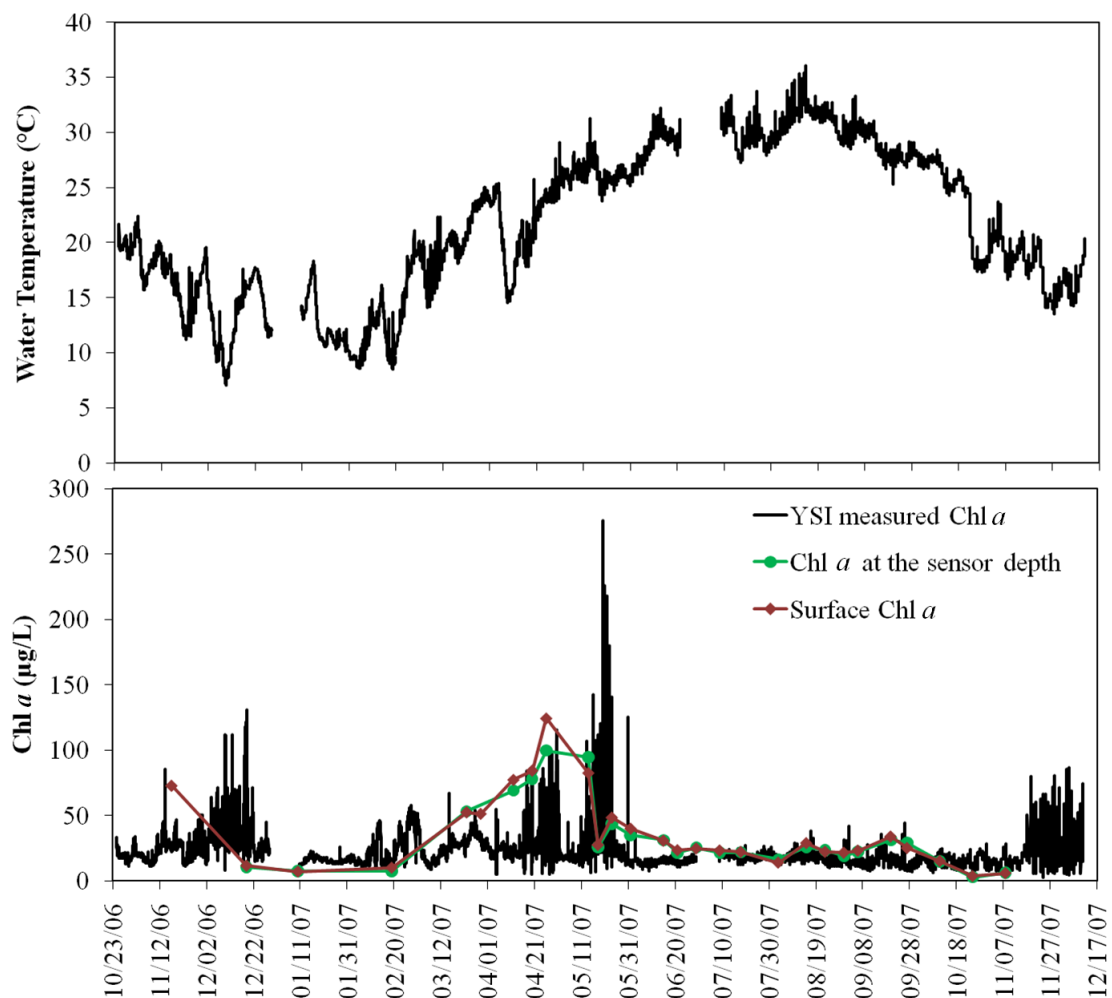


Fig. 2.1 YSI measured time series of Chl *a* concentrations and water temperature at the YSI instrument deployment site in Lac des Allemands from October 24, 2006 through December 11, 2007. HPLC Chl *a* at the water surface from November 17, 2006 through November 8, 2007 and at the sensor depth from December 17, 2006 through November 8, 2007 are shown with the YSI Chl *a* with sampling days indicated (*see* Table 2.2 for the list of sampling days).

Other water quality parameters including time series of salinity, DO, optical back-scatter, and PC concentrations measured by the YSI 6600 instrument deployed in Lac des Allemands are shown in appendix A. Water level at the YSI instrument deployment sites in Lac des Allemands and Lake Salvador, and the water level anomalies in comparison with mean daily discharge at the Davis Pond Diversion are also shown in appendix A.

### 2.2.3. *In Situ* $R_{rs}$ Measurements

*In situ*  $R_{rs}$  from 299 nm to 1096 nm was determined from above-water measurements on selected field trips. To derive above water  $R_{rs}$  three measurements are generally required: (1) upward radiance ( $L_u$ ), (2) downward sky radiance ( $L_{sky}$ ), and (3) upward radiance from a standard Spectralon reflectance plaque ( $L_{plaque}$ ). First, measurements of radiance from a plaque with known spectral directional reflectance (10% Spectralon, Labsphere) were made using the fiber-optic-based high-spectral-resolution GER 1500 radiometer. Subsequently, three replicate scans of target water surface were made at an angle  $30^\circ$  to the vertical and then sky radiance was measured by pointing the radiometer towards the sky opposite to the sun. The radiometer data were processed following Hu (2003) for the determination of above water  $R_{rs}$ . First, water-leaving radiance ( $L_w$ ) was determined by

$$L_w = L_u - (0.02 \times L_{sky}) \quad (2.6)$$

Subsequently,  $R_{rs}$  was computed by

$$R_{rs} = \frac{L_w}{10 \times L_{plaque} \times \pi} \quad (2.7)$$



## CHAPTER 3

### ATMOSPHERIC CORRECTION AND VICARIOUS CALIBRATION OF OCEANSAT-1 OCM DATA

#### 3.1. Introduction

Satellite remote sensing provides a valuable tool for rapidly assessing the spatial variability of water quality parameters over synoptic scales (Gould and Arnone, 1997). However, use of satellite remote sensing for monitoring small lakes and estuaries is a challenge due to the optical complexities of these Case 2 water bodies leading to atmospheric correction problems (“Case 1” and “Case 2” defined in Morel and Prieur, 1977). One such small lake is Lac des Allemands in Louisiana, USA, where high concentrations of cyanobacteria are known to occur in spring and summer (Dortch et al., unpublished data; Swenson et al., unpublished data; Rabalais et al., unpublished data; Ren et al., 2009; Garcia et al., 2010; Dash et al., in press).

Operational satellite monitoring of small water bodies requires higher spatial and temporal resolution (Kutser, 2009). The Oceansat-1 satellite launched on May 26, 1999 carried the OCM sensor with spectral bands nearly identical to the SeaWiFS sensor. SeaWiFS and MODIS ocean bands have high radiometric sensitivity (Hooker et al., 1993; O’Reilly et al., 1998), however, they lack the spatial resolution needed for studying smaller water bodies. Other ocean color sensors that have the required spatial resolution for studying smaller water bodies, lack frequent revisit cycles. The Oceansat-1 OCM sensor provides a compromise between the two types of sensors discussed above with a spatial resolution of  $360 \times 236$  m and an exact revisit period of alternate days.

OCM acquired data for a period of eleven years since 1999, but these data have not been used extensively by the scientific community for studying Case 2 waters despite its higher spatial resolution. This is possibly due to one or more of the following: a lack of reliable atmospheric

correction procedure and bio-optical algorithms for the sensor over Case 2 waters, the timing of its launch immediately following the launch of the long-awaited SeaWiFS instrument, and difficulty in data access by the scientific community (Crowley, 2003). Nevertheless, the high resolution OCM data has strong potential for ocean color research especially in coastal waters. In addition, its successor, the OCM-2 sensor, was launched on September 23, 2009, and OCM-3 is planned for launch in 2013 (ISRO, 2010). With the recent failure of the SeaWiFS instrument, OCM series of sensors are potential alternatives for the ocean color data continuity.

In ocean color remote sensing, the water-leaving radiance forms a small fraction of the total radiance received by the sensor, with the main contribution being due to the atmosphere. The NASA SeaWiFS Data Analysis System (SeaDAS) is one of the most comprehensive atmospheric correction programs that processes ocean color data from several sensors including SeaWiFS, MODIS, OCTS, CZCS and MERIS. The SeaDAS processed SeaWiFS or MODIS data over Case 1 waters is widely used by the ocean color community. However, SeaDAS processed data generally fail to deliver the Case 1 type accuracy in shallow coastal Case 2 waters (Hu et al., 2000; Wang and Franz, 2000; D'Sa et al., 2002; Kutser, 2009). The SeaDAS atmospheric correction procedure assumes the water-leaving radiance to be negligible in the near infrared (NIR) which is one of the major reasons for its failure in Case 2 waters, because NIR reflectance is not zero in waters with high chlorophyll *a* (Chl *a*) and suspended sediments. Iterative approaches have been incorporated in SeaDAS software to correct for this problem (Arnone et al., 1998; Stumpf et al., 2003; Siegel et al., 2000). However, due to the presence of even modest quantities of the constituents such as, suspended sediments or CDOM, which do not co-vary with Chl *a*, SeaDAS processing fails in coastal waters and either produces negative water-leaving radiances or masks the pixels.

Due to its small size and optical complexities, Lac des Allemands is often flagged and masked out in the SeaWiFS data processed through SeaDAS. OCM data with its higher spatial resolution and SeaWiFS equivalent spectral bands is an appropriate sensor for the study of small lakes such as Lac des Allemands. However, unlike SeaDAS for SeaWiFS, OCM does not have a standard processing software for atmospheric correction. Preliminary results showed that the existing data processing software including SeaSpace Terascan™, ENVI FLAASH, and SeaDAS failed in Lac des Allemands for atmospheric correction of OCM data. Hence, there was a need for the development of an atmospheric correction procedure with the capability to process turbid Case 2 waters to utilize the full potential of OCM. Hu et al. (2000) developed a method of atmospheric correction for SeaWiFS data over turbid coastal waters by using the aerosol characteristics of a non-turbid adjacent region with an assumption that the type of aerosol does not vary much over relatively short spatial scales. They were able to retrieve realistic estimates of several in-water constituents from SeaWiFS turbid pixels, which had been flagged with either “negative water-leaving radiance” or “turbid water” flags in the SeaDAS processing. SeaDAS enforces a rigorous atmospheric correction but, on the other hand, it is comprised of a complex suite of programs which is difficult to modify as a user. The principle of atmospheric correction for the ocean has been reviewed by Gordon (1997), however in practice it is hard to find the solutions in one place (Hu et al., 2004), especially in the case of OCM. In this study, an atmospheric correction procedure was written for the processing of OCM data based on the extensive work done for SeaWiFS. The Hu et al. (2000) aerosol correction technique has been incorporated in this procedure to increase the efficacy of the atmospheric correction over turbid-water pixels.

In addition to an accurate atmospheric correction procedure, a consistent vicarious calibration is also required to achieve the level of accuracy desired for quantitative oceanographic applications (Franz et al., 2007). Amongst all the ocean color sensors, SeaWiFS had the most comprehensive vicarious calibration program in place (McClain et al., 2000) and it was continuously monitored for calibration errors using several direct methods and well-calibrated instruments such as one at the MOBY site near Hawaii (Barnes et al., 2001; Clark et al., 2001; Eplee et al., 2001; Suresh et al., 2006). As the OCM sensor has identical bands and a similar equatorial crossing time to SeaWiFS, OCM data were vicariously calibrated using SeaWiFS data as reference.

In this study, an atmospheric correction procedure for OCM sensor was developed following that of SeaWiFS with the capability to accurately process Case 2 water bodies. In addition, a vicarious calibration procedure was developed and new coefficients were applied to the OCM data. These procedures were implemented on OCM data at “clear-water” pixels and the results were compared with co-located SeaWiFS data processed with the same procedure and with the SeaDAS output. These procedures were then applied to the OCM data of Lac des Allemands and compared with field measurements and SeaDAS output. It was demonstrated that valid normalized water-leaving radiances ( $nL_w$ ) and remote sensing reflectances ( $R_{rs}$ ) could be retrieved over Case 1 as well as Case 2 waters using the combined vicarious calibration and atmospheric correction procedure developed in this study.

## **3.2. Materials and Methods**

### **3.2.1 Satellite Data Processing Overview**

OCM data were received via an X-band antenna and processed at the Earth Scan Laboratory, Louisiana State University. Raw OCM data were calibrated by converting raw

counts to radiance values for the eight OCM spectral bands using the SeaSpace Terascan™ software. Six relatively clear-sky OCM images over the Gulf of Mexico were chosen from 2004 to 2007 (Table 3.1). SeaWiFS MLAC data of the same dates and similar overpass times over the Gulf of Mexico were obtained from NASA's Ocean Color website ([oceancolor.gsfc.nasa.gov](http://oceancolor.gsfc.nasa.gov)) and processed through SeaDAS 6.0. Based on the SeaWiFS derived Chl *a* images, one “clear-water” (Chl *a* conc. < 0.5 µg/L) site from the northern Gulf of Mexico was chosen in a clear-sky region in each of the SeaWiFS and OCM images. These clear water sites are indicated as squared dots in the SeaDAS processed SeaWiFS Chl *a* images (Fig. 3.1). Comparison of OCM and SeaWiFS geometries and attributes at the six atmospheric correction sites on the six dates is given in Table 3.1.

Table 3.1. Comparison of OCM and SeaWiFS attributes and geometries at the six atmospheric correction sites on the six dates.

Parameters	OCM	SeaWiFS	OCM	SeaWiFS	OCM	SeaWiFS
Date	5-Nov-04	5-Nov-04	7-Nov-04	7-Nov-04	19-Dec-04	19-Dec-04
Time of pixel scan	18:05:43	18:55:33	18:06:05	18:38:46	18:05:47	19:09:18
Latitude	28.198	28.198	26.504	26.504	27.702	27.702
Longitude	-92.001	-92.001	-89.001	-89.001	-91.802	-91.802
Ozone Conc. (DU)	267	267	275	275	280	280
Satellite Zenith Angle	37.770	25.297	22.293	22.544	36.224	42.222
Solar Zenith Angle	44.847	46.786	44.047	45.372	51.031	53.455
Satellite Azimuth Angle	128.044	221.578	168.388	204.667	130.264	253.689
Solar Azimuth Angle	184.652	201.311	188.896	200.078	180.242	198.544
Sat_az - 180 - Sol_az	-236.608	-159.733	-200.507	-175.411	-229.977	-124.855
Relative Azimuth Angle	123.391	-159.733	159.492	-175.411	130.022	-124.855
Pressure	1023.73	1023.73	1020.44	1020.44	1024.73	1024.73
Parameters	OCM	SeaWiFS	OCM	SeaWiFS	OCM	SeaWiFS
Date	17-Nov-06	17-Nov-06	20-Apr-07	20-Apr-07	21-Jun-07	21-Jun-07
Time of pixel scan	18:03:58	18:54:48	18:03:04	19:06:09	18:02:59	19:45:16
Latitude	27.099	27.099	28	28	27.54	27.54
Longitude	-92.1	-92.1	-91.001	-91.001	-90.55	-90.55
Ozone Conc. (DU)	278	278	286	286	301	301
Satellite Zenith Angle	37.110	41.733	32.523	31.258	30.426	49.963
Solar Zenith Angle	46.643	48.527	16.588	22.102	3.879	23.191
Satellite Azimuth Angle	129.368	125.144	135.770	140.678	142.916	260.344
Solar Azimuth Angle	183.151	199.511	179.826	225.2	178.569	265.533
Sat_az - 180 - Sol_az	-233.782	-254.367	-224.055	-264.522	-215.653	-185.189
Relative Azimuth Angle	126.217	105.633	135.944	95.478	144.346	174.811
Pressure	1018.01	1018.01	1018.11	1018.11	1015.64	1015.64

To apply the Hu et al. (2000) aerosol correction, six additional clear-water sites were chosen based on minimum TOA radiances in NIR bands 7 and 8 in the OCM and SeaWiFS images. The TOA radiance values in bands 7 and 8 were then corrected for Rayleigh path radiance for transferring the aerosol characteristics of these pixels to the corresponding atmospheric correction sites. The additional sites for aerosol correction are also shown in Fig. 3.1. Atmospheric correction equations were then applied sequentially to the OCM TOA radiances to produce  $nL_w$  and  $R_{rs}$  before and after vicarious calibration. To compare the accuracy of the atmospheric correction procedure between OCM and SeaWiFS,  $nL_w$  and  $R_{rs}$  were produced in a similar fashion for SeaWiFS. Rayleigh and aerosol look up tables for OCM were generated (by B. Franz of OBPG, NASA) so that the OCM data could be processed through SeaDAS for comparison. The six SeaWiFS datasets were processed through both the single scattering and the default (multiple scattering) approaches in SeaDAS, which formed two more datasets. In summary, five datasets were generated including (1) OCM data processed with the atmospheric correction procedure developed in this study (hereafter termed as new code), (2) SeaWiFS data processed with the new code, (3) OCM data processed with SeaDAS, (4) SeaWiFS data processed with SeaDAS single scattering approximation, and (5) SeaWiFS data processed with SeaDAS multiple scattering approximation.

Finally, the new code was applied to the vicariously calibrated OCM data covering Lac des Allemands, located in the uppermost part of the Barataria estuary in southeastern Louisiana (Fig. 1.1). Lac des Allemands is a freshwater lake (salinity < 1 psu) with surface area of 49 km<sup>2</sup>. The same OCM data were also processed through SeaDAS and resulting  $nL_w$  values were compared to the OCM data processed through the new code. The new code results over Lac des Allemands were also compared to *in situ* radiometric measurements.

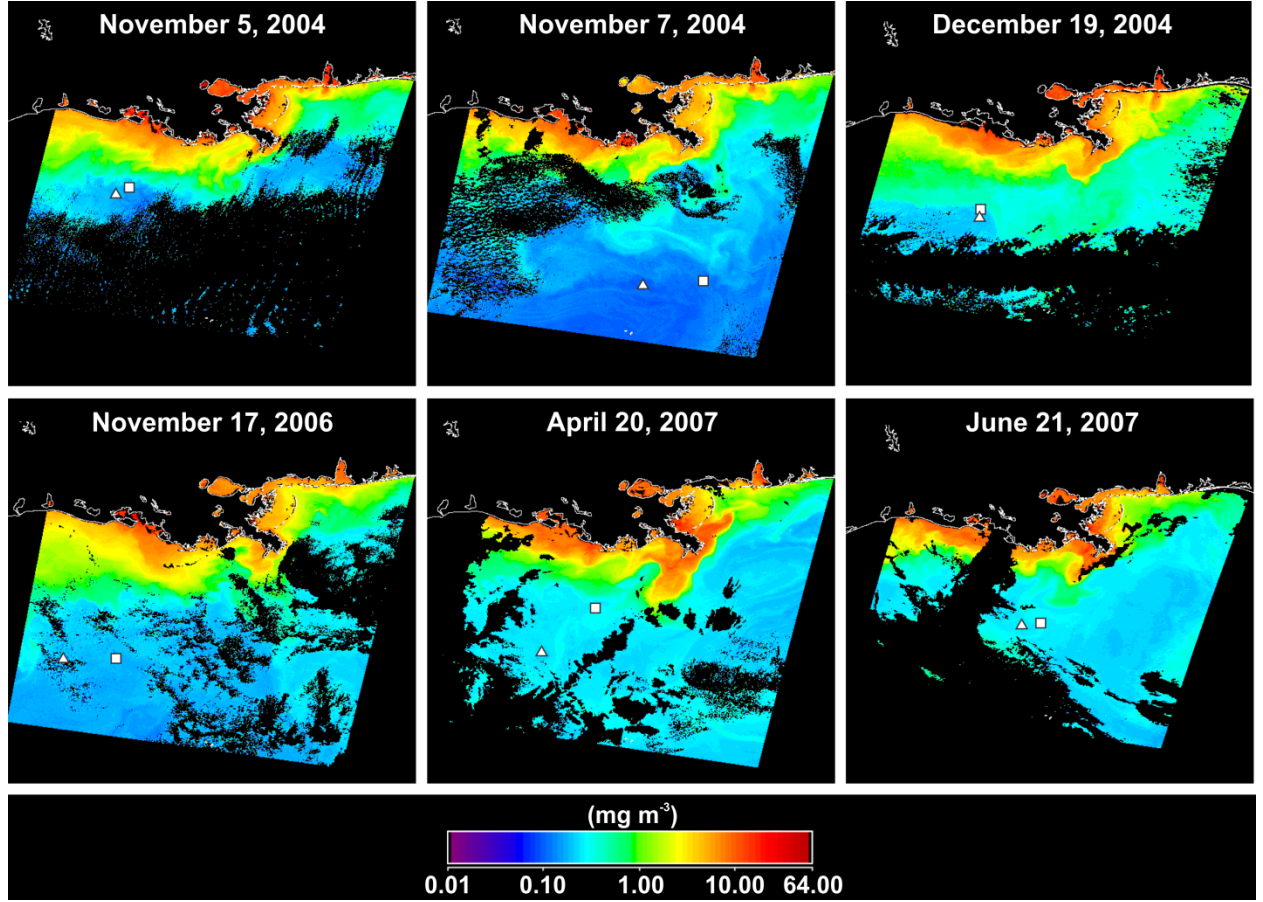


Fig. 3.1. SeaDAS processed SeaWiFS Chl *a* images of northern Gulf of Mexico. The sites represented by squared dots are the clear water locations, where atmospheric correction was performed. The sites represented by triangles are the location from which aerosol characteristics were transferred to the atmospheric correction sites.

### 3.2.2 Atmospheric Correction Procedure

In a single scattering approach, the radiance received by a space borne sensor at the top of the atmosphere (TOA) in a spectral band centered at a wavelength,  $\lambda_i$ ,  $L_r(\lambda_i)$ , can be divided into the following components (Gordon et al., 1997):

$$L(\lambda_i) = L_r(\lambda_i) + L_a(\lambda_i) + T(\lambda_i)L_g(\lambda_i) + t(\lambda_i)L_w(\lambda_i) \quad (3.1)$$

where  $L_r(\lambda_i)$  and  $L_a(\lambda_i)$  are radiance contributions associated with air molecules (Rayleigh scattering) and aerosols (including Rayleigh-aerosol interactions) respectively,  $T$  is the direct

atmospheric transmittance,  $L_g(\lambda_i)$  is the sun-glint component,  $t$  is the diffuse atmospheric transmittance, and  $L_w(\lambda_i)$  is the desired water leaving radiance.

For observations that have significant sun-glint contamination,  $T(\lambda_i)L_g(\lambda_i)$  is so large that those observations cannot be accurately corrected and must be removed (Wang and Franz, 2000; Gordon and Voss, 2004; Mishra et al., 2005). In the case of OCM sun-glint is usually avoided through tilting of the sensor. Hence, this term may be ignored, and consequently, Eq. (1) can be written as:

$$L(\lambda_i) = L_r(\lambda_i) + L_t(\lambda_i) + t(\lambda_i)L_w(\lambda_i) \quad (3.2)$$

First, contribution due to ozone absorption was removed from the TOA radiance as given by Hu et al. (2004):

$$L_t^*(\lambda_i) = L_t(\lambda_i)e^{\left[\tau_{oz}(\lambda_i)\left(\frac{1}{\cos\theta_0} + \frac{1}{\cos\theta_v}\right)\right]} \quad (3.3)$$

where  $L_t^*(\lambda_i)$  is TOA radiance measured by the satellite in the absence of ozone,  $\theta_v$  is satellite viewing zenith angle,  $\theta_0$  is solar zenith angle, and  $\tau_{oz}(\lambda)$  is ozone optical depth, which was computed as (Gordon, 1995):

$$\tau_{oz}(\lambda_i) = k_{oz}(\lambda_i) \frac{DU}{1000} \quad (3.4)$$

where  $k_{oz}(\lambda_i)$  is ozone absorption coefficient taken from Gregg and Carder (1990) and  $DU$  is ozone concentration in Dobson units obtained from the TOMS website.

**3.2.2.1 Computation of Rayleigh Path Radiance ( $L_r(\lambda_i)$ ):** Rayleigh path radiance is the contribution of Rayleigh scattering by air molecules to TOA radiance. It was computed as given by (Gordon, 1995):



$$L_r(\lambda_i) = \frac{F_0'(\lambda_i)\omega_{0r}\tau_r(\lambda_i)P_r}{4\pi \cos \theta_v} \quad (3.5)$$

where  $\tau_r(\lambda_i)$  is Rayleigh optical thickness,  $P_r$  is Rayleigh scattering phase function,  $\omega_{0r}$  is single scattering albedo (equals to 1), and  $F_0'(\lambda_i)$  is instantaneous extraterrestrial solar irradiance adjusted for the Sun-Earth distance as (Hu et al., 2004):

$$F_0'(\lambda_i) = F_0(\lambda_i) / [1.00014 - 0.01671 \cdot \cos(2\pi(0.9856002831 \cdot \text{julianday} - 3.4532868)/360) - 0.00014 \cdot \cos(4\pi(0.9856002831 \cdot \text{julianday} - 3.4532868)/360.0)^2] \quad (3.6)$$

where  $F_0(\lambda_i)$  is extraterrestrial solar irradiance. The  $F_0(\lambda_i)$  values were adopted from Pandya et al. (2002) for OCM data and from SeaDAS for SeaWiFS data processing.

3.2.2.1.1 Computation of Rayleigh Optical Thickness ( $\tau_r(\lambda_i)$ ): The value of Rayleigh optical thickness,  $\tau_r(\lambda_i)$  at any atmospheric pressure  $P$  was calculated as given by Hansen and Travis (1974):

$$\tau_r(\lambda_i) = \frac{P}{P_0} [0.008569\lambda_i^{-4} (1 + 0.0113\lambda_i^{-2} + 0.00013\lambda_i^{-4})] \quad (3.7)$$

where  $\lambda_i$  is wavelength in  $\mu\text{m}$ , and  $P_0$  is standard atmospheric pressure of 1013.25 millibars.

3.2.2.1.2 Computation of Rayleigh Scattering Phase Function ( $P_r(\theta_{\pm})$ ): The computations of Rayleigh scattering phase function involved the direct scattered light and the scattered light which is specularly reflected at the air-sea interface. It was computed as given by Doerffer (1992):

$$P_r(\theta_{\pm}) = \frac{3}{4} (1 + \cos^2 \theta_{\pm}) \quad (3.8)$$

where  $\theta_{\pm}$  represents the scattering angles. The  $-$  and  $+$  subscripts indicate the direct scattered light and direct scattered plus the specularly reflected light at the air-sea interface, respectively.

The scattering angles in the direction to the sensor and in direction to the sensor via the air-sea interface is given by,

$$\cos \theta_{\pm} = \pm \cos \theta_0 \cos \theta_v - \sin \theta_0 \sin \theta_v \cos(\Delta\phi) \quad (3.9)$$

where  $\Delta\phi$  represents the relative azimuth angle. Note that by definition the relative azimuth angle is the absolute difference between the satellite azimuth and the solar azimuth angles. In this definition the sun vector is considered in the down direction (sun to surface). However, it is a common practice (also instituted in SeaDAS) to define both the sun vector and the sensor vector in the upward direction and thus the relative azimuth angle was obtained as:

$$\Delta\phi = \phi_v - 180 - \phi_0 \quad (3.10)$$

where  $\phi_0$  and  $\phi_v$  are solar and satellite azimuth angles, respectively. Further, to keep the values between  $\pm 180^\circ$ ,  $360^\circ$  was added or subtracted when the relative azimuth angles were less than  $-180^\circ$  and greater than  $180^\circ$ , respectively.

At the air-sea interface, another phenomenon occurs with the specularly reflected light that should be accounted for in the computation of Rayleigh phase function is Fresnel reflection. It is the reflection that occurs when light propagates through media with different refractive indices. As none of the relevant media (air or water) were magnetic, when the light is polarized with the electric field of the light perpendicular to the incident light (s-polarized), the Fresnel reflection coefficient is calculated as:

$$R(\theta_i)_s = \sin^2(\theta_i - \theta_j) / \sin^2(\theta_i + \theta_j) \quad (3.11)$$

where  $\theta_i$  is solar zenith angle ( $\theta_0$ ) for  $R(\theta_0)$  and satellite viewing zenith angle ( $\theta_v$ ) for  $R(\theta_v)$  calculation, and  $\theta_j$  is determined through Snell's law as:

$$\sin(\theta_i) / \sin(\theta_j) = n = 1.333 = \text{refractive index of water} \quad (3.12)$$

When the light is polarized in the same plane as the incident light (p-polarized), the Fresnel reflection coefficient is calculated by:

$$R(\theta_i)_p = \tan^2(\theta_i - \theta_j) / \tan^2(\theta_i + \theta_j) \quad (3.13)$$

Assuming the incident light contains an equal mix of s- and p-polarizations, the Fresnel reflection coefficient was computed as Gordon (1997):

$$R(\theta_i) = 0.5[R(\theta_i)_s + R(\theta_i)_p] \quad (3.14)$$

The total Rayleigh scattering phase function was computed as given by Doerffer (1992) and Gordon and Wang (1994):

$$P_r(\theta_{\pm}) = P_r(\theta_-) + [R(\theta_v) + R(\theta_0)]P_r(\theta_+) \quad (3.15)$$

where  $P_r(\theta_{\pm})$  is total Rayleigh scattering phase function,  $P_r(\theta_-)$  is Rayleigh scattering phase function when solar radiation is directly backscattered to the sensor, and  $P_r(\theta_+)$  is Rayleigh scattering phase function due to the direct backscattered light in addition to the specularly reflected light at the air/sea interface.

3.2.2.2 Computation of Aerosol Path Radiance ( $L_a(\lambda_i)$ ): Aerosol path radiance is the contribution of scattering by particles similar to or larger than the wavelength of light such as dust, pollen, smoke or water vapor in the atmosphere to the TOA radiance. Unlike  $L_r$ , which can be computed fairly accurately,  $L_a$  is difficult to determine since the aerosol scattering is highly variable and many times there is no a priori information on their optical properties and size distributions. By using the sensor radiances above 700 nm, it is possible to determine  $L_a$  indirectly (Gordon and Wang, 1994). Over Case 1 clear-waters, water-leaving radiance is negligible in the NIR bands because of strong NIR absorption by water, thus, the radiance measured is essentially the contributions from the atmosphere. Therefore,  $L_a$  could be estimated after removing  $L_r$  from the TOA radiance at the NIR bands. To estimate  $L_a$  in the visible

wavelengths, one NIR band is required for assessing the magnitude of aerosol's contribution and another is required for assessing its dependence on wavelength. Gordon and Wang (1994) atmospheric correction algorithm uses the SeaWiFS NIR band centered at 865 nm to estimate the aerosol scattering and 765 nm band together with 865 nm band to extrapolate into visible.

The technique described above does not work over Case 2 waters because NIR reflectance is influenced by the optically active constituents in the water. Therefore in this study, Hu et al. (2000) aerosol correction procedure was used for an accurate correction of aerosol scattering. A clear-water pixel close to the atmospheric correction site was identified in the same scene from the open ocean waters where the TOA radiances at the NIR bands were minimal.  $L_a$  at the two NIR bands was determined after removing  $L_r$  from the TOA radiance. From  $L_a$  at the two NIR bands,  $L_a$  for bands less than 700 nm were computed through extrapolation using a spectral model following Gordon and Wang (1994), Gordon et al. (1997), and Mohan and Chauhan (2003). The expression for aerosol path radiance (Doerffer, 1992) is:

$$L_a(\lambda_i) = \frac{F_0'(\lambda_i) \omega_{0a} \tau_a P_a}{4\pi \cos \theta_v} \quad (3.16)$$

where  $\omega_{0a}$  is single scattering albedo (equals to 1),  $\tau_a$  is aerosol optical thickness, and  $P_a$  is aerosol scattering phase function. By assuming an exponential relationship between aerosol optical thickness and wavelength (Gordon and Wang, 1994),  $\tau_a \propto e^{-\lambda}$ , and the phase function to remain constant over the desired wavelengths (Mohan and Chauhan, 2003), Eq. (3.16) can be modified to:

$$L_a(\lambda) / F_0'(\lambda) = k e^{(-c\lambda)} \quad (3.17)$$

where  $k$  and  $c$  are constants. Natural logarithm in both sides of Eq. (3.17) leads to:

$$\ln[L_a(\lambda) / F_0'(\lambda)] = k (-c) \lambda = -\varepsilon \lambda \quad (3.18)$$

$Ln[L_a(\lambda) / F_0'(\lambda)]$  for OCM NIR bands centered at 768.6 and 865.1 nm were plotted against  $\lambda$ , and  $\varepsilon$  was determined as the negative of the slope of the straight line as:

$$\frac{Ln\{L_a(\lambda_{865.1}) / F_0'(\lambda_{865.1})\} - Ln\{L_a(\lambda_{768.6}) / F_0'(\lambda_{768.6})\}}{\lambda_{865.1} - \lambda_{768.6}} = -\varepsilon \quad (3.19)$$

Once  $\varepsilon$  was known, the  $L_a$  for the wavelengths below 700 nm were determined as:

$$L_a(\lambda_i < 700nm) = L_a(\lambda_{865.1})(F_0' / F_0'(\lambda_{865.1}))e^{[-\varepsilon(\lambda_i / \lambda_{865.1})]} \quad (3.20)$$

3.2.2.3 Computation of Diffuse Transmittance ( $t(\lambda_i)$ ): Diffuse transmittance from the water surface to the satellite was computed as (Hu et al., 2004):

$$t(\lambda_i) = e^{\left[-\left(\frac{\tau_r(\lambda_i)}{2}\right)\left(\frac{1}{\cos\theta_v}\right)\right]} \quad (3.21)$$

3.2.2.4 Computation of Water-Leaving Radiance ( $L_w(\lambda_i)$ ): The desirable water-leaving radiance at a specific wavelength was computed by rewriting the Eq. (3.2) as:

$$L_w(\lambda_i) = \frac{L_t^*(\lambda_i) - L_r(\lambda_i) - L_a(\lambda_i)}{t(\lambda_i)} \quad (3.22)$$

3.2.2.5 Computation of Normalized Water-Leaving Radiance ( ${}_nL_w(\lambda_i)$ ): The  ${}_nL_w$  is approximately the radiance that would exit the ocean in the absence of atmosphere with sun at the zenith at mean earth-sun distance (1 AU), and was computed as given by Gordon and Voss (2004):

$${}_nL_w(\lambda_i) = \frac{L_w(\lambda_i)}{d^{-2} \times \cos\theta_0 \times e^{\left\{-\left(\frac{\tau_r(\lambda_i)}{2}\right)\left(\frac{1}{\cos\theta_0}\right)\right\}}} \quad (3.23)$$

where  $d$  is earth-sun distance in astronomical unit (AU).

3.2.2.6 Computation of remote sensing reflectance ( $R_{rs}(\lambda_i)$ ): The  $R_{rs}$  associated with  $nL_w$  was computed as given by Gordon and Voss (2004):

$$R_{rs}(\lambda_i) = \frac{nL_w(\lambda_i)}{F_0(\lambda_i)} \quad (3.24)$$

This atmospheric correction procedure does not include out-of-band correction, whitecap correction, surface roughness influences and contribution of  $L_a$  to diffuse transmittance. However, these corrections will not significantly change the overall accuracy of the procedure particularly for small lakes or estuaries on low wind speed days when whitecap and surface roughness terms are minimal.

### 3.2.3 Vicarious Calibration

In addition to an accurate atmospheric correction, a precise vicarious calibration is crucial to the success of any quantitative ocean color remote sensing data retrieval because of the uncertainties associated with pre-launch calibration coefficients (Franz et al., 2007). Therefore, post-launch vicarious calibration of ocean color sensors in a timely manner is necessary. Any systematic bias associated with the atmospheric correction algorithm further emphasizes the need of continuously monitoring all the bands for any calibration errors. Thus, the vicarious calibration as discussed below is the procedure to determine new coefficients for adjustments of the TOA radiance due to both, post launch changes in sensor response, and any unknown bias due to the atmospheric correction algorithm.

Vicarious calibration is usually achieved by comparing satellite-derived  $nL_w$  and *in situ* measured  $nL_w$ , but it can also be based on models, regional climatology data or retrievals from other sensors (Franz et al., 2007). In the absence of any “ground” truth such as buoy or other suitable matchup data, an inter-comparison of satellite sensors is often the best choice (Suresh et

al., 2006). As SeaWiFS instrument was well-calibrated, the SeaWiFS  $nL_w$  values are the best choice to vicariously calibrate another satellite sensor, particularly when the bands of the sensor to be calibrated (i.e., OCM) are identical to SeaWiFS and the sensor had a similar overpass time as SeaWiFS. The OCM calibration table was last updated in 2003 (S. Kumar, NRSC, India, pers. comm.). Therefore, OCM data processed using the old calibration table produced abnormal  $nL_w$  values during preliminary analysis. Thus, the OCM bands were vicariously calibrated using coincident and co-located SeaWiFS data. SeaWiFS images were processed through SeaDAS 6.0 and  $nL_w$  values at the six sites were extracted and compared with the corresponding OCM  $nL_w$  radiance data produced through the atmospheric correction procedure developed in this study. Out of the eight OCM bands, the two NIR bands were not considered for vicarious calibration due to near-zero NIR water-leaving radiance in clear water areas. Based on the comparison, six calibration coefficients were determined for the six OCM bands and multiplied to OCM TOA radiances, such that the combined root mean square error (RMSE) for all the six dates between OCM and SeaWiFS  $nL_w$  was minimal. Thus, for the vicarious calibration coefficient for the band  $i$ , the RMSE for the  $i$ th band,  $e_i$  was computed as

$$e_i = \sqrt{\frac{\sum_{j=1}^n \{(OCM_{nL_{w_{ij}}}) - (SeaWiFS_{nL_{w_{ij}}})\}^2}{n}} \quad (3.25)$$

where  $i$  represents OCM bands from 1 to 6, and  $j$  represents overpass days from 1 to 6.

The vicarious calibration coefficients are presented in Table 3.2. As these coefficients were computed for various observation dates over the OCM lifespan, they can be termed as OCM mission mean vicarious gains and could be used to produce accurate OCM TOA radiances. Originally, SeaWiFS data are vicariously calibrated by comparing SeaWiFS TOA radiances with

the predicted TOA radiances obtained at the MOBY site so that the average difference between the MOBY and SeaWiFS  $nL_w$  are minimal. The vicarious calibration procedure described here used SeaWiFS  $nL_w$  values as a proxy for *in situ*  $nL_w$  and compared these with  $nL_w$  from co-located pixels of OCM data. An optimization technique was used to correctly predict the TOA radiances from the OCM data using the new atmospheric correction procedure. Therefore, the vicarious calibration coefficients developed in this study adjust for any changes in the response due to the atmospheric correction procedure, in addition to the changes due to instrument bias or any other source of calibration error. Since, this is a simple and straight-forward approach, new calibration coefficients can be computed easily when needed in future.

Table 3.2. Vicarious calibration coefficients of OCM bands 1-6.

Bands	Vicarious calibration coefficients	Error in original TOA radiance
Band 1	1.162430130338560	16.2 %
Band 2	1.099317412022420	9.93 %
Band 3	1.097377164249840	9.73 %
Band 4	1.093961431616450	9.39 %
Band 5	1.085434622452900	8.54 %
Band 6	1.021605349340930	2.16 %

#### 3.2.4 Destriping

After atmospheric correction of vicariously calibrated OCM data, occasional abnormalities were observed in the spectral shapes of the retrieved OCM  $R_{rs}$ , especially in bands 1, 2 and 3. For example, sometimes a peak was observed at OCM band centered at 441.4 nm. If these abnormalities were due to calibration error, this typical low-high-low shape corresponding to OCM bands 1, 2 and 3 should have appeared in the spectra of all the stations on the same day. From comparison with 250 m resolution MODIS-Aqua images, it was observed that MODIS-Aqua bands do not have these periodic features, meaning that the OCM features are artifacts. After analyzing several images carefully, it was concluded that these artifacts in OCM



data were due to striping. Upon registration and geolocation, these along-track stripes result in image speckling. Lyon (2009) developed an Automated Destriping algorithm (ADM) to remove the effects of striping from OCM data. ADM has been integrated into the Automated Processing System (APS) of Naval Research Laboratory, Stennis Space Center, Mississippi, USA. The OCM images over Lac des Allemands were destriped using ADM (by S. Ladner of NRL, Stennis Space Center) before vicarious calibration and atmospheric correction.

*In situ*  $R_{rs}$  values were obtained with a hand-held GER 1500 (Geophysical and Environmental Research) radiometer on selected dates at the 12 sites coinciding with clear-sky OCM data. The hyperspectral radiometer data were weighted with the relative spectral response function of OCM to yield  $R_{rs}$  values at the six OCM bands. Weighted radiometer  $R_{rs}$  and  $R_{rs}$  estimated by the new code before and after destriping were compared to gauge the performance of the combined destriping, vicarious calibration and atmospheric correction approach.

### 3.3. Results and Discussion

The following datasets were compared and analyzed for the six study sites: (a) new code processed OCM data [new code OCM], (b) new code processed SeaWiFS data [new code SeaWiFS], (c) SeaDAS processed SeaWiFS data with multiple scattering approximations [SeaDAS (default) SeaWiFS], (d) SeaDAS processed SeaWiFS data with single scattering approximations [SeaDAS (single scattering) SeaWiFS] and (e) SeaDAS processed OCM data [SeaDAS OCM].

In most instances,  $L_r$  is much greater than all the other atmospheric attenuation components, so it is critical that the computations of  $L_r$  be carried out accurately (Gordon et al., 1988). To assess the accuracy of  $L_r$  estimation, the new code computed  $L_r$  were compared with SeaDAS provided  $L_r$  along OCM and SeaWiFS scan lines (Fig. 3.2 and 3.3). It is well-known

that  $L_r$  values increase from the scene center towards the edges with the increase in satellite zenith angles forming a U-shaped curve, which is particularly noticeable in the blue bands. For the SeaWiFS scene, the new code computed  $L_r$  and SeaDAS provided  $L_r$  were consistent with each other for the most part except for the scan edges of the blue bands (Fig. 3.3). These differences in  $L_r$  at SeaWiFS scan edges were due to the high swath width of SeaWiFS. However for the entire OCM scene, the new code computed  $L_r$  were in good agreement with SeaDAS provided  $L_r$  (Fig. 3.2).

For a range of  $\tau_r$  values, sun angles, and viewing angles of interest,  $L_r$  calculated with the single scattering approximations can differ from the results of scalar radiative transfer models by 3-4 percent, and the  $L_r$  computed by scalar radiative transfer models can differ from vector radiative transfer models (models including polarization by approximately the same amount) by a few percent (Kattawar et al., 1976; Gordon et al., 1988). The procedure developed in this study uses a single scattering approximation for computations of  $L_r$ , but it incorporates corrections for polarization, by considering approximately equal s- and p-polarizations. The SeaDAS atmospheric correction algorithm uses lookup tables for Rayleigh and aerosol radiances, which are generated with over ~25,000 radiative transfer simulations using multiple scattering approximations. SeaDAS does not provide single scattering  $L_r$ , therefore, single scattering comparison of new code processed  $L_r$  and SeaDAS processed  $L_r$  was not possible. However, SeaDAS can provide single scattering  $L_a$ ; therefore, single and multiple aerosol scattering provided by SeaDAS can be compared. It was found that sometimes small differences existed in SeaDAS produced single and multiple aerosol scattering approximations (not shown). It was observed that the new code computed  $L_r$  values were fairly accurate with a difference of less

than 5% from SeaDAS computed  $L_r$ . Thus, it was concluded that, by employing the new code, a reasonable correction for  $L_r$  could be accomplished.

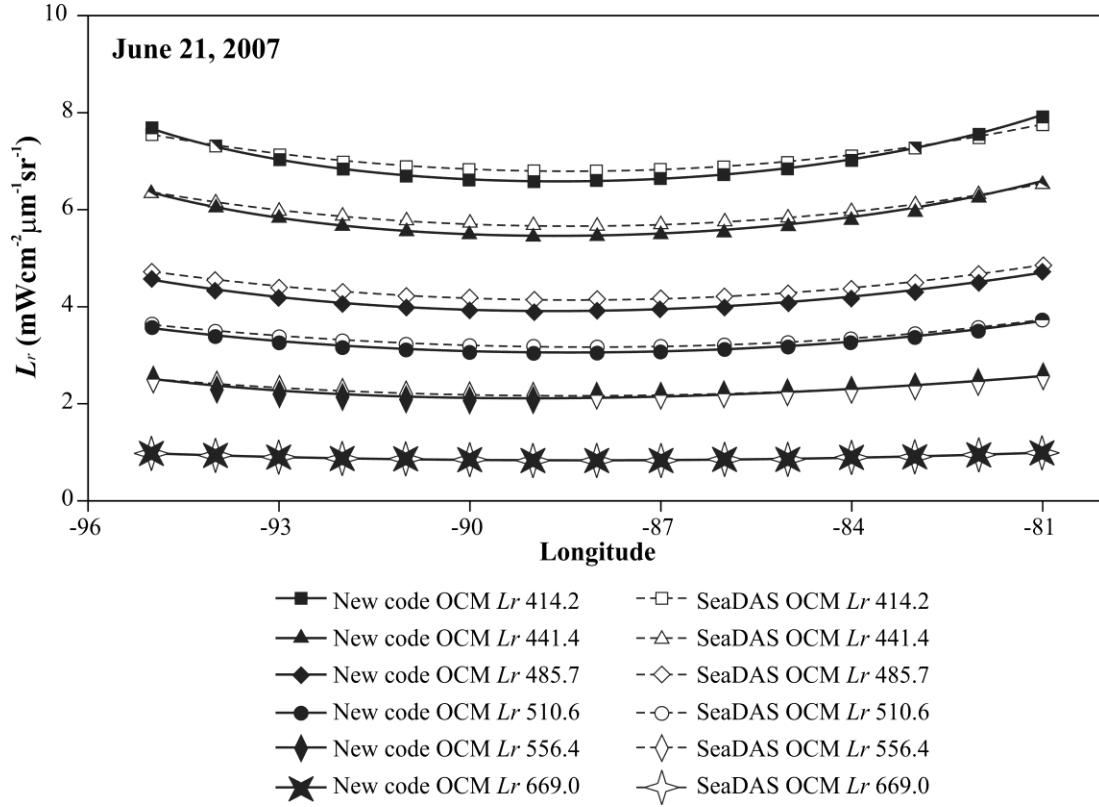


Fig. 3.2. Comparison of Rayleigh path radiance for OCM bands 1-6 calculated by the new code and SeaDAS along a scan line of OCM data of June 21, 2007.

Fig. 3.4 shows the comparison of Rayleigh radiance, aerosol radiance and diffuse transmittance calculated by the new code and SeaDAS over the atmospheric correction sites in the OCM data.  $L_r$  computed by the new code and SeaDAS were in good agreement for the dates November 7, 2004, April 20, 2007 and June 21, 2007. Since Rayleigh scattering depends on solar and viewing geometries and the location of the observation site within the scene, the differences were greater between the new code and SeaDAS computed  $L_r$  on November 5, 2004, December 19, 2004 and November 17, 2006. The new code derived diffuse transmittance

and aerosol radiance values for all the sites and dates were in agreement with the SeaDAS calculations (Fig. 3.4).

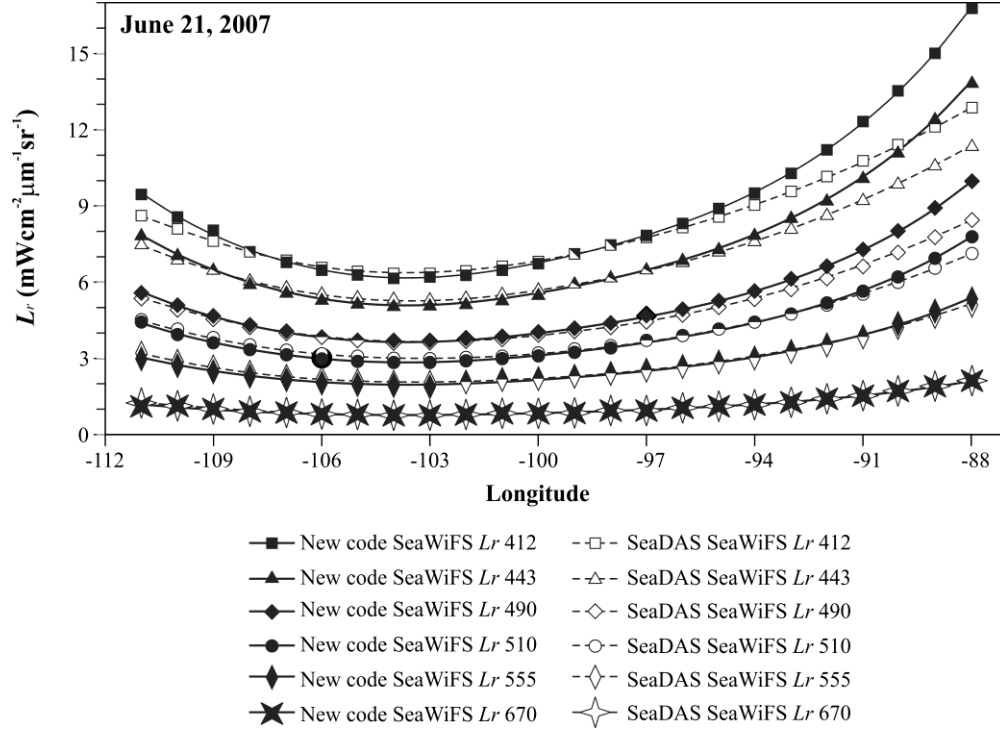


Fig. 3.3. Comparison of Rayleigh path radiance for SeaWiFS bands 1-6 calculated by the new code and SeaDAS along a scan line of SeaWiFS data of June 21, 2007.

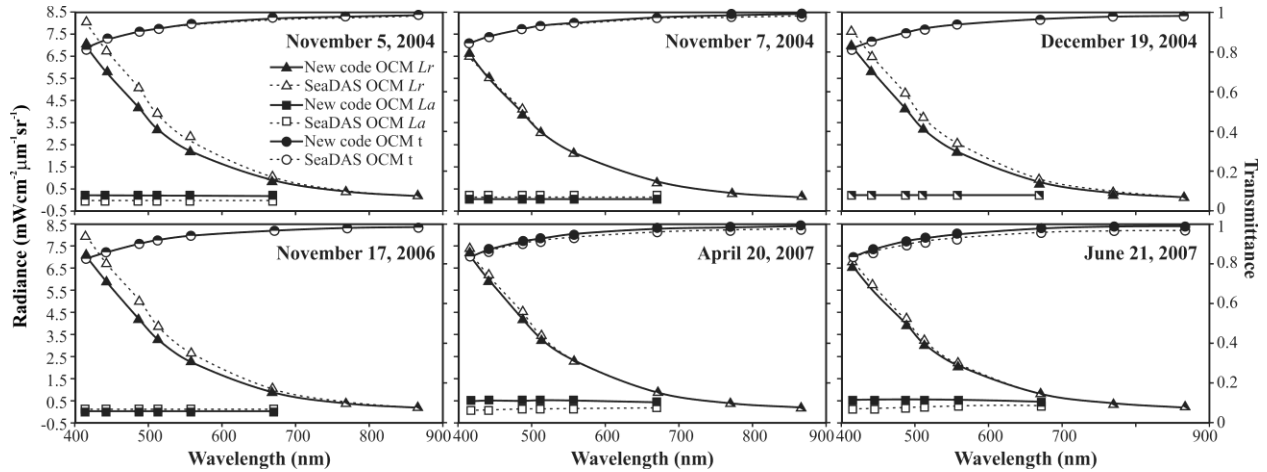


Fig. 3.4. Comparison of Rayleigh path radiance ( $L_r$ ), aerosol path radiance ( $L_a$ ) and Diffuse transmittance (t) calculated by the new code and SeaDAS at the atmospheric correction sites in each of the OCM data.

OCM data of December 19, 2004 had stripes in band 1, but other bands were stripe free. Unfortunately, the atmospheric correction site for December 19, 2004 was on a stripe with bad data, which prevented  $L_a$ ,  $L_w$ ,  $nL_w$ , and  $R_{rs}$  calculations for any band from SeaDAS processing. Therefore, SeaDAS processed  $L_a$  is not shown for December 19, 2004 in Fig. 3.4. Although a destriping algorithm such as the one proposed by Lyon (2009) (used in this study) or Wang and Franz (2000) could be applied to eliminate this type of striping artifact, the atmospheric correction procedure should not transfer the effects of stripes to other bands, as occurs in the SeaDAS processing. However, the new code deals with each band individually. Therefore, the observed striping in band 1 on December 19, 2004 did not negatively impact data retrieval in other bands.

Fig. 3.5 compares the OCM TOA radiances before and after vicarious calibration, and the corresponding  $nL_w$  values computed by the new code and SeaDAS. Before vicarious calibration significant errors were observed especially in the blue bands (Fig. 3.5, Table 3.2). Large calibration errors resulted in low TOA radiances. Since the atmospheric correction terms are computed independently, upon applying these corrections to the lower than anticipated TOA radiance, negative  $nL_w$  values were obtained before vicarious calibration. Note that for December 19, 2004 the SeaDAS processed  $nL_w$  were not available as the site was on a stripe of bad data. Before vicarious calibration the shapes of  $nL_w$  spectra did not resemble expected clear-water spectral shapes. After vicarious calibration, OCM  $nL_w$  values were positive even in the blue bands and resembled clear-water spectral shapes (IOCCG, 2010). New code and SeaDAS processed spectra were in good agreement.

The vicarious calibration procedure presented in this study is similar to the SeaWiFS procedure. SeaWiFS vicarious calibration computes the coefficients by predicting TOA radiance

after matching SeaWiFS  $nL_w$  values with the MOBY  $nL_w$  values. The vicarious calibration procedure developed in this study computes the coefficients by predicting TOA radiance after matching OCM  $nL_w$  values with near synchronous SeaWiFS  $nL_w$  values. This procedure also adjusts the deviations resulting from integrated instrument and atmospheric correction. Therefore, if OCM data are vicariously calibrated using the coefficients given in table 3.2 and processed with the atmospheric correction procedure presented in this study, the resulting  $nL_w$  values will be in agreement with SeaWiFS  $nL_w$  values of the same dates. In addition, this simple procedure can be easily duplicated and these calibration coefficients can be updated for the OCM data of any date irrespective of the calibration status of OCM data. This procedure can also be used to derive vicarious calibration coefficients for other ocean color sensors using SeaWiFS as a standard.

Fig. 3.6 shows the comparisons between the new code and SeaDAS processed SeaWiFS, and vicariously calibrated OCM  $nL_w$  spectra. The spectral shapes of SeaDAS processed SeaWiFS (with the default multi-scattering and the single scattering approaches) were similar with a slight difference in magnitudes. The new code processed SeaWiFS  $nL_w$  values were in good agreements with SeaDAS processed SeaWiFS  $nL_w$  values, however, a difference was observed in the first few bands. This is because the SeaWiFS data were not vicariously calibrated when processed through the new code. In SeaDAS, the SeaWiFS vicarious calibration coefficients of the corresponding dates are usually applied prior to atmospheric correction using look-up-tables within SeaDAS. If the SeaWiFS data are not processed through SeaDAS, the vicarious calibration coefficients are not being applied automatically and differences in radiance values would be observed. From Fig. 3.6, it is clear that the blue SeaWiFS bands were most affected by these calibration errors. Hu et al. (2000) also found significantly lower water-leaving

radiances in SeaWiFS bands 1 and 2 while processing SeaWiFS data through their modified atmospheric correction procedure. They also attributed this to incorrect calibrations in the SeaWiFS bands 1 and 2.

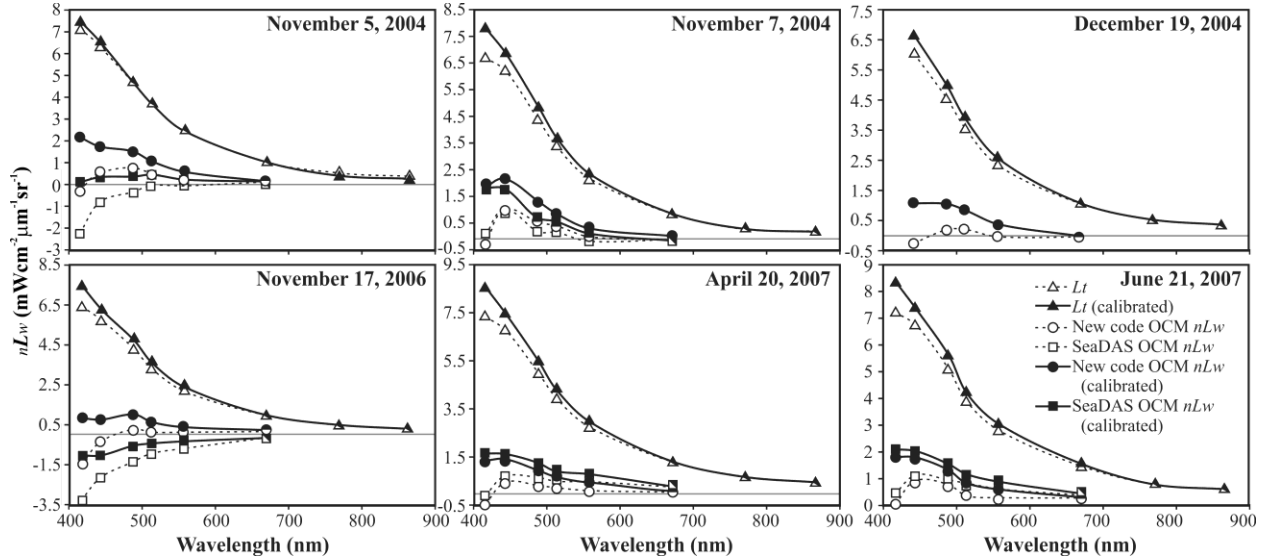


Fig. 3.5. Comparison of OCM TOA radiances before and after vicarious calibration, and the corresponding  $nL_w$  values computed by the new code and SeaDAS. Solid dots with solid lines represent vicariously calibrated  $nL_w$  and TOA radiances, and hollow dots with dotted lines represent  $nL_w$  and TOA radiances before vicarious calibration.

New code processed and SeaDAS processed vicariously calibrated OCM  $nL_w$  spectra were in good agreement with each other for the most part except for November 5, 2004, when a difference in the first three bands was observed, and for November 17, 2006, when the SeaDAS processed spectra were negative for all the bands. The new code processed OCM spectral shapes for these two dates were in good agreement with SeaDAS processed SeaWiFS (both single and multi-scattering) and new code processed SeaWiFS results, but the SeaDAS processed OCM spectra were not in agreement with any other spectral shapes. There was maximum disagreement on these two dates between the SeaDAS processed  $L_r$  and new code processed  $L_r$  (Fig. 3.4). It can be concluded that in this case the new code processed  $L_r$  values are more realistic compared

to SeaDAS processed  $L_r$  because the new code processed  $nL_w$  values were in agreement with SeaWiFS  $nL_w$  (Fig. 3.6). Thus, the new code provided SeaWiFS-like  $nL_w$  values.

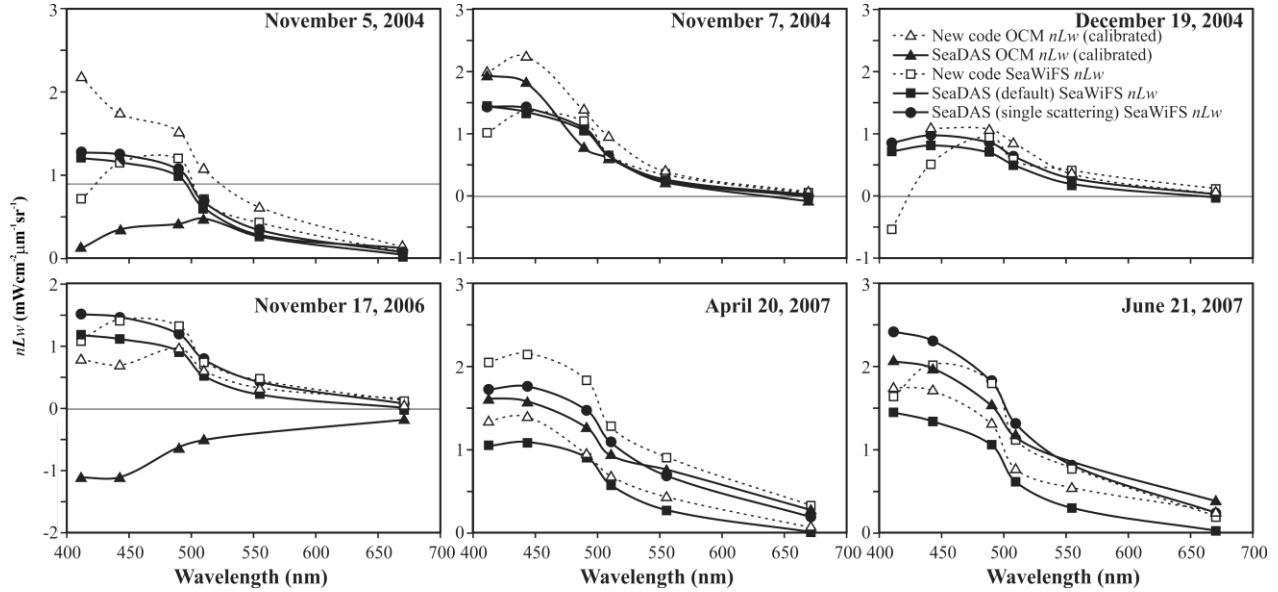


Fig. 3.6. Comparison of new code and SeaDAS computed OCM and SeaWiFS  $nL_w$ .

In summary, it was demonstrated that an accurate atmospheric correction of OCM data is possible using the atmospheric correction procedure developed in this study. Using the calibration coefficients determined from the clear-water locations, realistic  $nL_w$  values were obtained from OCM data. This atmospheric correction procedure was applied to all the clear-sky OCM data covering Lac des Allemands during the study period (from November 2006 to November 2007). Fig. 3.7 shows the TOA radiances from OCM data of April 20, 2007 at four selected sites in the lake before and after vicarious calibration, along with comparisons of the Rayleigh radiances calculated by the new code and SeaDAS. Before the vicarious calibration, negative  $nL_w$  values were computed by both new code and SeaDAS in OCM bands 1 and 2 because the TOA radiances were less than Rayleigh radiances at those bands. As Lac des Allemands is a very small lake, there is not much variation in the viewing and solar angles and



atmospheric pressure, therefore, both the new code and SeaDAS calculated Rayleigh radiances were similar for all the sites. Fortuitously, Lac des Allemands falls on the scene center and the OCM sensor has an exact repeat coverage. Therefore,  $L_r$  computations by new code for all the other dates were as accurate as  $L_r$  shown in Fig. 3.7.

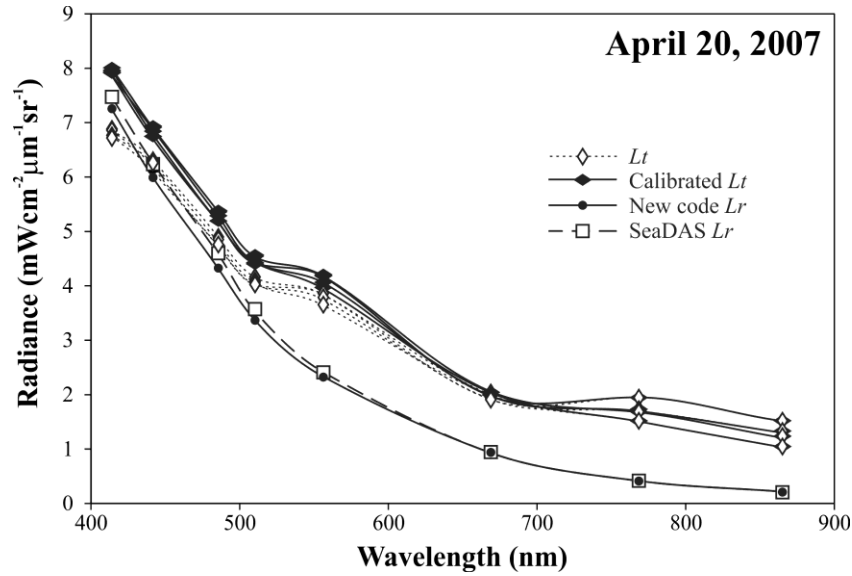


Fig. 3.7. Comparison of TOA radiance before vicarious calibration ( $L_t$ ) and after vicarious calibration (Calibrated  $L_t$ ) at four selected sites (S1, S7, S9 and S12) from the 12 sites in Lac des Allemands for the OCM data of April 20, 2007. Comparison of Rayleigh path radiance ( $L_r$ ) calculated by the new code and SeaDAS at these 4 sites is also shown.

A comparison of aerosol radiances computed by the new code and SeaDAS at the 12 sites is presented in Fig. 3.8. In this study, the  $L_a$  estimation scheme used the Hu et al. (2000) technique, which “borrows” aerosol types of an adjacent clear-water region, to apply over turbid Case 2 waters. Assuming the aerosol characteristics do not change over short distances, the aerosol characteristics were transferred from a clear-water pixel and were applied to all 12 sites in Lac des Allemands. In contrast, SeaDAS uses an iterative approach that assumes a “known” empirical relationship between the  $L_w$  values for at least three bands (usually bands 6, 7, and 8) and Chl  $a$ . However, in a hyper-eutrophic lake such as in Lac des Allemands, the results of the empirical relationships could be erroneous. Therefore, the iterative approach produces errors in

computed  $L_a$ . In such a small lake, a large variation in aerosol radiance as shown by the SeaDAS computed  $L_a$  values at the 12 sites would not be expected (Fig. 3.8). These differences are likely attributable to variations in water constituents rather than variations in aerosol characteristics.

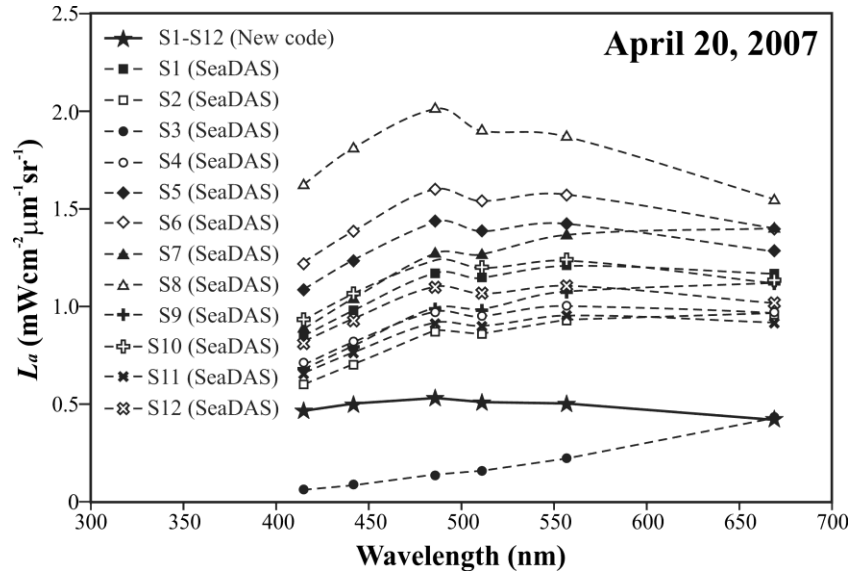


Fig. 3.8. Comparison of aerosol radiance ( $L_a$ ) calculated by the new code and SeaDAS at the 12 sites in Lac des Allemands for the OCM data of April 20, 2007.

Due to variations in relative response of the individual detectors on the CCD array, OCM radiance images sometimes have along-track stripes especially obvious in OCM bands 1, 2, and 3. Fig. 3.9 shows the comparison of  $R_{rs}$  obtained from *in situ* measurements and  $R_{rs}$  estimated by the new code before and after destriping for June 21 and October 11, 2007 at a central lake site. Clearly, destriping improved the  $R_{rs}$  spectra and reduced the abnormalities in the blue bands. The destriped new code  $R_{rs}$  spectra and the *in situ* radiometer spectra demonstrated good agreement. The high closure between the radiometer  $R_{rs}$  and the new code  $R_{rs}$  demonstrated the effectiveness of the procedures developed in this study.

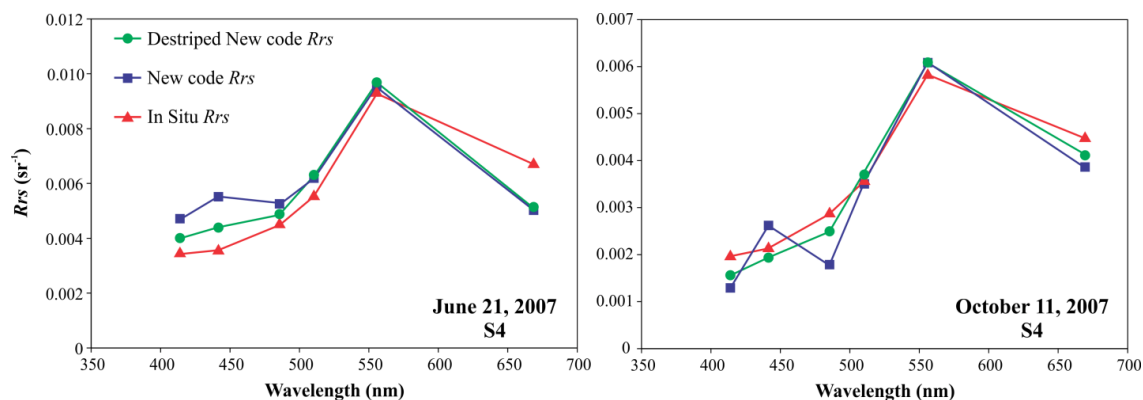


Fig. 3.9. Comparison of *in situ*  $R_{rs}$  and  $R_{rs}$  estimated by the new code before and after destriping. *In situ*  $R_{rs}$  was obtained with a hand-held hyperspectral radiometer and then weighted with the relative spectral response function of each OCM band.

Comparison of  $nL_w$  calculated by SeaDAS and the new code before and after destriping of OCM data at five selected sites in the lake is shown in Fig. 3.10. Since SeaDAS yielded slightly higher  $L_a$ , the SeaDAS processed  $nL_w$  values are negative in the first four bands. For one site, S3, the SeaDAS computed  $nL_w$  values were positive and highest among all the sites. S3 is located in southwest Lac des Allemands, where a bayou introduces copious amounts of suspended sediments and dissolved material from surrounding areas to the lake. On April 20, 2007 the water color at S3 was brown to dark brown as observed visually during the field trip and also in the OCM “true color” image (Dash et al., in press). Measured *in situ* data suggested a CDOM absorption coefficient of  $13.05 \text{ m}^{-1}$  (at 412 nm), a SPM concentration of 12 mg/L and a Chl *a* concentration of  $36.72 \text{ } \mu\text{g/L}$  at that site on April 20, 2007. As SPM was found to be relatively dark detrital matter at S3 and CDOM exhibits high absorption in the blue bands, there should be more absorption especially in the blue and therefore  $nL_w$  should be lower than other sites. Hence, the relatively high  $nL_w$  computed by SeaDAS for the OCM data at S3 seems unrealistic. On the contrary, the new code computed  $nL_w$  values were positive throughout the visible spectrum. For S3, the lowest  $nL_w$  was observed as expected. Overall, the new code computed  $nL_w$  spectra resembled the ideal phytoplankton spectra (IOCCG, 2010). Using this

combined atmospheric correction and vicarious calibration procedure, new algorithms were successfully developed for estimating cyanobacteria by quantifying phycocyanin and Chl *a* in Lac des Allemands from OCM data (Dash et al., in press).

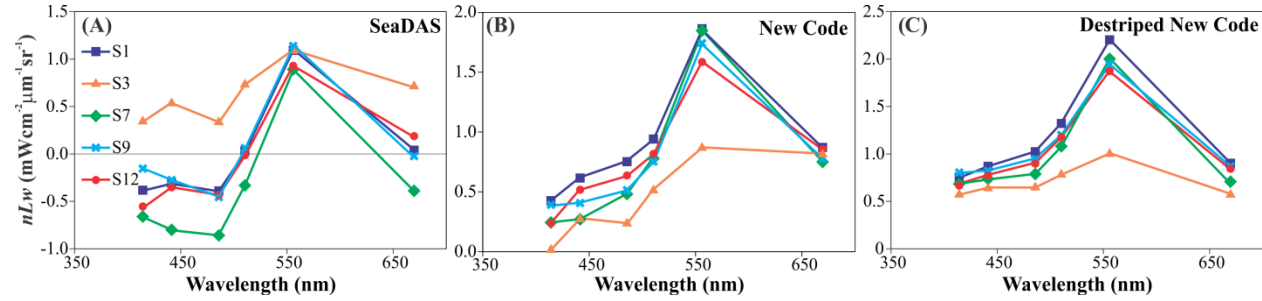


Fig. 3.10. Comparison of normalized water-leaving radiance ( $nL_w$ ) calculated by SeaDAS and by the new code before and after destriping of the OCM data of April 20, 2007 at selected 5 sites (S1, S3, S7, S9 and S12) out of the 12 sites in Lac des Allemands.

Retrieval of accurate  $R_{rs}$  in coastal Case 2 waters provides a challenge for satellite remote sensing. The standard atmospheric correction procedure developed for SeaWiFS yields unacceptable errors, and/or masks the Case 2 water pixels due to atmospheric correction failure. The atmospheric correction procedure presented here reduces errors in the estimated water-leaving radiance and provides more accurate results in small- to moderate-sized coastal water bodies. The accuracy in the estimated water-leaving radiance may sometimes exhibit minor errors due to the use of a single scattering approximation (if the site is located towards the scan edge) or homogeneous aerosol assumption. Nevertheless, the simple atmospheric correction procedure described here can be used to obtain valid retrievals in Case 2 waters and can be easily modified based on user needs. A vicarious calibration procedure was also developed for the recalibration of OCM data. For any sensor having identical bands and a similar overpass time as SeaWiFS, vicarious calibration coefficients can be derived using SeaWiFS  $nL_w$  over clear-water locations by following this procedure. In the absence of *in situ*  $nL_w$  data, this procedure is a cost effective solution for the vicarious calibration of any ocean color sensor.

### 3.4. Conclusions

A detailed methodology for the vicarious calibration and atmospheric correction of Oceansat-1 OCM satellite data over clear waters and an optically complex lake was presented. Over Case 1 clear water locations, the  $nL_w$  values from OCM data computed by the combined atmospheric correction and vicarious calibration procedure developed in this study were very similar to the  $nL_w$  values computed by SeaDAS from SeaWiFS and OCM data. Since the main objective of this study was to atmospherically correct the OCM data of the hyper-eutrophic Lac des Allemands, this atmospheric correction procedure was applied to the destriped and vicariously calibrated OCM data covering the lake. The  $R_{rs}$  obtained after the atmospheric correction of OCM data over the lake were in good agreements with *in situ*  $R_{rs}$ , and the spectral shapes resembled Chl *a* rich Case 2 waters, while SeaDAS and other atmospheric correction procedures produced either negative/erroneous  $nL_w$  values or masked the pixels.

SeaDAS was developed over many years with an emphasis on retrieving Chl *a* in Case 1 waters. Many researchers have tried to use SeaDAS processed data in coastal waters where the atmospheric correction procedure developed for Case 1 waters does not work. This paper presents a straight forward approach for atmospheric correction which can be used by researchers to retrieve better results in coastal waters. With this approach, the retrieved results from OCM and SeaWiFS could be meaningfully compared and a possible merger of datasets could be envisaged. The atmospheric correction and vicarious calibration approach discussed here is also applicable to other ocean color sensors. Future research should include an *in situ* validation experiment over several regions having different aerosol characteristics to further assess the validity of the atmospheric correction procedure presented here.

## CHAPTER 4

### ESTIMATION OF CYANOBACTERIAL PIGMENTS IN A FRESHWATER LAKE USING OCM SATELLITE DATA

#### 4.1. Introduction

A number of studies (Dekker, 1993; Schalles and Yacobi, 2000; Simis et al., 2005; Hunter et al., 2008; Mishra et al., 2009) have utilized the phycocyanin (PC) absorption feature near 620 nm to develop algorithms for quantifying cyanobacteria. More recently Hu et al. (2010) and Wynne et al. (2010) focused on the red and near infrared wavelengths to characterize the distribution and intensity of cyanobacterial blooms using remotely sensed data. However, relatively little attention has been devoted to the reflectance and absorption features in the 500-600 nm region. A spectral curve representing PC absorbance shows that PC has an absorption maximum at 620 nm with a prominent shoulder extending to lower wavelengths (MacColl and Guard-Friar, 1987; Fig. 1.3). The same peak and a prominent shoulder toward blue wavelengths were observed from the measurements of PC absorption coefficients using PC standards in this study (Fig. 1.3). A few studies concerning the mapping of cyanobacteria using satellite measurements have used sensors such as LANDSAT, MERIS, and MODIS (Simis et al., 2005; Wynne et al., 2010; Hu et al., 2010; Vincent et al., 2004). Additionally, while both SeaWiFS and OCM have been used for detecting the cyanobacteria *Trichodesmium* spp. (Subramaniam et al., 2001; Sarangi et al., 2005), and SeaWiFS has been used together with CZCS and MODIS for quantifying the cyanobacteria *Nodularia spumigena* (Kahru et al., 2007), neither OCM nor SeaWiFS has been used for mapping PC concentrations, mainly because these sensors do not have the spectral band covering the PC absorption maximum. In this study, we present the first OCM-based algorithms for quantifying PC using the remote sensing reflectance ( $R_{rs}$ ) at bands <600 nm. Our approach incorporates modeling and subtracting the contributions of other

optically active constituents (OACs) in this wavelength region. This chapter has been published in the journal Remote Sensing of Environment, but some additions were made later.

The Oceansat-1 satellite launched on May 26, 1999 carried the OCM sensor with spectral bands nearly identical to the SeaWiFS sensor. SeaWiFS and MODIS (ocean bands) have high radiometric sensitivity (O'Reilly et al., 1998); however, they lack the spatial resolution needed for studying smaller water bodies. Other ocean color sensors that have the required spatial resolution for studying smaller water bodies, lack frequent revisit cycles. The Oceansat-1 OCM sensor provides a compromise between the two types of sensors discussed above with a spatial resolution of  $360 \times 236$  m and an orbit that repeats exactly every alternate day. OCM acquired data for a period of eleven years since 1999, but these data have not been used much by the scientific community possibly due to one or more of the following: a lack of reliable atmospheric correction procedure and bio-optical algorithms for the sensor, the timing of its launch immediately following the launch of the long-awaited SeaWiFS instrument, and difficulty in data access by the scientific community (Crowley, 2003). Nevertheless, the high resolution OCM data has a strong potential for ocean color research especially in coastal waters. In addition, its successor, the OCM-2 sensor, was launched on September 23, 2009 and OCM-3 is planned for launch in 2013 (ISRO, 2010). The feasibility of quantifying cyanobacteria using OCM bands 4 and 5 centered at 510.6 and 556.4 nm, respectively was examined in the present study. This study is significant because it represents the first attempt of utilizing OCM data to quantify PC and the first effort of using satellite data for both development and validation of algorithms for quantitatively mapping cyanobacteria with  $R_{rs} < 600$  nm. The three primary questions addressed in this study are: 1) Can concentrations and spatial distributions of cyanobacteria be quantified using OCM reflectance measurements? 2) Are wavelengths less than 620 nm applicable for

quantifying PC? 3) Does subtraction of the effects of other optically active constituents improve the performance of the algorithms?

## **4.2. Materials and Methods**

### **4.2.1 Study Site**

Lac des Allemands is a tidally influenced freshwater lake (salinity <1 psu) with a surface area of 49 km<sup>2</sup> located in the uppermost part of the Barataria Estuary in southeastern Louisiana, USA (29°55'25.74'' N, 90°34'39.31'' W; Fig. 1.1). Lac des Allemands provides an ideal natural laboratory for this study because high concentrations of cyanobacteria usually occur in spring and summer (Ren et al., 2009; Garcia et al., 2010; Dortch et al., unpublished data; Swenson et al., unpublished data; Rabalais et al., unpublished data). The average depth of Lac des Allemands is 2 m and it is connected to Lake Salvador and Lake Boeuf through two narrow bayous called Bayou des Allemands and Bayou Boeuf, respectively (Fig. 1.1). Lac des Allemands receives runoff from surrounding areas through Vacherie canal and Bayous Fortier, Bechnel, Lassene and Chevreuil (Fig. 1.1). Bayou Lassene and Bayou Boeuf drain extensively fertilized sugar cane fields to Lac des Allemands and Bayou Chevreuil introduces copious amounts of suspended sediments and dissolved material from surrounding areas. The excess nutrients contribute to the hyper-eutrophic status of Lac des Allemands (Ren et al., 2009; Garcia et al., 2010).

### **4.2.2 Field Data**

In the years 2006-2007, monthly field trips from November 2006 to February 2007, weekly trips from March to August 2007, and bi-weekly trips from September to November 2007 were undertaken. These trips were planned targeting clear-sky conditions over the study area. During each trip, twelve sites in Lac des Allemands were sampled within an hour before and after the Oceansat-1 satellite overpass (12:00 noon  $\pm$ 10 min), approximately (Fig. 1.1). The



field data included collection of water samples in clean Nalgene bottles, *in situ* water quality data using a YSI (Yellow Springs Instrument) 6600 probe and *in situ*  $R_{rs}$  measurements using a GER (Geophysical and Environmental Research) 1500 radiometer. The water samples were collected for High Performance Liquid Chromatography (HPLC) photopigments, the cyanobacteria unique pigment PC, Colored Dissolved Organic Matter (CDOM), Suspended Particulate Matter (SPM), toxin, and microscopic analyses. In the summer of 2009, six field trips were undertaken to obtain another dataset for validation of the algorithms. An overview of the field data collected and laboratory analyses performed during 2006-2007 and 2009 is summarized in Table 2.2 and Table 2.3, respectively.

HPLC analysis of filtered water samples provided concentrations of 40 algal pigments including chlorophyll *a* (Chl *a*) and the cyanobacteria specific pigments echinenone, myxoxanthophyll and zeaxanthin. ChemTax was used to calculate the absolute abundances of major algal groups in Lac des Allemands from the HPLC pigment data (Mackey et al. 1996). For ChemTax, an iterative scheme (Latasa, 2007) was followed using the initial pigment ratios from published ratios (Pinckney et al., 2009; Schlüter et al. 2006). Iterations were successively performed until the ratios in the output matrix remained constant (8 iterations). The ChemTax analysis was limited to cyanobacteria, euglenophyte, chlorophyte, dinoflagellate, cryptophyte, diatom and chrysophyte groups. PC was extracted from the filtered water samples of selected dates according to Downes and Hall (1998) with Tris-buffer and measured the concentration fluorometrically using a Horiba Jovin Yvon fluorometer. To determine the specific absorption coefficients of PC, first a dilution series of concentrations 1 to 100  $\mu\text{g/L}$  with 10  $\mu\text{g/L}$  interval was prepared from the PC standards (Prozyme Inc.) and the absorption coefficients were measured using a Perkin Elmer Lambda 850 spectrophotometer. Subsequently, these absorption

coefficients were divided by PC concentrations to determine the specific absorption coefficient of PC for each dilution. The average specific absorption coefficient of PC, which is presented in Fig. 1.3, was determined by taking the average specific absorption coefficients of PC of all the concentrations.

*In situ*  $R_{rs}$  from 299 nm to 1096 nm was determined from above-water measurements on selected field trips. Measurements of radiance from the water surface, sky radiance, and from a plaque with known spectral directional reflectance (10% Spectralon, Labsphere) were made using a fiber-optic-based high-spectral-resolution GER 1500 radiometer and the data were processed following Hu (2003) for the determination of above-water  $R_{rs}$ . Spectral absorption coefficients of CDOM was determined by filtering the water samples through 0.2  $\mu$ m Nuclepore membrane filters followed by absorption measurements using a multiple path-length aqueous capillary waveguide-based spectrophotometer (D'Sa et al., 1999). The concentrations of SPM were determined by following the glass fiber filter method (USGS, 1987). Recorded volume of water samples were filtered through GF/F filters and the increase in weight of the filter after drying at 105 °C was measured as SPM. Ashing the residue at 500 °C provided the inorganic sediment fraction or suspended particulate inorganic matter (SPIM). Subsequently, the organic fraction or the suspended particulate organic matter (SPOM) was determined by subtracting SPIM from SPM. Water samples collected during this field campaign were used by Garcia et al. (2010) for enumeration of all the species of cyanobacteria present by microscopic cell counts and using an imaging microscope (Fluid Imaging Technologies). Garcia et al. (2010) also reported the microcystin concentrations both in surface water samples and in blue crab tissues, and the environmental data collected using the YSI 6600 instrument for the eight month period from December, 2006 to July, 2007.

The same set of field measurements were obtained on the six field trips in 2009. In addition, filtered water samples were processed on the Perkin Elmer Lambda 850 spectrophotometer to determine the absorption coefficients of total particulate and NAP using quantitative filter pad technique (QFT), following the methods described in Cleveland and Weidemann (1993) and Mitchell et al. (2002). The phytoplankton absorption coefficients were computed by subtracting the absorption coefficients of NAP from the absorption coefficients of total particulate matter. The specific absorption coefficients of phytoplankton were computed by dividing these phytoplankton absorption coefficients by Chl *a* concentrations obtained from the HPLC analysis and then computing the average. For the specific absorption coefficients of NAP, first NAP concentrations were determined by subtracting Chl *a* concentrations from gravimetrically determined SPM after conversion of Chl *a* concentrations from  $\mu\text{g/L}$  to  $\text{mg/L}$ . Subsequently, the specific absorption coefficients of NAP were computed by dividing NAP absorption coefficients by NAP concentrations and averaging all the NAP specific absorption coefficients.

#### 4.2.3 Satellite Data

Clear-sky OCM data were obtained on nine of the field dates in 2006-2007 and on four of the field dates in 2009 (shown with ‘\*’ in Tables 2.2 and 2.3). The OCM data were received via an X-band antenna and processed at the Earth Scan Laboratory, Louisiana State University. Raw OCM data were calibrated by converting raw counts to radiance at the eight OCM spectral bands using the SeaSpace Terascan™ software. Preliminary results showed that the existing data processing software including SeaSpace Terascan™, ENVI FLAASH, and SeaDAS failed in atmospherically correcting OCM data over Lac des Allemands. Additionally, several issues such as image speckling, striping, image registration and calibration errors were observed. Therefore,

a number of steps were followed for the processing of OCM data beginning with a destriping procedure (Lyon, 2009) which corrected for image speckling, striping and image registration issues. Next, a vicarious calibration procedure was developed using SeaWiFS normalized water-leaving radiance ( $nL_w$ ) as a proxy for *in situ*  $nL_w$  (Dash et al., in review). Finally, an atmospheric correction procedure was developed following the SeaWiFS protocol (Dash et al., in review).

#### 4.2.4 Destriping

Due to variations in relative response of the individual detectors on the CCD array, OCM radiance images sometimes have along-track stripes especially obvious in OCM bands 1, 2 and 3. Upon registration and geolocation these along-track stripes result in image speckling. Lyon (2009) developed an automated destriping algorithm (ADM) for OCM data to remove the effects of striping which is based on the information contained in each image. ADM has been integrated into the Automated Processing System (APS) of the Naval Research Laboratory, Stennis Space Center, MS. All the clear-sky OCM data used in this study were processed through the ADM before atmospheric correction.

#### 4.2.5 Vicarious Calibration

OCM data processed using its old calibration table produced abnormal values during preliminary analysis because the OCM calibration table was last updated in 2003 (S. Kumar, National Remote Sensing Centre, India, pers. comm.). Therefore, the OCM bands were vicariously calibrated using coincident and co-located SeaWiFS data at clear-water sites after performing atmospheric correction. The SeaWiFS images were processed through SeaDAS 6.0 and  $nL_w$  values at selected clear-water sites were extracted and compared with the corresponding OCM  $nL_w$  radiance data produced through the atmospheric correction procedure developed in this study. Out of the eight OCM bands, the two NIR bands were not considered for vicarious

calibration due to negligible NIR water-leaving radiance in clear water areas. Based on the comparison, six calibration coefficients for OCM bands 1-6 were determined using optimization technique and multiplied to corresponding OCM TOA radiance such that the combined root mean square error (RMSE) between OCM and SeaWiFS  $nL_w$  was minimal. For the vicarious calibration coefficient for the band  $i$ , the RMSE for the  $i$ th band,  $e_i$  was computed as follows (Dash et al., in review):

$$e_i = \sqrt{\frac{\sum_{j=1}^n \{(OCM_{-nL_{wij}}) - (SeaWiFS_{-nL_{wij}})\}^2}{n}} \quad (4.1)$$

where  $i$  represents bands from 1 to 6 and  $j$  represents overpass days. The vicarious calibration procedure discussed above determined new coefficients for adjustments of TOA radiance due to both post-launch changes in sensor response, and deviations due to any unknown bias of the atmospheric correction algorithm.

#### 4.2.6 Atmospheric Correction

Based on the principles and methods of atmospheric correction for satellite ocean color instruments outlined in Gordon (1997), Mishra et al. (2005), and Hu et al. (2004), an atmospheric correction procedure for OCM was customized (Dash et al., in review). First, effects of ozone absorption were removed from the top of the atmosphere (TOA) radiance (Hu et al., 2004):

$$L_t^*(\lambda_i) = L_t(\lambda_i) \exp \left[ \tau_{oz}(\lambda_i) \left( \frac{1}{\cos \theta_0} + \frac{1}{\cos \theta_v} \right) \right] \quad (4.2)$$

where  $L_t^*(\lambda_i)$  represents TOA radiance measured by the satellite in the absence of ozone,  $\theta_v$  is satellite viewing zenith angle,  $\theta_0$  is solar zenith angle, and  $\tau_{oz}(\lambda)$  is ozone optical depth, which is obtained as (Gordon et al., 1995):

$$\tau_{oz}(\lambda_i) = k_{oz}(\lambda_i) \frac{DU}{1000} \quad (4.3)$$

where  $k_{oz}(\lambda_i)$  is ozone absorption coefficient taken from Gregg and Carder (1990) and  $DU$  is ozone concentration in Dobson Unit obtained from the TOMS (Total Ozone Mapping Spectrometer) website. Rayleigh path radiance ( $L_r$ ) with corrections for Fresnel reflection was computed by modifying the single scattering approximations of Mishra et al. (2005) and Hu et al. (2004), which are based on Gordon (1995). Correction for aerosol path radiance ( $L_a$ ) followed the work of Gordon and Wang (1994), Hu et al. (2000), and Mohan and Chauhan (2003). Clear-water pixels were identified in the same scene from the open ocean waters where the TOA radiances at the NIR bands were minimal.  $L_a$  at the two NIR bands was determined after removing  $L_r$  from the TOA radiance at the clear-water pixels. From  $L_a$  at these two wavelengths,  $L_a$  for bands less than 700 nm was computed through extrapolation using a spectral model (Gordon and Wang, 1994; Gordon et al., 1997; Mohan and Chauhan, 2003). Diffuse transmittance ( $t$ ) was calculated following Hu et al. (2004). After computing  $L_r$ ,  $L_a$  and  $t$  the water-leaving radiance was computed by:

$$L_w(\lambda_i) = \frac{L_t^*(\lambda_i) - L_r(\lambda_i) - L_a(\lambda_i)}{t(\lambda_i)} \quad (4.4)$$

Finally,  $nL_w$  and  $R_{rs}$  were computed by (Gordon and Voss, 2004):

$$nL_w(\lambda_i) = \frac{L_w(\lambda_i)}{d^{-2} \times \cos \theta_0 \times \exp \left\{ - \left( \frac{\tau_r(\lambda)}{2} \right) \left( \frac{1}{\cos \theta_0} \right) \right\}} \quad (4.5)$$

where  $d$  is earth-sun distance in Astronomical Unit (AU), and

$$R_{rs}(\lambda_i) = \frac{nL_w(\lambda_i)}{F_0(\lambda_i)} \quad (4.6)$$

where  $F_0(\lambda_i)$  is the mean extraterrestrial solar irradiance. This atmospheric correction procedure was applied to all the clear-sky OCM data to obtain the spectral  $R_{rs}$  (Dash et al., in review).

#### 4.2.7 Algorithm Development

From the PC absorption features observed in Fig. 1.3, OCM  $R_{rs}$  at bands 5 (556.4 nm) and 4 (510.6 nm) were chosen for quantifying PC. It was chosen not to employ preconceived notions concerning the relationships of single bands, spectral ratio or spectral slopes of OCM  $R_{rs}$  with PC, PC/Chl  $a$  or PC+Chl  $a$  for quantifying PC. Rather all of them were separately used and found that the best relationship was between the spectral slopes of OCM  $R_{rs}$  of bands 5 and 4 with PC. The spectral slope for PC algorithm was defined as

$$Slope[R_{rs}(556.4) : R_{rs}(510.6)] = \frac{R_{rs}(556.4) - R_{rs}(510.6)}{556.4 - 510.6} \quad (4.7)$$

In the 500-600 nm wavelength region, Chl  $a$ , NAP, CDOM and water can have a notable impact on the optical signals of PC in optically complex Case 2 waters such as Lac des Allemands. Therefore,  $R_{rs}$  was computed and subtracted systematically for the combination of components accounting for absorption by water, Chl  $a$ , NAP, and CDOM and backscattering by water, Chl  $a$ , and total particulate matter following the equation (Mobley, 1994; D'Sa et al., 2006)

$$R_{rs}(\lambda) = 0.54 (f/Q) (b_b/(a+b_b)) \quad (4.8)$$

where 0.54 accounts for the fresnel reflectivities at the sea surface.  $f/Q$  values for OCM bands 1-6 were adopted from SeaWiFS wavebands determined from field observations in northern Gulf of Mexico at sites in close proximity to Lac des Allemands (D'Sa et al., 2006). Backscattering coefficient ( $b_b$ ) was taken as  $b_{bw}$  or  $b_{bw} + b_{bChl\ a}$  or  $b_{bw} + b_{bp}$  sequentially, where  $b_{bw}$ ,  $b_{bChl\ a}$ , and  $b_{bp}$  denote backscattering coefficients of water, Chl  $a$ , and particulate matter, respectively. Similarly,

absorption coefficient ( $a$ ) was taken as  $a_w + a_{Chl\ a}$  or  $a_w + a_{Chl\ a} + a_{NAP}$  or  $a_w + a_{Chl\ a} + a_{NAP} + a_{CDOM}$  sequentially, where  $a_w$ ,  $a_{Chl\ a}$ ,  $a_{NAP}$ , and  $a_{CDOM}$  denote absorption coefficient of water, Chl  $a$ , NAP and CDOM, respectively.

For the 400-700 nm region,  $a_w(\lambda)$  were taken from Pope and Fry (1997) and  $b_{bw}(\lambda)$  were taken from Smith and Baker (1981) by multiplying the given scattering coefficients by 0.5.  $a_{Chl\ a}(\lambda)$  and  $a_{NAP}(\lambda)$  were computed by multiplying the concentrations of Chl  $a$  and NAP, respectively with the corresponding specific absorption coefficients.  $a_{CDOM}(\lambda)$  as a function of wavelength, are commonly modeled with an exponentially decreasing function (Bricaud et al., 1981) as:

$$a_{CDOM}(\lambda) = a_{CDOM}(\lambda_0) e^{-S(\lambda-\lambda_0)} \quad (4.9)$$

where  $\lambda_0$  is a reference wavelength, 440 nm, and  $S$  is the spectral slope parameter.  $S$  was calculated as the slope of the logarithm of the  $a_{CDOM}(\lambda)$  values between 400 and 560 nm. For Lac des Allemands,  $S$  varied between 0.012 and 0.022, which is in accordance with the  $S$  values obtained by Singh et al. (2010a, 2010b) in the Barataria Estuary.  $a_{CDOM}$  values for all the wavelengths were extrapolated from  $a_{CDOM}(440)$  using the above computed  $S$  values.

$b_{bChl\ a}(\lambda)$  were computed from Chl  $a$  concentrations using (Gordon et al., 1988; Morel and Maritorena, 2001)

$$b_{bChl\ a}(\lambda) = B \times \{0.416 \times (Chl\ a)^{0.766} \times \frac{550}{\lambda}\} \quad (4.10)$$

where  $B$  (backscattering ratio) is equal to 0.0183 taken from Petzold (1972).  $b_{bp}$  was computed using (Reynolds et al., 2001):

$$b_{bp}(\lambda) = b_{bp}(555) \times (555/\lambda)^7 \quad (4.11)$$

where  $b_{bp}(555)$  was calculated from SPM concentrations using (D'Sa et al., 2007):



$$b_{bp}(555) = \frac{(SPM-0.61)}{106.93} \quad (4.12)$$

and  $\gamma$  is the spectral slope, which indicates the wavelength dependence of  $b_{bp}$  and was computed using (D'Sa et al., 2007):

$$\gamma = -0.566 - [1.395 \times \log \{b_{bp}(555)\}] \quad (4.13)$$

The relationships shown in Eq. (4.12) and (4.13) were obtained from measurements in northern Gulf of Mexico in close proximity to Lac des Allemands (D'Sa et al., 2007).

Having computed the absorption and backscattering coefficients of all the parameters,  $R_{rs}(\lambda)$  were computed for the wavelength region 400-700 nm using Eq. (4.8). These  $R_{rs}$  values were then weighted and averaged with the relative spectral response function of each OCM band to obtain  $R_{rs}$  values at OCM bands 1-6. The weighted and averaged  $R_{rs}$  were subtracted successively from corresponding OCM  $R_{rs}$  to reduce the interference of other OACs on the PC signal. The spectral slopes of OCM bands 4 and 5 were computed from the subtracted  $R_{rs}$  and then regressed against PC for algorithm calibration. The 2006-2007 dataset was utilized for algorithm calibration and the 2009 dataset was utilized for validation.

Algorithms for Chl  $a$  were developed using the spectral slopes of OCM bands 5 (556.4 nm) and 6 (669 nm) as the OCM band 6 is located close to the Chl  $a$  absorption maximum. The spectral slope for Chl  $a$  algorithm was defined as

$$Slope[R_{rs}(556.4) : R_{rs}(669)] = \frac{R_{rs}(556.4) - R_{rs}(669)}{|556.4 - 669|} \quad (4.14)$$

Separation of the effects of other OACs from Chl  $a$  signal was accomplished in a similar fashion by replacing  $a_{Chl\ a}(\lambda)$  with absorption coefficients of PC,  $a_{PC}(\lambda)$  in Eq. (4.8). Values for  $a_{PC}(\lambda)$  were computed by multiplying the concentrations of PC at all the sites with the specific absorption coefficients of PC. Finally, the developed PC and Chl  $a$  algorithms were applied to

OCM data over Lac des Allemands to obtain the concentrations and spatial distributions of cyanobacteria and the phytoplankton assemblage.

#### 4.2.8 Algorithm Validation

All the algorithms were applied to the 2009 validation dataset to investigate the applicability of the new algorithms and accuracy was evaluated using root mean square error (RMSE) and mean absolute error (MAE). In order to remove the effect of magnitude of observations, RMSE and MAE were normalized using the range of observations and expressed in percent form. Expressions for relative RMSE and relative MAE are given as

$$\text{Relative RMSE (\%)} = \frac{\text{RMSE}}{\text{Measured maximum} - \text{Measured minimum}} \times 100 \quad (4.15)$$

$$\text{Relative MAE (\%)} = \frac{1}{n} \frac{\sum_{i=1}^n |\text{Estimated} - \text{Measured}|}{(\text{Measured maximum} - \text{Measured minimum})} \times 100 \quad (4.16)$$

where n represents number of observations.

### 4.3. Results

#### 4.3.1 Phytoplankton Pigments

Pigment data demonstrated large seasonal variations in Chl *a* concentrations and in the pigments associated with cyanobacteria (PC, echinenone and zeaxanthin) in Lac des Allemands (Fig. 4.1 and 4.2). During the 2006-2007 study period, Chl *a*, echinenone and zeaxanthin concentrations ranged from 0.88 to 208.16 µg/L, 0.00 to 103.35 µg/L, and 0.06 to 14.63 µg/L, respectively. Chl *a* concentrations indicated that algal blooms formed in fall 2006, died out during the winter, and reformed as temperatures warmed in spring 2007 (Fig. 4.1A). The largest bloom formed in April 26, 2007 with Chl *a* concentration of 208.16 µg/L and there were numerous smaller blooms in summer and fall 2007. Microscopic analysis revealed that the

largest bloom in April 2007 was a bloom of *Anabaena* spp. The cyanobacteria specific pigments PC and echinenone followed the general Chl *a* trend. The cyanobacteria specific pigment zeaxanthin also followed the general Chl *a* trend, except it was not present in high concentrations during the largest bloom. It was because zeaxanthin is not present in *Anabaena* spp. in high concentrations. During the six field trips in the months of May and June, 2009, Chl *a*, echinenone and zeaxanthin concentrations ranged from 9.46 to 212.76 µg/L, 0.00 to 41.95 µg/L, and 0.67 to 7.74 µg/L, respectively. The 2009 Chl *a* concentrations showed an increase from May 1 to June 18, 2009 with a highest Chl *a* concentration of 212.76 µg/L on June 18, 2009 and a slightly declined level on June 30, 2009 (Fig. 4.2A). During this study period, a small bloom on May 13, 2009 and a relatively larger bloom from June 18, 2009 through June 30, 2009 were observed. PC concentrations ranged from 0.69 to 290.51 µg/L from March 29, 2007 to October 2007 and 2.75 to 363.50 µg/L for the six field trip dates during summer of 2009. The concentrations of PC in 2007 co-varied with Chl *a* (Fig. 4.1B). However, on the six dates in summer 2009, PC concentrations did not co-vary with corresponding Chl *a* concentrations (Fig. 4.2B). Phytoplankton abundances derived from ChemTax showed that cyanobacteria achieved highest abundance among all the algal groups at all the twelve sites on every field trip (Fig. 4.3). According to ChemTax results, during summer 2009, other algal groups including diatoms, chlorophytes, and cryptophytes exhibited higher abundances than their usual low concentrations. These algal groups contributed to the Chl *a*, but not to the PC concentrations, resulting in PC to not co-vary with Chl *a* during summer 2009 in Fig. 4.1B, but they were much less prevalent than cyanobacteria. The ChemTax results also clearly show the large cyanobacterial blooms of April 2007 and June, 2009.

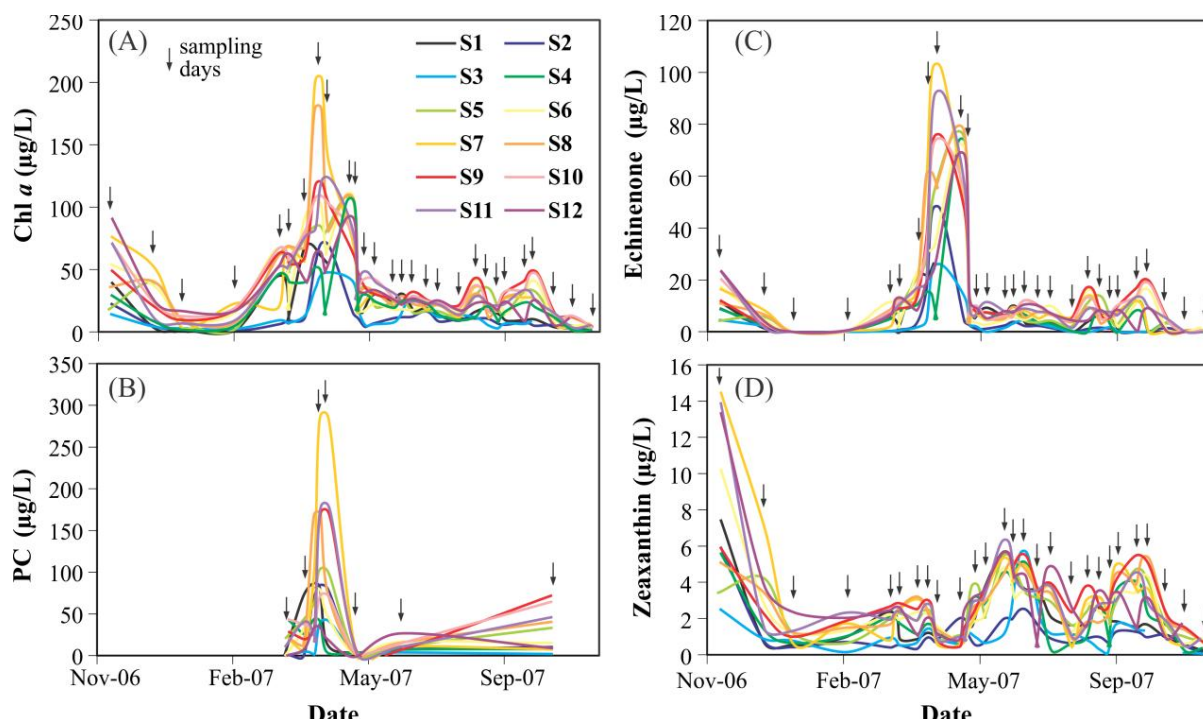


Fig. 4.1. (A) Chl *a*, (B) PC, (C) echinenone and (D) zeaxanthin concentrations at the twelve sampling sites (S1-S12) from November 17, 2006 through November 8, 2007 with sampling days indicated (see Table 2.2 for the list of sampling days).

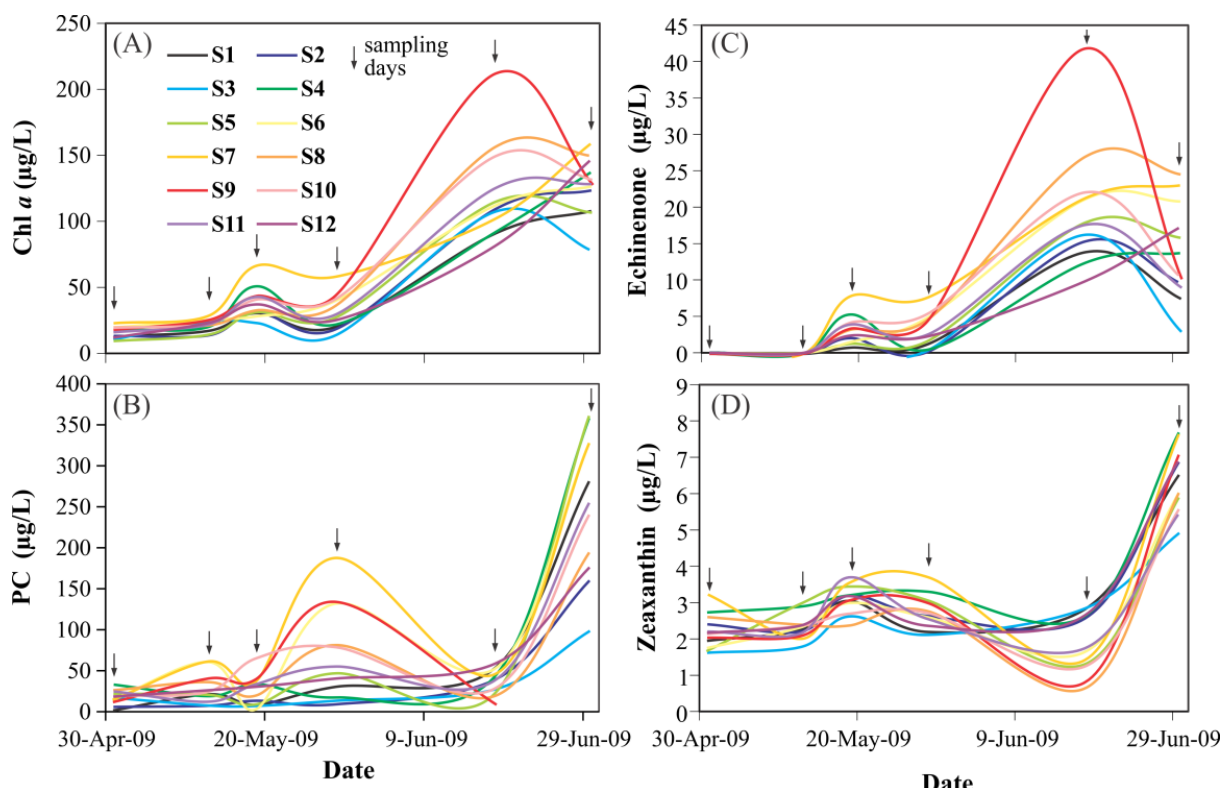


Fig. 4.2. (A) Chl *a*, (B) PC, (C) echinenone and (D) zeaxanthin concentrations at the twelve sampling sites (S1-S12) from May 1, 2009 through June 30, 2009 with sampling days indicated (see Table 2.3 for the list of sampling days).

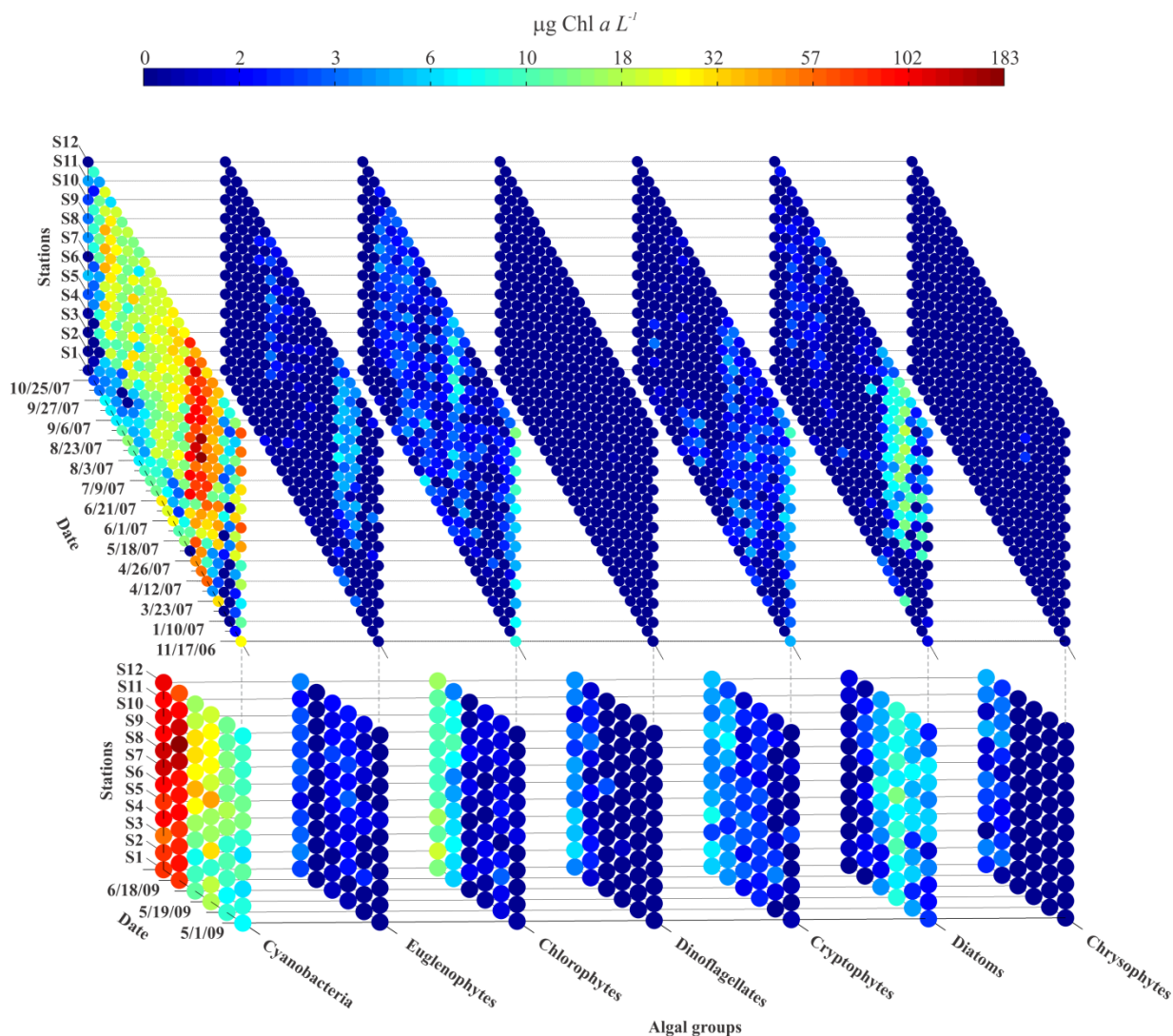


Fig. 4.3. ChemTax-derived concentrations of algal groups during 2006-2007 (top panel) and 2009 (bottom panel).

#### 4.3.2 Satellite Data

The main issues encountered with OCM data before algorithm development were striping, calibration error and atmospheric correction. The ADM destriping algorithm developed by Lyon (2009) was successful in removing the effects of striping in all OCM images. Large calibration errors resulted in low TOA radiances. Since the atmospheric correction terms are computed independently, upon applying these corrections to the lower than anticipated TOA

radiance, negative  $nL_w$  values were obtained before vicarious calibration. The developed vicarious calibration coefficients were able to correct for the calibration errors satisfactorily (Dash et al., in review). Unlike SeaDAS for SeaWiFS, OCM does not have a standard atmospheric correction procedure in place. The Case 2 type waters in case of Lac des Allemands further complicates the problem, due to which desired results could not be obtained by processing of OCM data through SeaDAS (Dash et al., in review). Therefore, an atmospheric correction procedure was developed with the capability to process turbid Case 2 waters to utilize the full potential of OCM. Using this atmospheric correction procedure realistic  $R_{rs}$  values could be obtained from OCM data (Dash et al., in review).

*In situ*  $R_{rs}$  obtained with the GER 1500 radiometer were weighted with the relative spectral response function of OCM to produce  $R_{rs}$  values at the six OCM bands. *In situ*  $R_{rs}$  and OCM  $R_{rs}$  (before and after destriping) were compared to gauge the performance of the combined destriping, vicarious calibration and atmospheric correction approach (Dash et al., in review). Fig. 3.9 shows this comparison for June 21 and October 11, 2007 at a central lake site. Clearly, destriping improved the  $R_{rs}$  spectra and reduced the abnormalities in the blue bands. The destriping smoothed out the noise from bad detectors and the destriped OCM  $R_{rs}$  spectra matched closely with the *in situ* radiometer spectra. The close fit between the radiometer spectra and the corrected  $R_{rs}$  spectra proved that the results from the combined destriping, vicarious calibration and atmospheric correction procedure were accurate and ready for use.

#### 4.3.3 Optimization of Algorithms for PC

OCM  $R_{rs}$  spectra of six selected sites with high, medium and low PC concentrations shown in Fig. 4.4A demonstrate that the spectral slopes of bands 4 and 5 are sensitive to variation in PC concentrations. The slopes decreased systematically from 0.0001163 to

0.0000379 with decrease in PC concentrations from 290.51 to 1.51  $\mu\text{g/L}$ . On the contrary, the spectral ratio was not sensitive to variation in PC concentrations. For example the highest spectral ratio of 2.38 was observed for a PC concentration of 7.64  $\mu\text{g/L}$  while a lower ratio of 1.74 was observed for a PC concentration of 290.51  $\mu\text{g/L}$ . Therefore, a spectral slope algorithm was developed as the band ratio approach did not produce significant correlation. Fig. 4.4B shows that PC is moderately correlated to Chl *a* concentrations ( $R^2 = 0.3957$ ;  $n=84$ ;  $p<0.0001$ ), which indicates the requirement of two separate algorithms for PC and Chl *a*. Simultaneously, the non-negligible correlation also suggests the necessity of removing the contribution of Chl *a* to the PC algorithm and vice versa, especially since both PC and Chl *a* algorithms share a band (OCM band 5).

PC concentrations and OCM  $R_{rs}$  for six dates in 2007 were used for algorithm development and four dates in 2009 were used for validation. Table 4.1 lists the regression results of the algorithms developed for PC. An exponential relationship produced the highest  $R^2$  between the spectral slopes of OCM  $R_{rs}$  at bands 4 and 5 against PC ( $R^2 = 0.7248$ ,  $n = 72$ ,  $p<0.0001$ ; Table 4.1). Application of this PC algorithm to the 2009 validation dataset yielded an

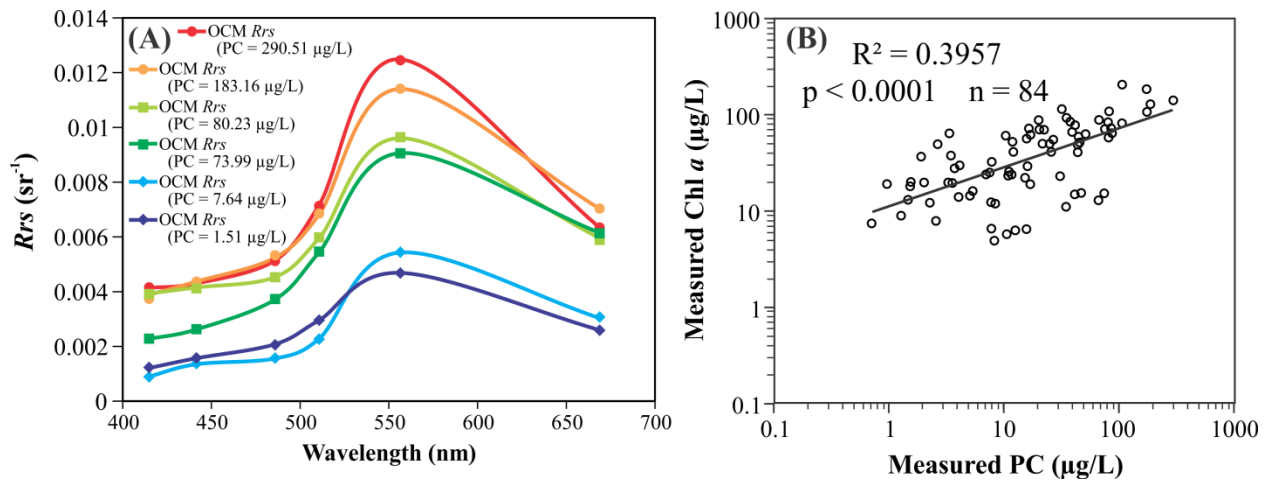


Fig. 4.4. (A) Comparison of OCM  $R_{rs}$  spectra when low, moderate and high PC concentrations were measured. (B) Relationship between field measured PC and Chl *a*.

RMSE of 37.40  $\mu\text{g/L}$  ( $n = 48$ , relative RMSE = 10.41%, MAE = 21.860  $\mu\text{g/L}$ , relative MAE = 6.084%) between the measured and estimated PC (Table 4.1).

A comprehensive analysis of the effects of optically active constituents- water, Chl *a*, NAP and CDOM was carried out on the optical signals of PC at the wavelengths 510.6 and 556.4 nm. First, the contribution of Chl *a* was subtracted from OCM  $R_{rs}$ . This was achieved by computing  $R_{rs}$ , accounting for absorption by water+Chl *a* and backscattering by (i) water, (ii) water+Chl *a*, (iii) water+total particulate matter and then subtracting the computed  $R_{rs}$  from OCM  $R_{rs}$ . The best regression results were obtained for PC when the computed  $R_{rs}$  accounted for absorption by water+Chl *a* with backscattering by water ( $R^2 = 0.7374$ ,  $n = 72$ ,  $p < 0.0001$ ; Table 4.1). Validation of this algorithm using the 2009 dataset provided an RMSE of 37.15  $\mu\text{g/L}$  ( $n = 48$ , relative RMSE = 10.34%, MAE = 21.806  $\mu\text{g/L}$ , relative MAE = 6.069%; Table 4.1). Second, the contributions of Chl *a* and NAP were subtracted from OCM  $R_{rs}$ . It was achieved following a similar approach as above by computing  $R_{rs}$ , accounting for absorption by water+Chl *a*+NAP. The best results were obtained when computed  $R_{rs}$  accounted for backscattering by water ( $R^2 = 0.7449$ ,  $n = 72$ ,  $p < 0.0001$ ; Table 4.1). Application of this PC algorithm to the 2009 validation dataset yielded a slightly lower RMSE than the previous algorithm ( $n = 48$ , RMSE = 36.98  $\mu\text{g/L}$ , relative RMSE = 10.29%, MAE = 21.797  $\mu\text{g/L}$ , relative MAE = 6.066%; Table 4.1). Third, subtraction of the contributions of Chl *a*, NAP and CDOM together from OCM  $R_{rs}$  was attempted. It was achieved following the same approach and accounting for absorption by water+Chl *a*+NAP+CDOM. The best results were obtained for PC when computed  $R_{rs}$  accounted for backscattering by water ( $R^2 = 0.7450$ ,  $n = 72$ ,  $p < 0.0001$ ; Fig. 4.5A, Table 4.1). Validation of this algorithm produced the lowest RMSE between the measured



and estimated PC ( $n = 48$ , RMSE = 36.92  $\mu\text{g/L}$ , relative RMSE = 10.27%, MAE = 21.791  $\mu\text{g/L}$ , relative MAE = 6.065%; Fig. 4.5B, Table 4.1).

Accounting for the contributions of absorption by water, Chl *a*, NAP and CDOM (either individually or together) improved the algorithms, but only marginally (Table 4.1). Since, there were no significant discernible differences between the scatter plots of all the PC algorithms, only the final scatter plots (when the absorptions of water, Chl *a*, NAP and CDOM together were accounted for in the computed  $R_{rs}$ ) are presented in Fig. 4.5A and B. It was observed that subtracting the computed  $R_{rs}$  accounting for the contributions of backscattering by water+Chl *a* and water+total particulate matter did not produce better predictive algorithms than subtracting the computed  $R_{rs}$  with contributions of just water. The  $R^2$  of 0.7450 obtained for the best PC algorithm, decreased to  $R^2$  of 0.4269 ( $n=72$ ,  $p<0.0001$ ) by incorporating contributions of backscattering by water+Chl *a* and to  $R^2$  of 0.3667 ( $n=72$ ,  $p<0.0001$ ) by incorporating contributions of backscattering by water+total particulate matter. This study did not include field-measured backscattering coefficients, therefore developed algorithms from the literature were used to compute the backscattering by Chl *a* and total particulate matter. Since, backscattering plays a pivotal role in the computed  $R_{rs}$ , small uncertainties in the computed backscattering of Chl *a* and total particulate matter rendered larger errors in the computed  $R_{rs}$ . As a result, subtraction of the computed  $R_{rs}$  with contributions of water+Chl *a* and water+total particulate matter to backscattering yielded poorer fits to the data used in this study. Therefore,  $b_{b\text{Chl } a}$  and  $b_{bp}$  were assumed to be invariant between the OCM  $R_{rs}$  at bands 4 and 5, particularly as the bands are closely spaced.

In summary, through the development of four PC algorithms it was observed that by removing the contributions of Chl *a* absorption, an algorithm with lower RMSE was obtained

than that of no subtraction. Further, by removing the contributions of Chl *a* and NAP absorption, an algorithm with even lower RMSE was obtained. The best algorithm was obtained by removing the contributions of Chl *a*, NAP and CDOM absorptions. The lack of trend in the validation residuals, relatively large sample size, strong positive slopes, and consistent patterns in the 2009 PC estimates indicate the validity of this approach.

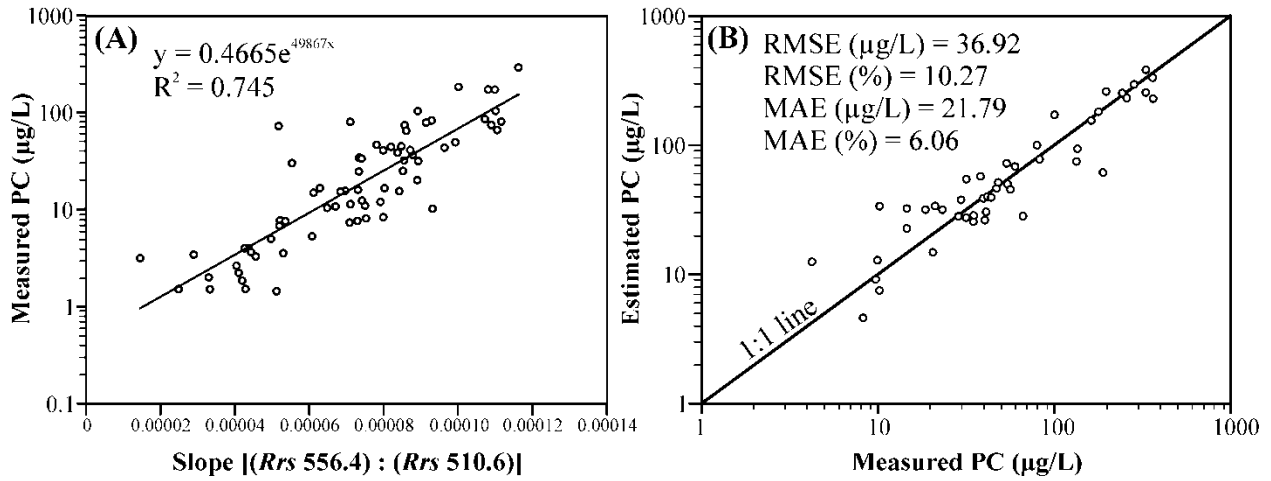


Fig. 4.5. (A) PC algorithm developed using OCM  $R_{rs}$  with subtraction of  $R_{rs}$  accounting for absorption by water+Chl *a*+NAP+CDOM and backscattering by water using 2006-2007 database (B) PC estimated from OCM data using this algorithm versus measured PC of 2009.

#### 4.3.4 Optimization of Algorithms for Chl *a*

From the comparisons between the use of single bands, spectral ratio, and spectral slopes of OCM  $R_{rs}$ , it was observed that the spectral slopes of OCM  $R_{rs}$  at bands 5 (556.4 nm) and 6 (669 nm) yielded the best set of algorithms for Chl *a*. Table 4.2 lists the regression results of the algorithms developed for Chl *a*. Data of all the nine dates when clear-sky OCM data were obtained in 2006-2007 used for Chl *a* algorithm development and data of four clear-sky dates in

Table 4.1 Regression results of PC algorithms. P-values were less than 0.0001 for all the PC algorithms. Relative RMSE and relative MAE are given in %.

	Components subtracted	Structure of the Algorithms	PC Algorithms (2007 data)	Validation results (2009 data)
1	No subtraction	OCM $R_{rs}$ Vs. PC	$0.4452e^{50039 \times \text{spectral slope}}$ ( $R^2=0.7248$ , n=72)	RMSE=37.40 $\mu\text{g/L}$ (10.41%) MAE=21.860 $\mu\text{g/L}$ (6.084%)
2	Chl $a$	OCM $R_{rs} - \frac{bb(w)}{\{a(w)+a(\text{Chl } a)\}+\{bb(w)\}}$ $R_{rs}$ Vs. PC	$0.5106e^{49280 \times \text{spectral slope}}$ ( $R^2=0.7374$ , n=72)	RMSE=37.15 $\mu\text{g/L}$ (10.34%) MAE=21.806 $\mu\text{g/L}$ (6.069%)
3	Chl $a$ + NAP	OCM $R_{rs} - \frac{bb(w)}{\{a(w)+a(\text{Chl } a)+a(\text{NAP})\}+\{bb(w)\}}$ $R_{rs}$ Vs. PC	$0.4708e^{49812 \times \text{spectral slope}}$ ( $R^2=0.7449$ , n=72)	RMSE=36.98 $\mu\text{g/L}$ (10.29%) MAE=21.797 $\mu\text{g/L}$ (6.066%)
4	Chl $a$ + NAP + CDOM	OCM $R_{rs} - \frac{bb(w)}{\{a(w)+a(\text{Chl } a)+a(\text{NAP})+a(\text{CDOM})\}+\{bb(w)\}}$ $R_{rs}$ Vs. PC	$0.4665e^{49867 \times \text{spectral slope}}$ ( $R^2=0.7450$ , n=72)	RMSE=36.92 $\mu\text{g/L}$ (10.27%) MAE=21.791 $\mu\text{g/L}$ (6.065%)

Table 4.2 Regression results of Chl  $a$  algorithms. P-values were less than 0.0001 for all the Chl  $a$  algorithms. Relative RMSE and relative MAE are given in %.

	Components subtracted	Structure of the Algorithms	Chl $a$ Algorithms (2007 data)	Validation results (2009 data)
1	No subtraction	OCM $R_{rs}$ Vs. Chl $a$	$7.9449e^{50865 \times \text{spectral slope}}$ ( $R^2=0.7143$ , n=108)	RMSE=34.17 $\mu\text{g/L}$ (17.19%) MAE=17.17 $\mu\text{g/L}$ (8.64%)
2	PC	OCM $R_{rs} - \frac{bb(w)}{\{a(w)+a(\text{PC})\}+\{bb(w)\}}$ $R_{rs}$ Vs. Chl $a$	$9.065e^{50279 \times \text{spectral slope}}$ ( $R^2=0.7450$ , n=72)	RMSE=32.96 $\mu\text{g/L}$ (16.59%) MAE=17.12 $\mu\text{g/L}$ (8.61%)
3	PC + NAP	OCM $R_{rs} - \frac{bb(w)}{\{a(w)+a(\text{PC})+a(\text{NAP})\}+\{bb(w)\}}$ $R_{rs}$ Vs. Chl $a$	$7.8345e^{51821 \times \text{spectral slope}}$ ( $R^2=0.7502$ , n=72)	RMSE=31.87 $\mu\text{g/L}$ (16.04%) MAE=16.85 $\mu\text{g/L}$ (8.48%)
4	PC + NAP + CDOM	OCM $R_{rs} - \frac{bb(w)}{\{a(w)+a(\text{PC})+a(\text{NAP})+a(\text{CDOM})\}+\{bb(w)\}}$ $R_{rs}$ Vs. Chl $a$	$7.6349e^{52223 \times \text{spectral slope}}$ ( $R^2=0.7510$ , n=72)	RMSE=31.19 $\mu\text{g/L}$ (15.70%) MAE=16.56 $\mu\text{g/L}$ (8.33%)

2009 were used for validation. Similar to PC algorithms, an exponential relationship was found to produce highest  $R^2$  between the spectral slopes and Chl  $a$  ( $R^2 = 0.7143$ ,  $n = 108$ ,  $p < 0.0001$ ; Table 4.2). Application of this algorithm to the 2009 dataset yielded an RMSE of 34.17  $\mu\text{g/L}$  with a relative RMSE of 17.19% ( $n = 48$ ,  $\text{MAE} = 17.17 \mu\text{g/L}$ , relative  $\text{MAE} = 8.64\%$ ) between the measured and estimated Chl  $a$  (Table 4.2).

A comprehensive analysis of the effects of the optically active constituents (water, PC, NAP and CDOM) was performed on the Chl  $a$  signal at the wavelengths 669 and 556.4 nm. First, the contribution of PC was subtracted from OCM  $R_{rs}$ , which was achieved by computing  $R_{rs}$  accounting for absorption by water+PC and backscattering by water. A higher  $R^2$  of 0.7450 ( $n = 72$ ,  $p < 0.0001$ ; Table 4.2) was obtained compared to the algorithm with no subtraction. Validation with the 2009 dataset yielded an RMSE of 32.96  $\mu\text{g/L}$  ( $n = 48$ , relative RMSE of 16.59%,  $\text{MAE} = 17.12 \mu\text{g/L}$ , relative  $\text{MAE} = 8.61\%$ ; Table 4.2). The subtraction of the contribution of both PC and NAP absorption produced an algorithm with an  $R^2$  of 0.7502 ( $n = 72$ ,  $p < 0.0001$ ; Table 4.2) and validation with the 2009 dataset produced an RMSE of 31.87  $\mu\text{g/L}$  ( $n = 48$ , relative RMSE = 16.04%,  $\text{MAE} = 16.85 \mu\text{g/L}$ , relative  $\text{MAE} = 8.48\%$ ; Table 4.2). Finally, subtraction of the contributions of PC, NAP and CDOM absorption together produced the best  $R^2$  of 0.7510 ( $n = 72$ ,  $p < 0.0001$ ; Fig. 4.6A, Table 4.2) and validation yielded an RMSE of 31.19  $\mu\text{g/L}$  ( $n = 48$ , relative RMSE = 15.70%,  $\text{MAE} = 16.56 \mu\text{g/L}$ , relative  $\text{MAE} = 8.33\%$ ; Fig. 4.6B, Table 4.2).

Although PC absorption is negligible at 669 nm, its absorption is relatively strong at 556.4 nm as seen in Fig. 1.3. Therefore, a slight improvement in the Chl  $a$  algorithm was observed after the subtraction of computed  $R_{rs}$  with the water+PC absorption from OCM  $R_{rs}$ . The subtraction of computed  $R_{rs}$  with the water+PC+NAP absorption and with the

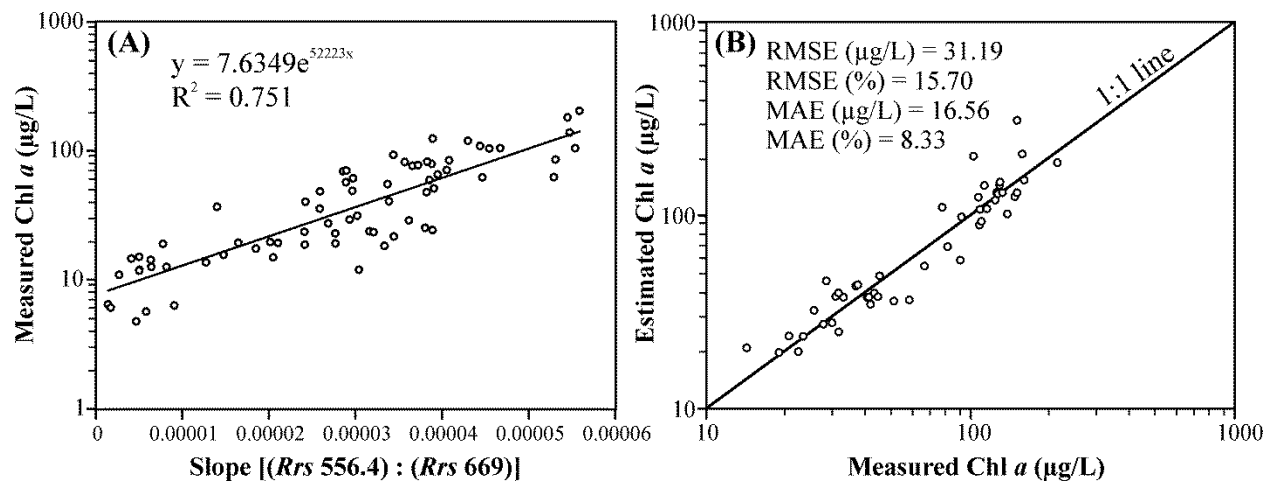


Fig. 4.6. (A) Chl *a* algorithm developed using OCM *R<sub>rs</sub>* with subtraction of *R<sub>rs</sub>* accounting for absorption by water+PC+ NAP+CDOM and backscattering by water using 2006-2007 database (B) Chl *a* estimated from OCM data using this algorithm versus measured Chl *a* of 2009.

water+PC+NAP+CDOM absorption from OCM *R<sub>rs</sub>* improved the performance of the Chl *a* algorithms only marginally. Nevertheless, the best algorithm for Chl *a* was the algorithm obtained after subtraction of computed *R<sub>rs</sub>* with the water+PC+NAP+CDOM absorption and thus, the scatter plots of this algorithm calibration and validation only are presented in Fig. 4.6A and B.

#### 4.3.5 Optimization of Algorithms for Accessory Pigments

HPLC analysis of algal pigments revealed that the dominant carotenoids were: echinenone, zeaxanthin and myxo-xanthophyll- a pigment suite characteristic of cyanobacteria (Schalles and Yacobi, 2000). A spectral reflectance curve given by Schalles and Yacobi, (2000) showed that the carotenoids have an absorption maxima between 450 and 530 nm which induces a prominent shoulder toward the lower wavelengths of the green reflectance peak. Therefore, a relationship was expected between the spectral slopes of bands 4 (510.6 nm) and 5 (556.4 nm) with the carotenoids, echinenone and zeaxanthin, which could potentially be used for mapping specific cyanobacterial taxa. However, the use of our entire dataset of nine dates did not

demonstrate a robust relationship between zeaxanthin and echinenone with OCM  $R_{rs}$ . A weak, positive relationship ( $R^2 = 0.5265$ ,  $n=108$ ,  $p < 0.0001$ ) was found between the spectral slopes of OCM  $R_{rs}$  at bands 4 and 5 with echinenone, and absolutely no relationship ( $R^2 = 0.0015$ ,  $n=108$ ,  $p = 0.6923$ ) with zeaxanthin. Application of the echinenone algorithm to the 2009 dataset yielded a high relative RMSE of 64.52% and a relative MAE of 50.94% with an RMSE of 26.85  $\mu\text{g/L}$ . The algorithm for echinenone was further fine-tuned with subtraction of the effects of water, NAP, CDOM, Chl  $a$ , and PC and a slightly improved correlation ( $R^2 = 0.5405$ ,  $n=72$ ,  $p < 0.0001$ ) was obtained. However, validation of this algorithm on the 2009 dataset did not improve the estimations significantly (relative RMSE = 53.61%, relative MAE = 44.08%) and yielded an RMSE of 22.31  $\mu\text{g/L}$ .

#### 4.3.6 Application of Algorithms to OCM Image Data

PC and Chl  $a$  images were generated by applying the developed algorithms to OCM data over Lac des Allemands. Field data indicated high concentrations of PC and Chl  $a$  on April 20, 2007 and low concentrations on June 21, 2007. These new image products for these two field dates are shown adjacent to true color images in Fig. 4.7. Basic statistics are given in Table 4.3 comparing the minimum and maximum values obtained at the 12 sites with the minimum and maximum values estimated by the algorithms over the entire lake. The April 20, 2007 images clearly show the high PC and Chl  $a$  concentrations indicated by the field data and as observed in the true color image. Higher values were found at regions of the lake that were not covered by the sampling stations (Table 4.3). In both images lowest concentrations of PC and Chl  $a$  were observed as expected in the southwestern part of the lake where Bayou Chevreuil brings in high amounts of suspended sediments and dissolved material. This water mass extended towards the northeast. The June 21, 2007 images exhibit the low concentrations of PC and Chl  $a$  as observed

in the field data except for few locations where a relatively high concentration of PC and Chl *a* was mapped (Table 4.3). These locations were missed during field observations since there were no sampling stations at those locations. The PC and Chl *a* images demonstrated good agreement with the true color images while the true color images do not show the variability that is obtained by applying the algorithms to the satellite data. The higher range of values detected in regions of the lake that were not covered by field sampling clearly demonstrates the advantage of using this satellite-based technique.

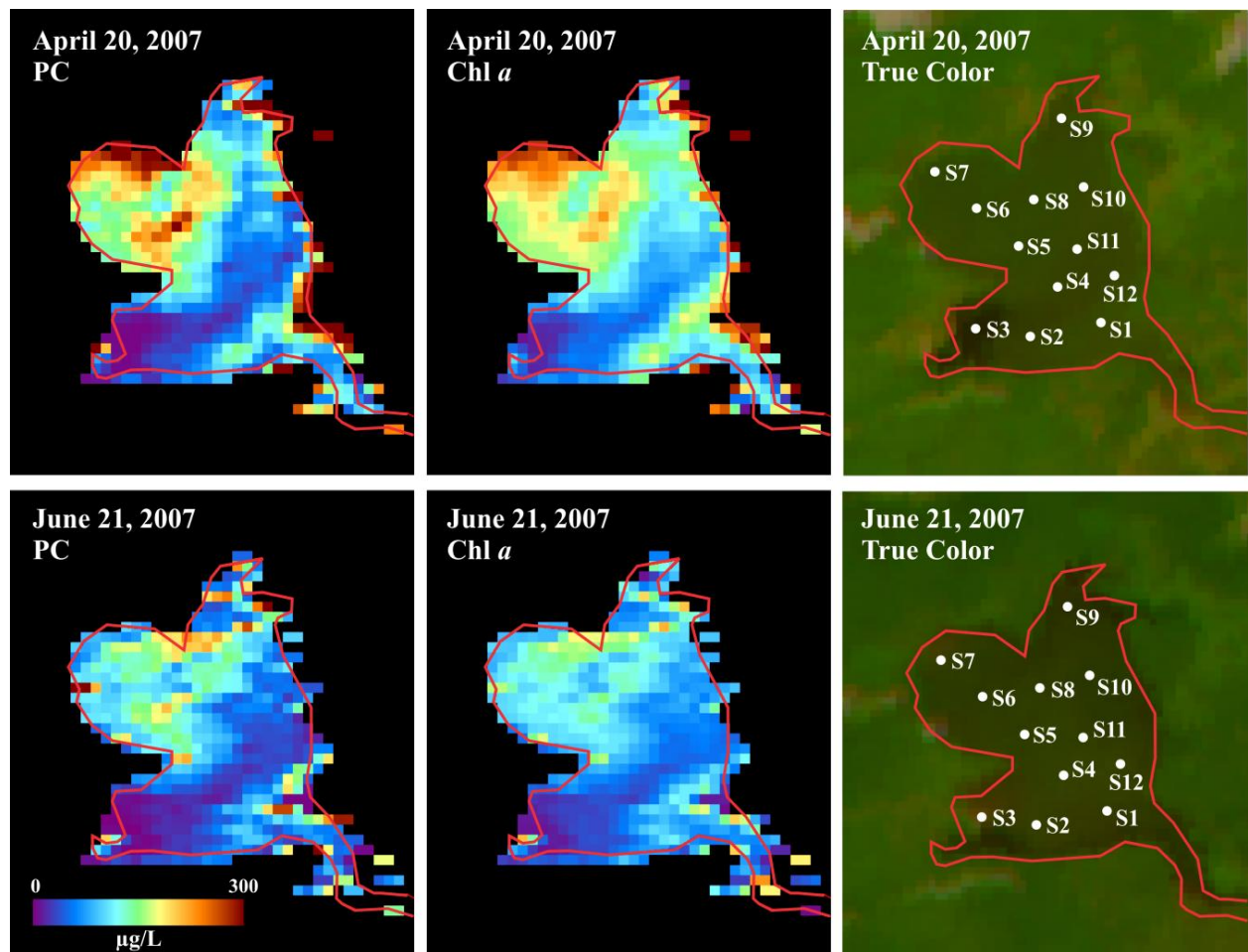


Fig. 4.7. PC, Chl *a* and true color images derived from OCM data of April 20, 2007 and June 21, 2007. The PC and Chl *a* images were obtained by application of PC algorithm 2 and Chl *a* algorithm 2. The 12 sampling sites are indicated in the true color images.

Table 4.3 Measured and image-derived concentrations of PC and Chl *a* on April 20, 2007 (with higher concentration of PC and Chl *a*) and June 21, 2007 (with lower concentration of PC and Chl *a*). The image-derived PC and Chl *a* were obtained by application of PC algorithm 2 and Chl *a* algorithm 2. Note that high concentrations of PC and Chl *a* were obtained at regions of the lake that were not covered by field sampling.

	April 20, 2007				June 21, 2007			
	Field-measured		Image-derived		Field-measured		Image-derived	
	PC	Chl <i>a</i>	PC	Chl <i>a</i>	PC	Chl <i>a</i>	PC	Chl <i>a</i>
<i>n</i>	12	12	521	521	12	12	517	517
Min	3.44	12.57	1.44	6.05	3.99	11.96	1.52	6.74
Max	171.85	92.86	295.59	256.07	30.12	31.40	198.87	179.04
SD	45.66	25.92	51.91	44.06	7.46	5.57	42.58	38.91

## 4.4. Discussion

### 4.4.1 Usefulness of Algorithms Developed from Satellite Data

Satellite remote sensing of algal blooms is both labor and cost effective in comparison to airborne remote sensing or using hand-held remote sensing instruments. In most cases, the area that needs to be monitored is large and only satellite sensors can provide the spatial and synoptic coverage needed (Kutser, 2009). The three most cited PC algorithms by Dekker et al. (1993), Schalles and Yacobi (2000), and Simis et al. (2005) were developed and validated with hyperspectral data from hand-held remote sensing instruments (Ruiz-Verdu et al., 2008). The algorithms by Dekker (1993) and Schalles and Yacobi (2000) cannot yet be applied to operational satellite sensors with global coverage as the required wavebands are lacking (Ruiz-Verdu et al., 2008). The algorithm by Simis et al. (2005), based on the MERIS sensor's band settings, yielded the best estimations from hand-held radiometer data (Simis et al., 2007; Randolph et al., 2008; Ruiz-Verdu et al., 2008). However, it did not produce the desired results when applied to MERIS data (Simis et al., 2006; Ruiz-Verdu et al., 2008). It was shown to be limited by sensitivity of the atmospheric correction procedure to high NIR reflectances over turbid water pixels and near land (Simis et al., 2006; Ruiz-Verdu et al., 2008). When an



algorithm developed from hand-held radiometer data does not comply with the spectral bands available from a satellite-borne sensor or does not produce acceptable results with the satellite data, it is applicable to radiometer data only. Thereby, it can replace tedious microscopic or analytic procedures to measure the algal concentrations in the laboratory, but the radiometer data collection is still required, which is not labor and cost effective and cannot provide a synoptic view. An algorithm for obtaining algal concentrations is most useful when it can be applied to satellite data. Additionally, it becomes partly insensitive to the residual atmospheric correction and calibration errors that are intrinsic to the sensor if it is developed from satellite data. Therefore, the algorithms in this study were developed and validated using satellite data.

#### 4.4.2 Advantages of Using OCM Data

The two most critical parameters for choosing a satellite sensor for operational monitoring of phytoplankton blooms in coastal areas are the sensor's revisit time and the spatial resolution. Other important considerations are radiometric sensitivity and spectral resolution. Optimal sensors based on these criteria are MODIS (high resolution bands 1 and 2), MERIS (Kutser, 2009) and OCM. The OCM sensor has a more frequent revisit time than MERIS and OCM bands have narrower bandwidth than MODIS bands 1 and 2. Additionally, a robust procedure has been developed for the atmospheric correction and vicarious calibration of OCM data (Dash et al., in review). This atmospheric correction procedure does not include out-of-band corrections, whitecap corrections, surface roughness influences and contributions of  $L_a$  to diffuse transmittance. However, these corrections would not significantly change the overall accuracy of the procedure particularly for small lakes on low wind speed days when whitecap and surface roughness terms are minimal. The high closure between the radiometer  $R_{rs}$  and

OCM  $R_{rs}$  shown in Fig. 3.9 demonstrates the effectiveness of the combined atmospheric correction and vicarious calibration procedure.

Another major advantage of using OCM data is that it has identical bands as SeaWiFS which is considered to be one of the most successful ocean color missions due to the duration, consistency, stability, coverage, documented quality, and accessibility of data (Siegel et al., 2004). Since, the spatial resolution of SeaWiFS data is not adequate for studying small water bodies such as Lac des Allemands, the higher resolution OCM data was chosen for the development of cyanobacteria algorithms. Wherever spatial resolution is not an issue, the algorithms developed from OCM can be easily modified for application to SeaWiFS imagery. These algorithms may also be applicable to OCM-2 and OCM-3 data. With this approach, the retrieved results from OCM and SeaWiFS could be meaningfully compared and a possible merger of datasets could be envisaged. OCM data has been successfully used for various practical applications including locating potential fishing zones (Solanki, et al., 2000 and 2003; Nayak, et al., 2003), surface Chl *a* estimation (Chauhan et al., 2002; Nagamani, et al., 2007), and detecting *Trichodesmium* blooms (Sarangi et al., 2005). This study is the first use of OCM data for quantifying freshwater cyanobacterial concentrations.

#### 4.4.3 Assessment of the Developed Algorithms

Although subtraction of OACs improved the performance of the algorithms, the increases were not large. Therefore, any one of the four PC algorithms could be used for quantifying cyanobacteria and, similarly, any Chl *a* algorithm of the four Chl *a* algorithms could be used for mapping the total phytoplankton assemblage. The choice would be based upon the availability of measurements of the OACs or the inherent optical properties. A plausible reason for the lack of variability in performance of the algorithms could be the dominance of cyanobacteria in Lac des

Allemands for the entire study period. Garcia et al. (2010) indicated the occurrence of alternating blooms of *Microcystis* sp. and *Anabaena* spp. in Lac des Allemands over the eight month period from December, 2006 to July, 2007 of this study. However, we had no success in demonstrating a robust relationship for specific cyanobacterial taxa. Our results concerning the echinenone and zeaxanthin algorithms confirm those of Schalles and Yacobi (2000), and are attributed to their relatively low concentrations and lower absorption activity per unit of pigment.

The PC and Chl *a* algorithms developed in this study are valid mainly within the range of values used in algorithm calibration. Although a wide range of PC and Chl *a* concentrations were used for development of these algorithms, which were responsible for the wide range of spectral slopes (0 to  $1.2 \times 10^{-4}$  for PC and  $-4.0 \times 10^{-5}$  to  $6.0 \times 10^{-5}$  for Chl *a*), any slopes higher than the spectral slopes used for the algorithm development would be due to more concentrated algal blooms or an artifact of the satellite data or error in the atmospheric correction. Those scenarios can be detected more readily since these algorithms are of exponential form and those data points should be viewed with some caution.

For the algorithms to be uniformly valid over all areas (or all bio-optical regimes) of the lake, a holistic approach was followed to minimize the influence of other OACs. The contributions of these constituents to the total  $R_{rs}$  were determined by computing  $R_{rs}$  analytically. The  $R_{rs}$  computations were mainly based on absorption coefficients of the OACs and backscattering by water, since it was found that the incorporation of phytoplankton and particulate backscattering negatively affected algorithm performance. Use of field measured particulate and phytoplankton backscattering, especially since cyanobacteria have gas vacuoles, would have possibly improved the performance of the algorithms.

The PC algorithm developed by Simis et al. (2005) was also based on computations of absorption coefficients. They assumed the absorption coefficient of Chl *a* at 620 nm to be 24% of the absorption coefficient of Chl *a* at 665 nm and subtracted it from total absorption at 620 nm to derive PC concentrations. They subtracted the contributions of CDOM and NAP from  $R_{rs}$  by introducing a constant correction factor. They also assumed that backscattering is spectrally independent and computed a constant backscattering coefficient from the  $R_{rs}$  at 778 nm. Dekker et al. (1992) subtracted the contributions of SPM and CDOM for quantifying PC from remotely sensed data, by computing absorption coefficients of SPM and CDOM from specific absorption coefficients. They calculated total backscattering coefficients from computed subsurface irradiance reflectances. However, they did not subtract the contributions of Chl *a* for PC algorithm development. In this research the concentrations of Chl *a*, PC and NAP and their specific absorption coefficients, and absorption coefficients of water and CDOM were used to compute  $R_{rs}$  with just water in the backscattering term and they were subtracted from the OCM  $R_{rs}$  sequentially for algorithm development. With each subtraction the accuracy of algorithms increased. The best algorithm for PC resulted when the contributions of Chl *a*, NAP, CDOM and water were subtracted, and the best algorithm for Chl *a* resulted when the contributions of PC, NAP, CDOM and water were subtracted.

The Chl *a* and PC algorithms developed in this study used fixed specific absorption coefficients. Employing a fixed specific absorption coefficient of PC, Simis et al. (2005) obtained an  $R^2$  of 0.77 with slope and intercept values of 0.59 and 29.03, respectively in two lakes in the Netherlands. Randolph et al. (2008) estimated PC concentrations using the Simis et al. (2005) algorithm in two Indianapolis reservoirs and reported an  $R^2$  of 0.75 with slope and intercept values 0.58 and 34.76 respectively and an RMSE of 22.15  $\mu\text{g/L}$  for one of the

reservoirs. The validation results of the PC algorithms presented here ( $R^2 = 0.87$  with slope and intercept values of 0.86 and 7.56 respectively for the best PC algorithm) were comparable to these aforementioned studies. However, the RMSE values were higher (36.92  $\mu\text{g/L}$  for the best PC algorithm) mainly because in this study a wider range of PC concentrations (2.75 – 363.50  $\mu\text{g/L}$ ) were used in compared to the range of PC concentrations (2-135  $\mu\text{g/L}$ ) used by Randolph et al. (2008). The results reported here are of significance considering the PC algorithms developed in this study (1) employed satellite data for both development and validation, and (2) used wavelengths 510.6 and 556.4 nm, where a lower PC absorption activity is usually observed. In contrast, the aforementioned studies (1) employed radiometer data for both algorithm development and validation, and (2) used the PC absorption maximum at 620 nm for algorithm development.

The main goal in mapping algal blooms using satellite remote sensing is real-time surveillance. Therefore, it is critical for an algorithm to achieve accurate results over a broad range of conditions. However, variation in absorption efficiency and packaging effect are potential sources of error in all the absorption coefficient based algorithms. Pigment absorption efficiency is suggested to be a function of season, environmental conditions, nutrient and light availability, and phytoplankton composition (Metsamaa et al., 2006; Randolph et al., 2008). For example, Dekker (1993) obtained eight different specific absorption coefficients for PC at 624 nm using 8 samples from the same water body, Lake Vecht ranging from 0.0014 to 0.0058  $\text{m}^2 \text{mg}^{-1}$  (mean = 0.0032  $\text{m}^2 \text{mg}^{-1}$  and SD = 0.0012  $\text{m}^2 \text{mg}^{-1}$ ). Simis et al. (2005) investigated the fluctuations in specific absorption coefficients of PC and Chl *a* at 620 nm over the period March-November 2003 for Lake Loosdrecht, and observed a high variability with an average value of 0.0095  $\text{m}^2 \text{mg}^{-1}$  (SD = 0.0033  $\text{m}^2 \text{mg}^{-1}$ ) for the specific absorption coefficients of PC. Further,

Simis et al. (2007) observed that a change in pH of the buffer solution for extraction increased the extraction efficiency, but simultaneously decreased the average specific absorption coefficients of PC at 620 nm from  $0.0095 \text{ m}^2 \text{ mg}^{-1}$  to  $0.007 \text{ m}^2 \text{ mg}^{-1}$ . In this study, the average specific absorption coefficients of PC measured using a dilution series of PC standards at 620 nm was found to be  $0.006332 \text{ m}^2 \text{ mg}^{-1}$ , which compares closely with the specific absorption coefficients of PC mentioned above. Three PC algorithms and three Chl *a* algorithms developed in this study are based on subtraction of absorption of NAP, Chl *a* or PC and CDOM. As high variability exists in specific absorption coefficients and the CDOM spectral slope parameter, application of these six PC and Chl *a* algorithms to data of different time periods or different locations will require comparison of the specific absorption coefficients and CDOM spectral slope parameters used in this study with that of the water body under investigation.

#### 4.5. Conclusions

Despite the lack of a 620-nm band in Oceansat-1 OCM, algorithms for mapping cyanobacteria in a small freshwater lake ( $49 \text{ km}^2$ ), based on the spectral reflectance slopes between 510 and 669 nm, were developed and validated. The spectral slope of OCM bands 4 and 5, located at 556.4 and 510.6 nm (with lower PC-specific absorption), were sensitive to changes in PC concentrations, and could be used to estimate PC concentrations between 2.75 and  $363.50 \text{ } \mu\text{g/L}$ . A straightforward approach was followed to subtract the contributions of additional OACs to separate the PC signal from total  $R_{rs}$ . A similar method was developed to estimate Chl *a*, where the contributions of PC and other OACs were separated. However, attempts of estimating carotenoids zeaxanthin, and echinenone with OCM spectral reflectance were unsuccessful, mainly due to their low absorption efficiency and relatively low concentrations.

The results presented here demonstrate the preliminary success of using the  $360 \times 236$  m resolution OCM data to map cyanobacterial blooms in a small lake. While more field data are required to further validate the long-term performance of the algorithms, at present the algorithms may be implemented to process OCM data in an automatic fashion to provide timely information on the lake's bloom conditions. Similarly, retrospective processing may provide a long-term time series of bloom characteristics to document potential trends. The applicability of the algorithms to other lakes, however, remains to be tested.

## CHAPTER 5

### SUMMARY AND FUTURE DIRECTIONS

#### 5.1. Summary

This dissertation presented a new approach for the development of a suite of algorithms for the quantification of the primary cyanobacterial pigment, phycocyanin (PC), and chlorophyll *a* (Chl *a*) within a Case 2 inland lake using the OCM sensor. The use of this sensor was essential due to its improved spatial resolution but its use presented several problems that had to be overcome. In aquatic remote sensing, the water-leaving radiance forms a small fraction of the total radiance received at the sensor altitude, with the main contribution being due to the atmosphere. Atmospheric correction of satellite data over Case 2 waters (typically found in lakes and estuaries) is challenging due to difficulties in accurately estimating the aerosol scattering. As a first step towards algorithm development, a procedure for the atmospheric correction and vicarious calibration of ocean color sensors for Case 2 waters was developed. Incorporation of this new customized atmospheric correction procedure enabled accurate retrieval of  $R_{rs}$  from OCM data in the Case 2 waters of Lac des Allemands, a fresh water lake connected to the Gulf of Mexico. This procedure is also applicable to data from other ocean color sensors.

For the development of the algorithms, extensive field data were collected coincident with clear-sky satellite overpasses and a multi-year database of the optically active constituents was generated for the lake. A set of bio-optical algorithms were developed for estimating cyanobacteria by quantifying PC and Chl *a* using the vicariously calibrated and atmospherically corrected OCM data. For the algorithms to be uniformly valid over all areas (or all bio-optical regimes) of the lake, a holistic approach was followed to minimize the influence of other optically active constituents on the algorithms. The subtraction of the contributions of optically active constituents improved the performance of the algorithms. The validation of the algorithms



on the 2009 dataset yielded a good correlation between the observed and predicted PC and Chl *a*. The higher range of values detected in regions of the lake that were not covered by field sampling clearly demonstrates the advantage of using this satellite-based technique.

This research is the first attempt to use OCM measurements to quantify cyanobacterial pigments using the newly developed techniques for atmospheric correction and vicarious calibration. Although the PC absorption maximum is located at 620 nm, it is a broad peak with a prominent shoulder toward lower wavelengths. A set of algorithms for mapping cyanobacteria, based on the PC pigment, were successfully developed using OCM bands 5 and 4 (centered at 556.4 and 510.6 nm, respectively). Additionally, for mapping the phytoplankton assemblages, a set of algorithms for Chl *a* were developed using OCM bands 5 and 6 (centered at 556.4 and 669 nm, respectively). The spectral slope between two bands produced the most accurate algorithms compared with those using spectral ratio or single bands. Additionally, the use of PC instead of PC/Chl *a* or PC+Chl *a* in the PC algorithm yielded the best results. This study is significant because it represents the first attempt of utilizing OCM data to quantify PC and the first effort of using satellite data for both development and validation of algorithms for quantitatively mapping cyanobacteria with  $R_{rs} < 600$  nm.

Based on the results obtained in this study, the following answers to the four research questions identified in this dissertation can be proposed:

- 1) Can spectral  $R_{rs}$  be retrieved accurately by applying a customized atmospheric correction and vicarious calibration procedure to OCM data?

An atmospheric correction procedure was developed for processing OCM data, based on the extensive work done for SeaWiFS. Since OCM-retrieved radiances were found to be abnormally low in the blue wavelength region, a vicarious calibration procedure was needed and

thus developed. The vicarious calibration, using SeaWiFS data, allowed conversion of OCM data to a known high quality standard. The results of this combined vicarious calibration and atmospheric correction procedure for OCM data over Case 1 and Case 2 waters were compared with the results from the SeaDAS processing of SeaWiFS and OCM data. Over Case 1 waters, the results from this procedure matched with SeaDAS results. Over Case 2 waters, the results from this procedure showed closure with *in situ* radiometric measurements, while SeaDAS produced negative normalized water-leaving radiances ( $nL_w$ ) and remote sensing reflectances ( $R_{rs}$ ). It was shown that it is possible and efficient to apply the newly developed atmospheric correction procedure, together with vicarious calibration, to obtain valid  $nL_w$  and  $R_{rs}$  values from OCM data over both Case 1 and Case 2 waters.

- 2) Can concentrations and spatial distributions of cyanobacteria be quantified using derived reflectance measurements?

Empirical inversion algorithms were developed to convert the OCM remote sensing reflectance ( $R_{rs}$ ) at bands 4 and 5 (centered at 510.6 and 556.4 nm, respectively) to concentrations of PC, the primary cyanobacterial pigment. A holistic approach was used to minimize the influence of other optically active constituents on the PC algorithm. Similarly, empirical algorithms to estimate Chl *a* concentrations were developed using OCM bands 5 and 6 (centered at 556.4 and 669 nm, respectively). The best PC algorithm ( $R^2=0.7450$ ,  $p<0.0001$ ,  $n=72$ ) yielded a root mean square error (RMSE) of 36.92  $\mu\text{g/L}$  with a relative RMSE of 10.27%, and a mean absolute error (MAE) of 21.79  $\mu\text{g/L}$  with a relative MAE of 6.06% (PC from 2.75-363.50  $\mu\text{g/L}$ ,  $n=48$ ). The best algorithm for Chl *a* ( $R^2=0.7510$ ,  $p<0.0001$ ) produced an RMSE of 31.19  $\mu\text{g/L}$  (relative RMSE = 16.56%) and a MAE of 16.56  $\mu\text{g/L}$  (relative MAE = 8.10%) (Chl *a* from 9.46 to 212.76  $\mu\text{g/L}$ ,  $n=48$ ). While more field data are required to further validate the long-

term performance of these algorithms, at present these algorithms provide the basis to establish a long time-series of cyanobacterial blooms in the Lac des Allemands using OCM data.

3) Are wavelengths less than 620 nm applicable for quantifying PC?

Although the PC absorption maximum is located at 620 nm, it is a broad peak with a prominent shoulder towards lower wavelengths. A set of algorithms for mapping cyanobacteria based on PC were successfully developed by taking advantage of the prominent PC absorption shoulder in this wavelength region using OCM bands 5 and 4, centered at 556.4 and 510.6 nm respectively.

4) Does subtraction of the effects of other optically active constituents improve the performance of the algorithms for mapping cyanobacterial pigments?

Accounting for the contributions of absorption by water, Chl *a*, NAP and CDOM (either individually or together) improved the PC algorithms, but only marginally. It was observed that subtracting the computed  $R_{rs}$  accounting for the contributions of backscattering by water+Chl *a* and water+total particulate matter did not produce better algorithms than subtracting the computed  $R_{rs}$  with contributions of just water. This study did not include field-measured backscattering coefficients, therefore developed algorithms from the literature were used to compute the backscattering by Chl *a* and total particulate matter. Since backscattering plays a pivotal role in the computed  $R_{rs}$ , small uncertainties in the computed backscattering of Chl *a* and total particulate matter rendered larger errors in the computed  $R_{rs}$ . As a result, subtraction of the computed  $R_{rs}$  with contributions of water+Chl *a* and water+total particulate matter to backscattering yielded poorer fits to the data used in this study. Therefore,  $b_{bChl\ a}$  and  $b_{bp}$  were assumed to be invariant between the OCM  $R_{rs}$  at bands 4 and 5, particularly as the bands are closely spaced.

## 5.2. Future Directions

The techniques developed and applied in this study could be applied to time-series of OCM data which can give a unique perspective on the seasonality of cyanobacterial occurrence. This could take this study beyond the technical ("case study") approach towards a 'big picture' i.e., to establish a long time-series of cyanobacterial blooms for Lac des Allemands. Incorporation of backscattering coefficients during decomposition of total  $R_{rs}$  has the potential for improving the performance of the algorithms. The three most cited PC algorithms, focusing on the 620 nm absorption maximum of PC were developed by Dekker et al. (1993), Schalles and Yacobi (2000), and Simis et al. (2005). These algorithms were developed and validated with hyperspectral data from hand-held remote sensing instruments. The algorithms by Dekker (1993) and Schalles and Yacobi (2000) cannot yet be applied to operational satellite sensors with global coverage as the required wavebands are lacking (Ruiz-Verdu et al., 2008). Prior attempts by Simis et al. (2005) to apply their PC algorithm to MERIS data were unsuccessful, due to inaccuracies in atmospheric correction of MERIS data. Since, the atmospheric correction procedure developed in this study is also producing good results with MERIS data (not shown), the PC algorithm developed by Simis et al. (2005) using radiometer data could be applied to MERIS data after atmospherically correcting MERIS data using the procedure developed in this study. In addition, new MERIS algorithms using the approach developed in this study could be developed. Thereafter, the performance of algorithms developed in this study and the PC algorithms for MERIS data mentioned above could be statistically compared with the results from the Simis et al. (2005) algorithm.

Application of these algorithms to radiometer data would reveal the performance of the algorithms without the effects of atmospheric correction and artifacts of satellite data. using the

approach developed in this study, new algorithms could be developed from radiometer data. Then, the performance of algorithms presented in this dissertation and the algorithms developed from radiometer data using the approaches used in this research could be compared with the performance of algorithms developed by Dekker et al. (1993), Schalles and Yacobi (2000), and Simis et al. (2005) using radiometer data.

Similar algorithms could also be developed for other ocean color sensors using the approach developed in this dissertation. Furthermore, these algorithms could be applied to clear-sky satellite data from all these sensors including OCM to obtain a time-series of the occurrence of cyanobacteria blooms in Lac des Allemands. All these algorithms could be applied to other lakes to test the validity of the algorithms in other systems. For bigger water bodies (e.g. Lake Pontchartrain, the Great Lakes, Lake Tahoe), algorithms for multiple satellite sensors including OCM, MERIS, MODIS, SeaWiFS and OCM-2 sensors could be developed, so that a merger of datasets would provide a time-series with much higher temporal resolution.

## REFERENCES

- Acker, J. G. (1994) The heritage of SeaWiFS: A Retrospective on the CZCS NIMBUS Experiment Team (NET) Program, *NASA Tech. Memo. 104566*, edited by S. B. Hooker and E. R. Firestone, NASA Goddard Space Flight Cent., Greenbelt, Md., 21- 44.
- Anderson, D. (2007) Freshwater. Retrieved on May 30, 2011 from <http://www.whoi.edu/redtide/page.do?pid=15775>
- Arnone, R. A., Martinolich, P., Gould, R. W. Jr., Stumpf, R. P. and Ladner, S. (1998) Coastal optical properties using SeaWiFS. *Proceedings Ocean Optics XIV, Kailua Kona, Hawaii, USA*, November 10-13.
- Barnes, R. A., Eplee, R.E., Schmidt, G. M., Patt, F. S. and McClain, C. R. (2001) The calibration of SeaWiFS. I. direct techniques, *Appl. Opt.*, 40, 6682-6700.
- Bricaud, A., Morel, A. and Prieur, L. (1981). Absorption by dissolved organic matter of the sea (yellow substance) in the UV and visible domains, *Limnol. Oceanogr.*, 26, 1, 43-53.
- Carmichael, W.W. (1997). The cyanotoxins. In: Callow, J. (Ed.), *Advances in Botanical Research*, vol. 27. Academic Press, London, 211–256.
- Chauhan P., Mohan M., and Nayak S. (2003). Comparative analysis of ocean color measurements of IRS-P4 OCM and SeaWiFS in the Arabian Sea. *IEEE Transactions on Geoscience and Remote Sensing*, 41, 4, 922-926.
- Chauhan P., Mohan, M., Sarngi, R. K., B. Kumari and Nayak, S. (2002). Surface chlorophyll *a* estimation in the Arabian Sea using IRS-P4 Ocean Colour Monitor (OCM) satellite data, *Int. J. Rem. Sens.*, 23, 8, 1663-1676.
- Chauhan, P., Nagur, C. R. C., Mohan, M., Nayak, S. R. and Navalgund, R. R. (2001) Surface chlorophyll *a* distribution in Arabian Sea and Bay of Bengal using IRS-P4 Ocean Color Monitor satellite data. *Current Science*, 80, 2, 127-129.
- Cleveland, J. S. and Weidemann, A. D. (1993). Quantifying absorption by aquatic particles: a multiple scattering correction for glass fiber filters, *Limnol. Oceanogr.*, 38, 1321- 1327.
- Codd, G.A., Bell, S.G., Kaya, K., Ward, C.J., Beattie, K.A. and Metcalf, J.S. (1999). Cyanobacterial toxins, exposure routes and human health. *Eur. J. Phycol.* 34 (4), 405–415.
- Crowley, M. F., Bernstein, R., Prasad, K. and Glenn, S. (2003). Oceansat's Ocean Color Monitor: an instrument whose time has come, *Proc. Oceans 2003*, 22-26 Sept. 2003, 3, 1581.
- Dash, P., Walker, N. D., Mishra, D. R. and D'Sa, E. (In Review). Atmospheric correction and vicarious calibration of Oceansat-1 OCM data.

Dash, P., Walker, N., Mishra, D., Hu, C., Pinckney, J. and D'Sa, E. (In Press) Estimation of cyanobacterial pigments in a freshwater lake using OCM satellite data, *Remote Sensing of Environment*.

Dekker, A. G. (1993). Detection of optical water quality parameters for eutrophic waters by high resolution remote sensing, *PhD thesis*, Vrije University, Amsterdam.

Dekker, A. G., Malthus T. J. and Goddijn L. M. (1992). Monitoring cyanobacteria in eutrophic waters using airborne imaging spectroscopy and multispectral remote sensing systems, *Proc. 6<sup>th</sup> Australasian Remote Sensing Conf.*, 1, 204-214.

D'Sa, E. J., Miller, R.L., and McKee, B.A. (2007). Suspended particulate matter dynamics in coastal waters from ocean color: applications to the northern Gulf of Mexico, *Geophys. Res. Letters*, 34-39, L23611, doi:10.1029/2007GL031192.

D'Sa, E.J., Miller, R.L. and Del Castillo, C. (2006). Bio-optical properties and ocean color algorithms for coastal waters influenced by the Mississippi River during a cold front, *Appl. Opt.*, 45, 7410-7428.

D'Sa, E. J., Hu, C., Muller-Karger, F. E., and Carder, K. L. (2002). Estimation of colored dissolved organic matter and salinity fields in Case 2 waters using SeaWiFS: Examples from Florida Bay and Florida Shelf. *Earth and Planetary Sciences (Proc. Indian Acad. Sci.)*, 106, 3, 197-207.

D'Sa, E. J. and Steward, R. G. (2001). Liquid capillary waveguide application in absorbance spectroscopy (reply to comment), *Limnol. Oceanogr.*, 46, 742-745.

D'Sa, E. J., Steward, R. G., Vodacek, A., Blough, N. V. and Phinney, D. (1999). Optical absorption of seawater colored dissolved organic matter determined using a liquid capillary waveguide, *Limnol. Oceanogr.*, 44, 4, 1142-1148.

Doerffer, R. (1992) Imaging spectroscopy for detection of chlorophyll and suspended matter," in *Imaging Spectroscopy: Fundamentals and Prospective Applications*, F. Toselli and J. Bodechtel, Eds. London, U.K.: Kluwer, 215–257.

Downes, M. T. and Hall, J. A. (1998). A sensitive fluorometric technique for the measurement of phycobilin pigments and its application to the study of marine and freshwater picophytoplankton in oligotrophic environments, *J. App. Phyco.*, 10, 4, 357-363.

Dyer, B. D. (2003) *A Field Guide to Bacteria*, Cornell University Press ISBN 0801488540.

Eplee, R. E., Robinson, W. D., Bailey, S. W., Clark, D. K., Werdell, P. J., Wang, M., Barnes, R.A. and McClain, C. R. (2001) The calibration of SeaWiFS. II vicarious techniques, *Applied Optics*, 40, 6701-6718.

ESA (2006) European Space Agency – MERIS Product Handbook. 2.1, 12.

Evans, R. H., and Gordon, H. R., (1994). Coastal zone color scanner "system calibration": A retrospective examination, *J. Geophys. Res.*, 99, 7293-7307.

- Falconer, I.R., Humpage, and A.R. (2005). Health risk assessment of cyanobacterial (blue-green algal) toxins in drinking water, *Int. J. Environ. Res. Public Health*, 2, 1, 43–50.
- Franz, B. A., Bailey, S. W., Werdell, P. J. and McClain, C. R. (2007) Sensor-independent approach to the vicarious calibration of satellite ocean color radiometry. *Applied Optics*, 46, 22, 5068-5082.
- Garcia, A. C., Bargu, S., Dash, P., Rabalais, N. N., Sutor, M., Morrison, W. and Walker, N. D. (2010) Evaluating the potential risk of microcystins to blue crab (*Callinectes sapidus*) fisheries and human health in a eutrophic estuary, *Harmful Algae*, 9, 134–143.
- Geological Survey U. S. (1987). Methods for collection and analysis of aquatic biological and microbiological samples. In L. J. Britton and P. E. Greesonm, eds., *Techniques of water resources investigations of the U. S. Geological Survey, Washington D. C.*, 127-130.
- Gordon, H. R. and Voss, K. J. (2004). MODIS normalized water-leaving radiance algorithm theoretical basis document, Univ. Miami, Coral Gables, FL, *Tech. Rep. MOD 18*, NAS5-31 363.
- Gordon, H. R. (1997). Atmospheric correction of ocean color imagery in the Earth Observing System era, *J. Geophys. Res.*, 102, 17081-17106.
- Gordon H. R. and Wang M. H. (1994). Retrieval of water-leaving radiance and aerosol optical-thickness over the oceans with SeaWiFS - A preliminary algorithm, *Appl. Opt.*, 33, 443-452.
- Gordon H. R. (1995) Remote sensing of ocean color: a methodology for dealing with broad spectral bands and significant out-of-band response, *Appl. Opt.*, 34, 36, 8363-8374.
- Gordon, H. R., Brown, O. B., Evans, R. H., Brown, J. W., Smith, R. C., Baker, K. S. and Clark, D. K. (1988). A semi-analytic radiance model of ocean color, *J. Geophys. Res.*, 93, 10909-10924.
- Gordon, H. R., Brown, J. W. and Evans, R. (1988) Exact Rayleigh scattering calculations for use with the Nimbus-7 Coastal Zone Color Scanner, *Appl. Opt.*, 27, 5, 862-871.
- Gordon, H. R. (1978) Removal of atmospheric effects from the satellite imagery of oceans, *Appl. Opt.* 17, 10, 1631-1636.
- Gould, R. W. and Arnone, R. A. (1997) Remote sensing estimates of inherent optical properties in a coastal environment. *Remote Sensing of Environment*, 61, 290–301.
- Gregg, W. W. and Carder, K. L. (1990) A simple spectral solar irradiance model for cloudless maritime atmospheres, *Limnol. Oceanogr.*, 35(8), 1657-1675.
- Hansen J. E. and Travis L. D. (1974) Light scattering in planetary atmospheres, *Space Sci. Rev.*, 16, 527–610.
- Hooker, S. B., McClain, C. R., and Holmes, A. (1993). Ocean Color Imaging: CZCS to SeaWiFS, *Marine Technol. Soc.*, 27(1), 2-15.



- Hu, C., Lee, Z., Ma, R., Yu, Kun, Li, D. and Shang, S. (2010). Moderate Resolution Imaging Spectroradiometer (MODIS) observations of cyanobacteria blooms in Taihu Lake, China, *J. Geophys. Res.*, 115, C04002, doi: 10.1029/2009JC005511.
- Hu, C., Chen, Z., Clayton, T. D., Swarzenski, P., Brock, J. C. and Muller-Karger, F. E. (2004). Assessment of estuarine water-quality indicators using MODIS medium-resolution bands: Initial results from Tampa Bay, FL, *Remote Sens. Environ.*, 93, 423-441.
- Hu, C. (2003). A simple instrument for measurement of remote sensing reflectance in coastal environment. SPIE Proceedings 4897 (Multispectral and Hyperspectral Remote Sensing Instruments and Applications, edited by Allen M. Larar, Qingxi Tong, and Makoto Suzuki. SPIE, Bellingham, WA, 2003), 219-226.
- Hu, C., Carder, K. L. and Muller-Karger, F. E. (2000). Atmospheric correction of SeaWiFS imagery of turbid coastal waters: a practical method, *Remote Sens. Environ.*, 74, 195-206.
- Hunter, P. D., Tyler, A. N., Willby, N. J. and Gilvear, D. J. (2008). The spatial dynamics of vertical migration by *Microcystis aeruginosa* in a eutrophic shallow lake: A case study using high spatial resolution time-series airborne remote sensing, *Limnol. Oceanogr.*, 53, 2391-2406.
- IOCCG (2010). Atmospheric Correction for Remotely-Sensed Ocean-Colour Products, M. Wang, ed., Reports of the International Ocean-Colour Coordinating Group, No. 10 (IOCCG, Dartmouth, Nova Scotia, Canada).
- ISRO (2010). Oceansat-2 meeting global demand, 53<sup>rd</sup> session of UNCOPUS, Vienna.
- Jeffrey SW, Vesik M (1997) Introduction to marine phytoplankton and their pigment signatures. In: Jeffrey SW, Mantoura RFC, Wright SW (eds) Phytoplankton pigments in oceanography. SCOR-UNESCO, Paris, 37-84.
- Kattawar, G. W., Plass, G. N. and Hitzfelder, S. J. (1976) Multiple scattered radiation emerging from Rayleigh and continental haze layers. 1: Radiance, polarization, and neural points. *Applied Optics*, 15, 632.
- Kirk, J. T. O. (1994) Light and Photosynthesis in Aquatic Ecosystems. Cambridge, U.K.: Cambridge Univ. Press, 509.
- Kutser, T. (2009) Passive optical remote sensing of cyanobacteria and other intense phytoplankton blooms in coastal and inland waters. *Int. J. Remote Sensing*, 30, 17, 4401-4425.
- Kutser, T., Metsamaa, L., Strombeck, N. and Vahtmae, E. (2006). Monitoring cyanobacterial blooms by satellite remote sensing, *Estuarine, Coastal and Shelf Science*, 67, 303-312.
- Latasa, M. (2007). Improving estimations of phytoplankton class abundances using CHEMTAX, *Mar. Ecol. Prog. Ser.*, 329, 13-21.
- Liew, S. C., Kwok, L. K. and Lim, H. (2000). Classification of algal bloom types from remote sensing reflectance. *GIS Development*, December 2000, 1-3.

- Lyon, P. E. (2009) An automated de-stripping algorithm for Ocean Color Monitor imagery. *Int. J. of Remote Sensing*, 30, 6, 2009, 1493–1502.
- MacColl, R. and Guard-Friar, D. (1987). Phycobiliproteins. Boca Raton, FL: CRC Press.
- Mackey, M. D., Mackey D. J., Higgins, H. W. and Wright S. W. (1996). CHEMTAX -a program for estimating class abundances from chemical markers: application to HPLC measurements of phytoplankton, *Mar. Ecol. Prog. Ser.*, 144, 265–283.
- McClain, C.R., E.J. Ainsworth, R.A. Barnes, R.E. Eplee, Jr., F.S. Patt, W.D. Robinson, M. Wang, and S.W. Bailey (2000) SeaWiFS Postlaunch Calibration and Validation Analyses, Part 1. *NASA Tech. Memo*, 9, S.B. Hooker and E.R. Firestone, Eds., NASA Goddard Space Flight Center, 11.
- McClain, C. R., Cleave, M. L., Feldman, G. C., Gregg, W. W., Hooker, S. B. and Kuring, N. (1998). Science quality SeaWiFS data for global biosphere research. *Sea Technology*. 10-16.
- Metsamaa, L., Kutser, T., and Strombeck, N. (2006). Recognising cyanobacterial blooms based on their optical signature: a modeling study, *Boreal Environ. Res.*, 11, 493-506.
- Metcalf, J.S., and Codd, G.A. (2004) *Cyanobacterial Toxins in the Water Environment*. ROCK – Reviews of Current Knowledge, Marlow, Bucks, UK: Foundation for Water Research.
- Mishra, D. R., Narumalani, S., Rundquist, D. and Lawson, M. (2005). High-Resolution Ocean Color Remote Sensing of Benthic Habitats: A case study at the Roatan Island, Honduras, *IEEE Trans. Geosci. Remote Sens.*, 43, 7, 1592-1604.
- Mishra S., Mishra, D. R. and Schluchter, W. M. (2009). A Novel Algorithm for Predicting Phycocyanin Concentrations in Cyanobacteria: A Proximal Hyperspectral Remote Sensing Approach, *Remote Sens.*, 1, 757-775.
- Mitchell, G., Bricaud, A., Carder, K., Cleveland, J., Ferrari, G., Gould, R., Kahru, M., Kishino, M., Maske, H., Moisan, T., Moore, L., Nelson, N., Phinney, D., Reynolds, R., Sosik, H., Stramski, D., Tassan, S., Trees, C., Weidemann, A., Weiland, J., and Vodacek, A. (2002) Determination of spectral absorption coefficients of particles, dissolved material, and phytoplankton for discrete water samples in *Ocean optics protocols for satellite ocean color sensor validation, Revision 2, NASA/TM 2000-209966*, G. S. Fargion and J. L. Mueller, Eds, 125-153, NASA, Goddard Space Flight Center, Greenbelt, MD.
- Mohan, M. and Chauhan, P. (2003) Atmospheric correction for ocean color remote sensing, ISRO Scientific report IRS-P4/SATCORE/SAC/RESIPA/MWRG/SR/22/2003.
- Mobley, C. D. (1994). Light and Water: Radiative transfer in natural waters. San Diego: Academic Press, 592 pp.
- Morel, A., and Maritorena, S. (2001). Bio-optical properties of oceanic waters: a reappraisal, *J. Geophys. Res.*, 106, 7163–7180.

- Nagamani, P. V., Chauhan, P. and Dwivedi, R. M. (2007). Estimation of chlorophyll *a* concentration using an artificial neural network (ANN)-Based algorithm with oceansat-1 OCM data, *Journal of the Indian Society of Remote Sensing*, 35, 3, 201-207.
- Naik, P., D'Sa, E. J., Goes, J. I., and Gomes, H. R. (2010). Assessment of particulate absorption properties in the southeastern Bering Sea from in-situ and remote sensing data, *Journal of Applied Remote Sensing*, 4, 043561, doi:10.1117/1.3525572.
- Nayak, S., Solanki, H. U. and Dwivedi, R.M. (2003). Utilisation of IRS P4 ocean colour data for potential fishing zone – a cost benefit analysis, *Indian J. Mar. Sci.*, 29, 244-248.
- Olson J. M. (2006). "Photosynthesis in the Archean era". *Photosyn. Res.* 88(2): 109–117. doi:10.1007/s11120-006-9040-5. PMID 16453059, Retrieved on May 30, 2011 from <http://www.scribd.com/doc/53317475/Cyanobacteria>.
- O'Reilly, J. E., Maritorena, S., Mitchell, G. G., Siegel, D. A., Carder, K. L., Garver, S. A., Kahru, M., and McClain, C. (1998) Ocean color algorithms for SeaWiFS. *Journal of Geophysical Research*, 103, 24937– 24953.
- Pandya M. R., Singh, R. P., Murali, K. R., Babu, P. N., Kirankumar A. S. and Dadhwal, B. K. (2002) Bandpass Solar Exoatmospheric Irradiance and Rayleigh Optical Thickness of Sensors On Board Indian Remote Sensing Satellites-1B, -1C, -1D, and P4. *IEEE Transactions on Geoscience and Remote Sensing*, 40, 3, 714-718.
- Petzold, T. J. (1972). Volume Scattering Functions for Selected Ocean Waters, SIO Ref. 71-78 (Scripps Institution of Oceanography, San Diego, Calif.).
- Pinckney, J. L., Wee, J. L., Hou, A. and Walker, N. D. (2009). Phytoplankton community structure responses to urban effluent inputs following Hurricanes Katrina and Rita, *Mar. Ecol. Prog. Ser.*, 387, 137–146.
- Pope, R. M. and Fry, E. S. (1997). Absorption spectrum (380–700 nm) of pure water. II. Integrating cavity measurements, *Appl. Opt.*, 36, 8710–8723.
- Randolph, K., Wilson, J., Tedesco, L., Li, L., Pascual, D. L. and Soyeux, E. (2008). Hyperspectral remote sensing of cyanobacteria in turbid productive water using optically active pigments, chlorophyll *a* and phycocyanin, *Remote Sens. Environ.*, 112, 11, 4009-4019
- Ren, L., Rabalais, N.N., Morrison, W., Mendenhall, W. and Turner, R.E. (2009). Nutrient limitation on phytoplankton growth in upper Barataria Basin, Louisiana: microcosm bioassays, *Estuaries and Coasts*, 32, 958–974.
- Reynolds, R. A., Stramski, D., and Mitchell, B. G. (2001). A chlorophyll-dependent semi analytical reflectance model derived from field measurements of absorption and backscattering coefficients within the Southern Ocean. *J. Geophys. Res.*, 106, 7125-7138.
- Richardson, L. L., Liu, C. J., Buisson, D. and Ambrosia, V. (1994). The detection of algal photosynthetic accessory pigments using airborne visible-infrared imaging spectrometer (AVIRIS) spectral data, *Marine Tech. Soc. J.*, 28, 10-21.

- Ruiz-Verdu, A., Simis, S. G. H., de Hoyos, C., Gons, H. J., Pena- Martinez, R. (2008). An evaluation of algorithms for the remote sensing of cyanobacterial biomass, *Remote Sens. Environ.*, 2008, 112, 3996–4008.
- Sarangi, R. K., Chauhan, P., Nayak, S. R. and Shreedhar, U. (2005). Remote sensing of Trichodesmium blooms in the coastal waters off Gujarat, India using IRS-P4 OCM, *Int. J. Rem. Sens.*, 26, 9, 1777-1780.
- Schalles, J. F., and Y. Z. Yacobi. (2000). Remote detection and seasonal patterns of phycocyanin, carotenoids and chlorophyll pigments in eutrophic waters. *Arch. Hydrobiol. Spec. Issues Advanc. Limnol.*, 55, 153-168.
- Schlüter L., Lauridsen, T. L., Krogh, G., and Jørgensen, T. (2006). Identification and quantification of phytoplankton groups in lakes using new pigment ratios – a comparison between pigment analysis by HPLC and microscopy. *Freshwater Biology*, 51, 1474–1485.
- Siegel, D.A., Thomas, A.C. and Marra, J. (2004). Views of ocean processes from the Sea-viewing Wide Field-of view Sensor mission: introduction to the first special issue, *Deep-Sea Research II*, 51, 2004, 1–3.
- Siegel, D. A., Wang, M., Maritorena, S. and Robinson, W. (2000) Atmospheric correction of satellite ocean color imagery: the black pixel assumption, *Applied Optics*, 39, 3582-3591.
- Simis, S. G. H., S. W. M. Peters, and H. J. Gons. (2005). Remote sensing of the cyanobacteria pigment phycocyanin in turbid inland water. *Limnol. Oceanogr.*, 50, 237–245.
- Simis, S. G. H., Peters, S. W. M., & Gons, H. J. (2006). MERIS potential for remote sensing of water quality parameters for turbid inland water, p. 97–120. In: Simis, S.G.H., Blue-green catastrophe: remote sensing of mass viral lysis of cyanobacteria. Ph.D. thesis, Vrije Universiteit Amsterdam.
- Simis, S. G. H., Ruiz-Verdú, A., Domínguez-Gómez, J. A., Peña-Martínez, R., Peters, S.W.M., and Gons, H. J. (2007). Influence of phytoplankton pigment composition on remote sensing of cyanobacterial biomass, *Rem. Sens. Environ.*, 106, 414–427.
- Singh, S., D'Sa, E. J. and Swenson, E. (2010a). Chromophoric dissolved organic matter (CDOM) variability in Barataria Basin using excitation-emission matrix (EEM) fluorescence and parallel factor analysis (PARAFAC). *Sci. Tot. Environ.*, 408, 3211-3222.
- Singh, S., D'Sa, E. J. and Swenson, E. (2010b). Seasonal variability in CDOM absorption and fluorescence properties in the Barataria Basin, Louisiana, USA. *J. Environ. Sci.* 22, 1481-1490.
- Smith, R. C. and Baker, K. S. (1981). Optical properties of the clearest natural waters (200-800 nm), *Appl. Opt.*, 20, 2, 177-184.
- Solanki, H.U., Dwivedi, R.M., and S.R. Nayak. (2000). Generation of composite image using OCM chlorophyll and NOAA AVHRR SST for locating potential fishing grounds. *PORSEC 2000 Proceedings*, Goa, India, Dec 5-8, II, 669-672.

- Solanki, H.U., Dwivedi, R.M., Nayak, S.R., Somvanshi, V.S., Gulati, D.K. and Pattnayak, S.K. (2003). Fishery forecast using OCM chlorophyll concentration and AVHRR SST: Validation results Off Gujarat Coast, India, *Int. J Rem. Sens.*, 24, 18, 3691-3699.
- Stumpf, R. P., Arnone, R. A., Gould, R. W. Jr., Martinolich, P. M. and Ransibrahmanakul, V. (2003) A partially coupled ocean-atmosphere model for retrieval of water-leaving radiance from SeaWiFS in coastal waters. *SeaWiFS postlaunch technical report series, 22: Algorithm updates for the fourth SeaWiFS data processing*, Hooker and E.R. Firestone, Eds., 51-59.
- Suresh, T., Desa, E., Mascarenhas, A., Matondkar, S. G. P., Naik, P. and Nayak S.R. (2006) Remote sensing and modeling of the atmosphere, oceans, and interactions, *Proc. of SPIE*, 6404, T. N. Krishnamurti, B. N. Goswami, T. Iwasaki, 1-9.
- Vincent, R. K., Qin, X., Mckay, R. M. L. and Miner. J. (2004). Phycocyanin detection from LANDSAT TM data for mapping cyanobacterial blooms in Lake Erie. *Remote Sens. Environ.*, 89, 381–392.
- Wang, M. and Franz, B. A. (2000) Comparing the ocean color measurements between MOS and SeaWiFS: A vicarious intercalibration approach for MOS, *IEEE Transactions on Geoscience and Remote Sensing*, 38, 1, 184-197.
- Wang, M. (1999) A sensitivity study of SeaWiFS atmospheric correction algorithm: Effects of spectral band variations, *Remote Sensing of Environment*, 67, 348–359.
- Wynne, T. T., Stumpf, R. P., Tomlinson, M. C. and Dyble, J. (2010). Characterizing a cyanobacterial bloom in western Lake Erie using satellite imagery and meteorological data, *Limnol. Oceanogr.*, 55, 5, 2025–2036.

## APPENDIX A

### TIME SERIES OF WATER QUALITY PARAMETERS MEASURED BY THE DEPLOYED YSI INSTRUMENTS

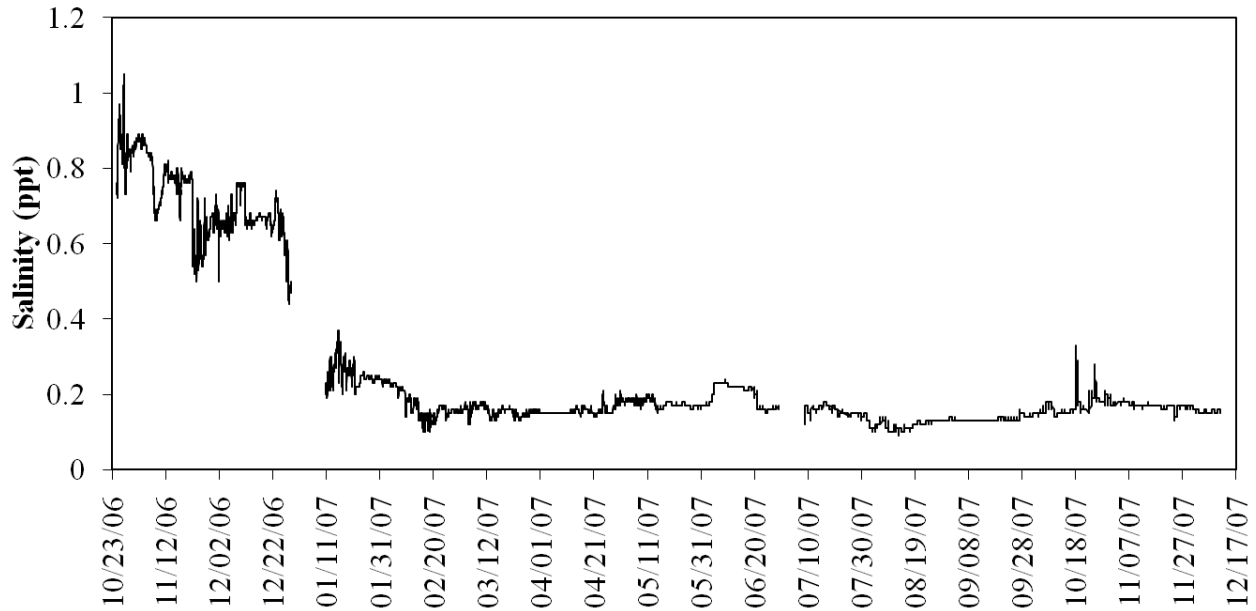


Fig. A.1 Time series of salinity at the YSI instrument deployment site in Lac des Allemands from October 24, 2006 through December 11, 2007.

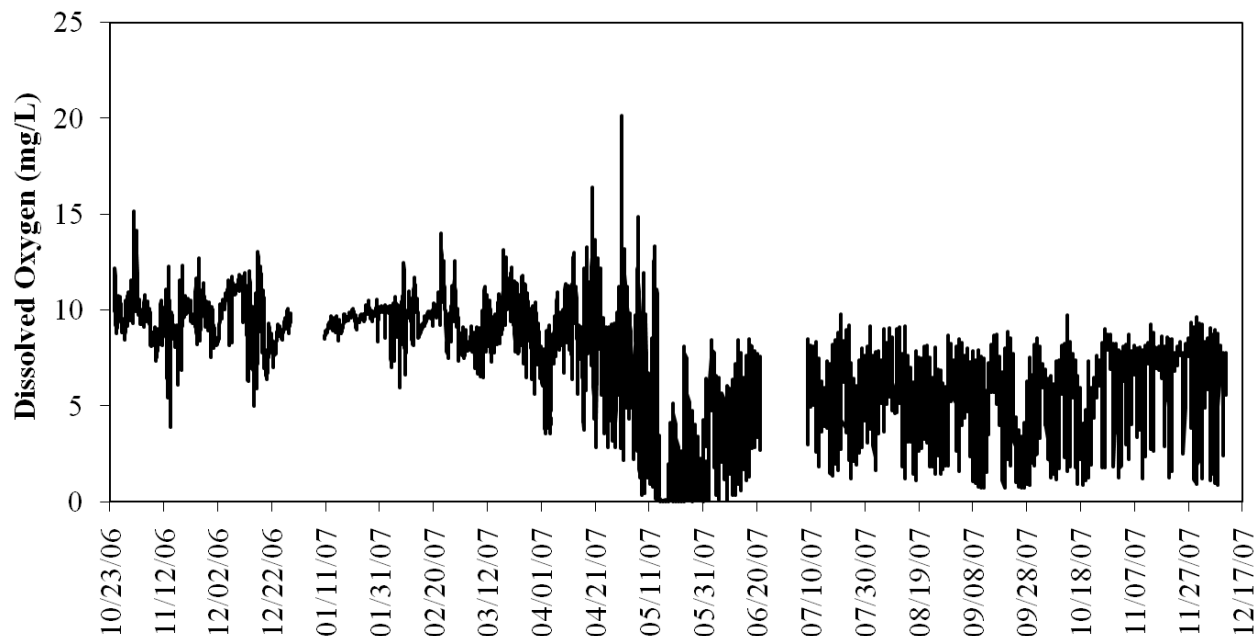


Fig. A.2 Time series of dissolved oxygen at the YSI instrument deployment site in Lac des Allemands from October 24, 2006 through December 11, 2007.

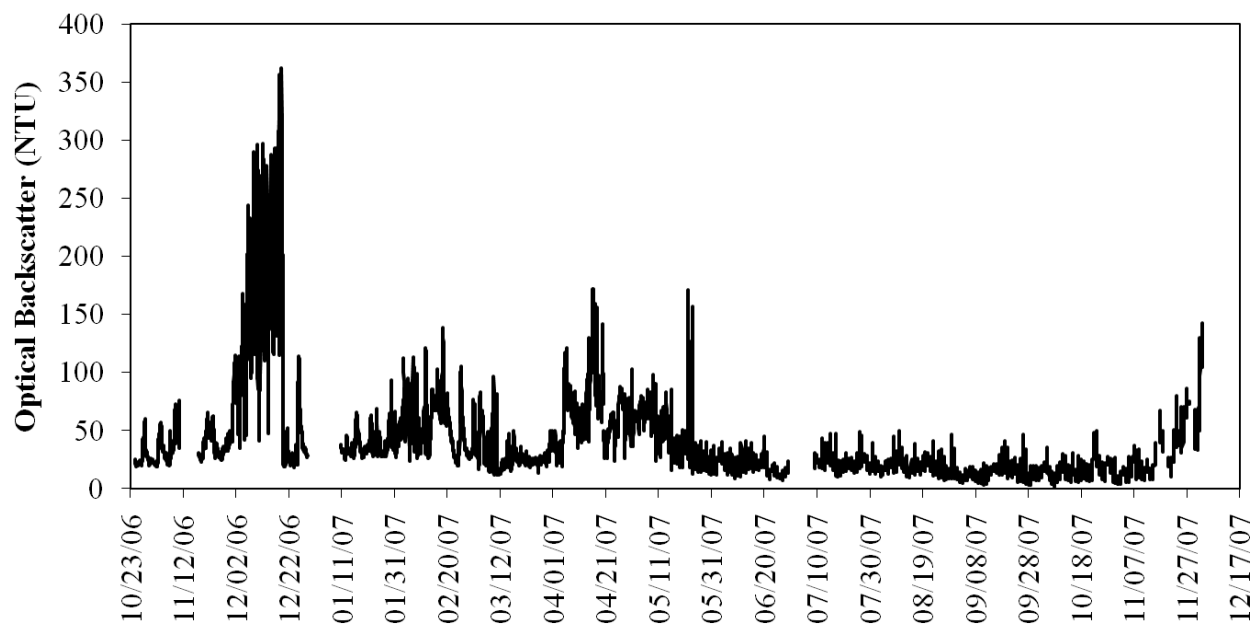


Fig. A.3 Time series of optical backscatter, a measure of turbidity, at the YSI instrument deployment site in Lac des Allemands from October 24, 2006 through December 11, 2007.

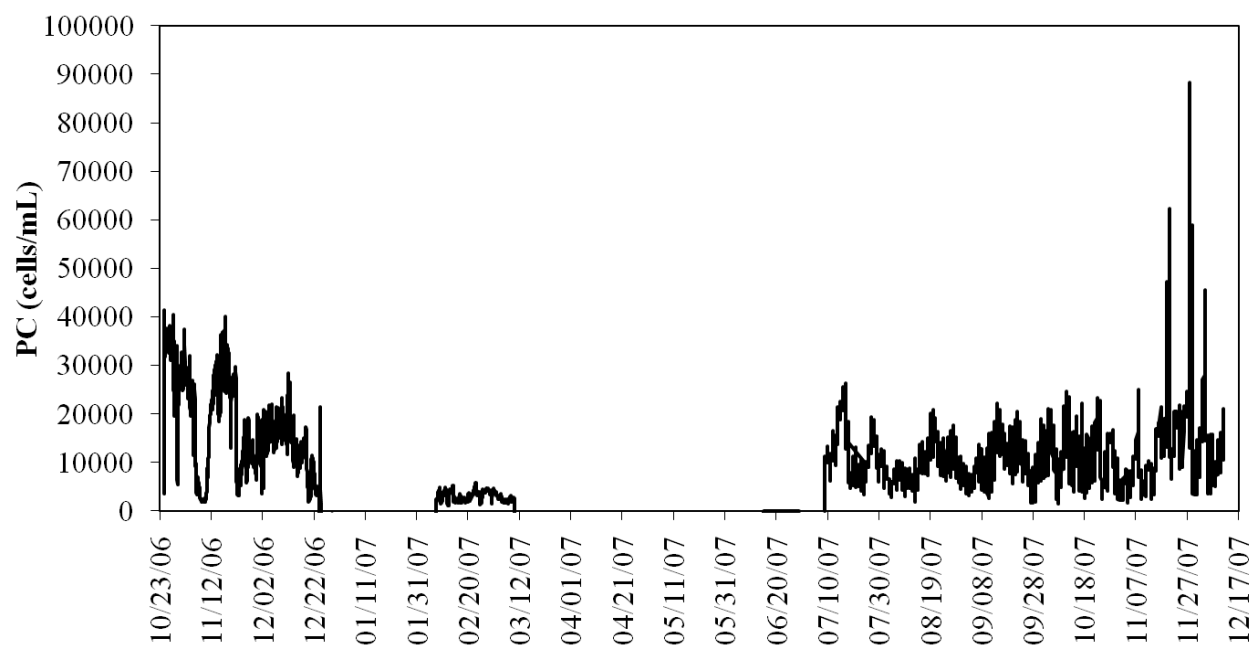


Fig. A.4 Time series of PC concentrations at the YSI instrument deployment site in Lac des Allemands from October 24, 2006 through December 11, 2007.

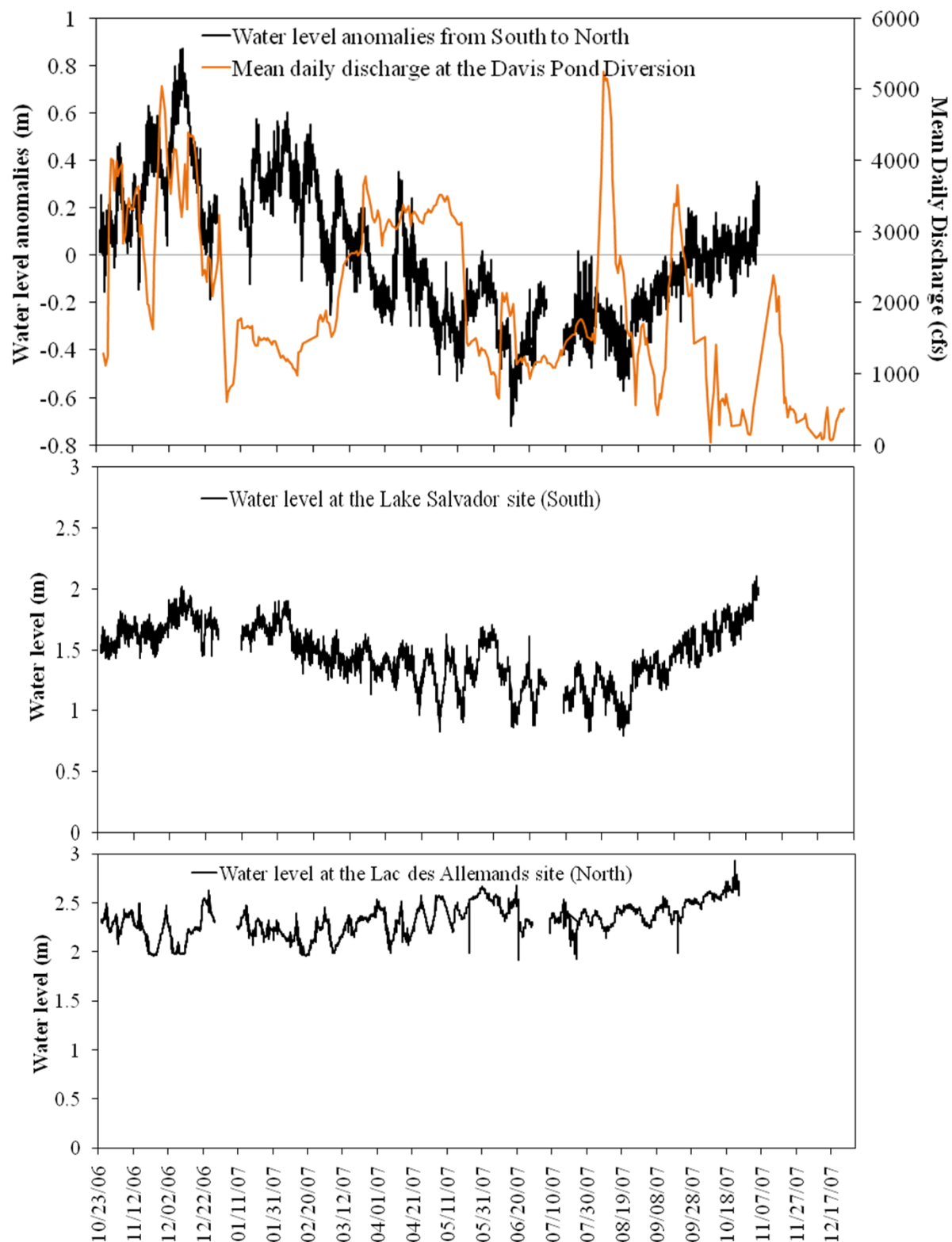


Fig. A.5 Water level at the YSI instrument deployment sites in Lac des Allemands and Lake Salvador, and the water level anomalies in comparison with mean daily discharge at the Davis Pond Diversion.



## APPENDIX B

### GLOSSARY

CDOM	Chromophoric Dissolved Organic Matter
Chl <i>a</i>	Chlorophyll <i>a</i>
CZCS	Coastal Zone Color Scanner
GLI	Global Imager
HPLC	High Performance Liquid Chromatography
MERIS	Medium Resolution Imaging Spectrometer
MISR	Multi-angle Imaging Spectroradiometer
MLAC	Merged local area coverage
MOBY	Marine Optical Buoy
MODIS	Moderate Resolution Imaging Spectroradiometer
NASA	National Aeronautics and Space Agency
NRSC	National Remote Sensing Center
OBPG	Ocean Biology Processing Group
OCI	Ocean Color Imager, OSMI- Ocean Scanning Multispectral Imager
OCM	Ocean Color Monitor
OCTS	Ocean Color and Temperature Scanner
PC	Phycocyanin
POLDER-2	Polarization and Directionality of the Earth's Reflectance-2
SeaWiFS	Sea-viewing Wide Field-of-View Sensor
SPM	Suspended Particulate Matter
TOA	Top of the atmosphere
TOMS	Total Ozone Mapping Spectrometer

## APPENDIX C

### PERMISSION

#### ELSEVIER LICENSE TERMS AND CONDITIONS

Oct 17, 2011

---

---

This is a License Agreement between Padmanava Dash ("You") and Elsevier ("Elsevier") provided by Copyright Clearance Center ("CCC"). The license consists of your order details, the terms and conditions provided by Elsevier, and the payment terms and conditions.

**All payments must be made in full to CCC. For payment instructions, please see information listed at the bottom of this form.**

Supplier	Elsevier Limited The Boulevard, Langford Lane Kidlington, Oxford, OX5 1GB, UK
Registered Company Number	1982084
Customer name	Padmanava Dash
Customer address	412 B, Howe-Russel Geoscience Complex Baton Rouge, LA 70803
License number	2771400701075
License date	Oct 17, 2011
Licensed content publisher	Elsevier
Licensed content publication	Remote Sensing of Environment
Licensed content title	Estimation of cyanobacterial pigments in a freshwater lake using OCM satellite data
Licensed content author	Padmanava Dash, Nan D. Walker, Deepak R. Mishra, Chuanmin Hu, James L. Pinckney, Eurico J. D'Sa
Licensed content date	1 September 2011
Licensed content volume number	
Licensed content issue number	
Number of pages	1
Start Page	
End Page	
Type of Use	reuse in a thesis/dissertation
Portion	full article

Format	both print and electronic
Are you the author of this Elsevier article?	Yes
Will you be translating?	No
Order reference number	
Title of your thesis/dissertation	QUANTITATIVE MAPPING OF CYANOBACTERIAL BLOOMS USING OCEANSAT-1 OCM SATELLITE DATA
Expected completion date	Dec 2011
Estimated size (number of pages)	109
Elsevier VAT number	GB 494 6272 12
Permissions price	0.00 USD
VAT/Local Sales Tax	0.00 USD / GBP
Total	0.00 USD
Terms and Conditions	

## INTRODUCTION

1. The publisher for this copyrighted material is Elsevier. By clicking "accept" in connection with completing this licensing transaction, you agree that the following terms and conditions apply to this transaction (along with the Billing and Payment terms and conditions established by Copyright Clearance Center, Inc. ("CCC"), at the time that you opened your Rightslink account and that are available at any time at <http://myaccount.copyright.com>).

## GENERAL TERMS

2. Elsevier hereby grants you permission to reproduce the aforementioned material subject to the terms and conditions indicated.

3. Acknowledgement: If any part of the material to be used (for example, figures) has appeared in our publication with credit or acknowledgement to another source, permission must also be sought from that source. If such permission is not obtained then that material may not be included in your publication/copies. Suitable acknowledgement to the source must be made, either as a footnote or in a reference list at the end of your publication, as follows:

“Reprinted from Publication title, Vol /edition number, Author(s), Title of article / title of chapter, Pages No., Copyright (Year), with permission from Elsevier [OR APPLICABLE SOCIETY COPYRIGHT OWNER].” Also Lancet special credit - “Reprinted from The Lancet, Vol. number, Author(s), Title of article, Pages No., Copyright (Year), with permission from Elsevier.”

4. Reproduction of this material is confined to the purpose and/or media for which

permission is hereby given.

5. **Altering/Modifying Material: Not Permitted.** However figures and illustrations may be altered/adapted minimally to serve your work. Any other abbreviations, additions, deletions and/or any other alterations shall be made only with prior written authorization of Elsevier Ltd. (Please contact Elsevier at [permissions@elsevier.com](mailto:permissions@elsevier.com))

6. If the permission fee for the requested use of our material is waived in this instance, please be advised that your future requests for Elsevier materials may attract a fee.

7. **Reservation of Rights:** Publisher reserves all rights not specifically granted in the combination of (i) the license details provided by you and accepted in the course of this licensing transaction, (ii) these terms and conditions and (iii) CCC's Billing and Payment terms and conditions.

8. **License Contingent Upon Payment:** While you may exercise the rights licensed immediately upon issuance of the license at the end of the licensing process for the transaction, provided that you have disclosed complete and accurate details of your proposed use, no license is finally effective unless and until full payment is received from you (either by publisher or by CCC) as provided in CCC's Billing and Payment terms and conditions. If full payment is not received on a timely basis, then any license preliminarily granted shall be deemed automatically revoked and shall be void as if never granted. Further, in the event that you breach any of these terms and conditions or any of CCC's Billing and Payment terms and conditions, the license is automatically revoked and shall be void as if never granted. Use of materials as described in a revoked license, as well as any use of the materials beyond the scope of an unrevoked license, may constitute copyright infringement and publisher reserves the right to take any and all action to protect its copyright in the materials.

9. **Warranties:** Publisher makes no representations or warranties with respect to the licensed material.

10. **Indemnity:** You hereby indemnify and agree to hold harmless publisher and CCC, and their respective officers, directors, employees and agents, from and against any and all claims arising out of your use of the licensed material other than as specifically authorized pursuant to this license.

11. **No Transfer of License:** This license is personal to you and may not be sublicensed, assigned, or transferred by you to any other person without publisher's written permission.

12. **No Amendment Except in Writing:** This license may not be amended except in a writing signed by both parties (or, in the case of publisher, by CCC on publisher's behalf).

13. **Objection to Contrary Terms:** Publisher hereby objects to any terms contained in any purchase order, acknowledgment, check endorsement or other writing prepared by you, which terms are inconsistent with these terms and conditions or CCC's Billing and

Payment terms and conditions. These terms and conditions, together with CCC's Billing and Payment terms and conditions (which are incorporated herein), comprise the entire agreement between you and publisher (and CCC) concerning this licensing transaction. In the event of any conflict between your obligations established by these terms and conditions and those established by CCC's Billing and Payment terms and conditions, these terms and conditions shall control.

14. **Revocation:** Elsevier or Copyright Clearance Center may deny the permissions described in this License at their sole discretion, for any reason or no reason, with a full refund payable to you. Notice of such denial will be made using the contact information provided by you. Failure to receive such notice will not alter or invalidate the denial. In no event will Elsevier or Copyright Clearance Center be responsible or liable for any costs, expenses or damage incurred by you as a result of a denial of your permission request, other than a refund of the amount(s) paid by you to Elsevier and/or Copyright Clearance Center for denied permissions.

### **LIMITED LICENSE**

The following terms and conditions apply only to specific license types:

15. **Translation:** This permission is granted for non-exclusive world **English** rights only unless your license was granted for translation rights. If you licensed translation rights you may only translate this content into the languages you requested. A professional translator must perform all translations and reproduce the content word for word preserving the integrity of the article. If this license is to re-use 1 or 2 figures then permission is granted for non-exclusive world rights in all languages.

16. **Website:** The following terms and conditions apply to electronic reserve and author websites:

**Electronic reserve:** If licensed material is to be posted to website, the web site is to be password-protected and made available only to bona fide students registered on a relevant course if:

This license was made in connection with a course,

This permission is granted for 1 year only. You may obtain a license for future website posting,

All content posted to the web site must maintain the copyright information line on the bottom of each image,

A hyper-text must be included to the Homepage of the journal from which you are licensing at <http://www.sciencedirect.com/science/journal/xxxxx> or the Elsevier homepage for books at <http://www.elsevier.com> , and

Central Storage: This license does not include permission for a scanned version of the material to be stored in a central repository such as that provided by Heron/XanEdu.

17. **Author website** for journals with the following additional clauses:

All content posted to the web site must maintain the copyright information line on the

bottom of each image, and

the permission granted is limited to the personal version of your paper. You are not allowed to download and post the published electronic version of your article (whether PDF or HTML, proof or final version), nor may you scan the printed edition to create an electronic version,

A hyper-text must be included to the Homepage of the journal from which you are licensing at <http://www.sciencedirect.com/science/journal/xxxxx> , As part of our normal production process, you will receive an e-mail notice when your article appears on Elsevier's online service ScienceDirect ([www.sciencedirect.com](http://www.sciencedirect.com)). That e-mail will include the article's Digital Object Identifier (DOI). This number provides the electronic link to the published article and should be included in the posting of your personal version. We ask that you wait until you receive this e-mail and have the DOI to do any posting.

Central Storage: This license does not include permission for a scanned version of the material to be stored in a central repository such as that provided by Heron/XanEdu.

**18. Author website** for books with the following additional clauses:

Authors are permitted to place a brief summary of their work online only.

A hyper-text must be included to the Elsevier homepage at <http://www.elsevier.com>

All content posted to the web site must maintain the copyright information line on the bottom of each image

You are not allowed to download and post the published electronic version of your chapter, nor may you scan the printed edition to create an electronic version.

Central Storage: This license does not include permission for a scanned version of the material to be stored in a central repository such as that provided by Heron/XanEdu.

**19. Website** (regular and for author): A hyper-text must be included to the Homepage of the journal from which you are licensing at <http://www.sciencedirect.com/science/journal/xxxxx>. or for books to the Elsevier homepage at <http://www.elsevier.com>

**20. Thesis/Dissertation:** If your license is for use in a thesis/dissertation your thesis may be submitted to your institution in either print or electronic form. Should your thesis be published commercially, please reapply for permission. These requirements include permission for the Library and Archives of Canada to supply single copies, on demand, of the complete thesis and include permission for UMI to supply single copies, on demand, of the complete thesis. Should your thesis be published commercially, please reapply for permission.

**21. Other Conditions:**

v1.6

**If you would like to pay for this license now, please remit this license along with your payment made payable to "COPYRIGHT CLEARANCE CENTER" otherwise you will be invoiced within 48 hours of the license date. Payment should be in the form of a check or money order referencing your account number and this invoice number RLNK500646840.**

**Once you receive your invoice for this order, you may pay your invoice by credit card. Please follow instructions provided at that time.**

**Make Payment To:  
Copyright Clearance Center  
Dept 001  
P.O. Box 843006  
Boston, MA 02284-3006**

**For suggestions or comments regarding this order, contact RightsLink Customer Support: [customercare@copyright.com](mailto:customercare@copyright.com) or +1-877-622-5543 (toll free in the US) or +1-978-646-2777.**

**Gratis licenses (referencing \$0 in the Total field) are free. Please retain this printable license for your reference. No payment is required.**

---

---

## VITA

Padmanava Dash was born in 1978 in Anandapur, a city in the state of Orissa in India. He obtained Bachelor of Science and Master of Science degrees in geology from Utkal University, Bhubaneswar, India. To explore the subject from both theoretical and applied aspects, he joined the master's program in applied geology at the Indian Institute of Technology (IIT), Bombay. At IIT, Bombay, he took rigorous courses and carried out research on a project entitled "Environmental case study of Cauvery river floodplain using IRS 1D satellite data" for his thesis which was published in the journal *GIS Development*. The thesis focused on monitoring the variability in land use, land cover, surface water, drainage and the river morphology from 1968 to 2002 employing topographic sheets and satellite imagery. In August of 2003 he came to the USA to join the master's program in geology program at Bowling Green State University (BGSU). At BGSU, his master's thesis involved developing an algorithm for mapping incipient cyanobacteria blooms from SeaWiFS data. The algorithm could serve as a tool for early stage monitoring of cyanobacterial blooms in Lake Erie and was published in the *Proceedings of ASPRS*. He joined the doctoral program in the Department of Oceanography and Coastal Sciences at Louisiana State University in the fall of 2005. Under the advisor-ship of Dr. Nan Walker and with funding from her grants (a NASA grant and a grant from the Shell Oil Company) he performed his doctoral research. He won two poster awards and four travel awards for presenting his dissertation research in conferences. This dissertation is the culmination of that research. He expects to receive the Doctor of Philosophy degree in December, 2011.